

FINAL REPORT

A Miniature Wide Band Atomic Magnetometer

SERDP Project MR-1568

DECEMBER 2011

Dr. Mark Prouty
Geometrics, Inc.

This document has been cleared for public release



Report Documentation Page

Form Approved
OMB No. 0704-0188

Public reporting burden for the collection of information is estimated to average 1 hour per response, including the time for reviewing instructions, searching existing data sources, gathering and maintaining the data needed, and completing and reviewing the collection of information. Send comments regarding this burden estimate or any other aspect of this collection of information, including suggestions for reducing this burden, to Washington Headquarters Services, Directorate for Information Operations and Reports, 1215 Jefferson Davis Highway, Suite 1204, Arlington VA 22202-4302. Respondents should be aware that notwithstanding any other provision of law, no person shall be subject to a penalty for failing to comply with a collection of information if it does not display a currently valid OMB control number.

1. REPORT DATE DEC 2011		2. REPORT TYPE N/A		3. DATES COVERED -	
4. TITLE AND SUBTITLE A Miniature Wide Band Atomic Magnetometer				5a. CONTRACT NUMBER	
				5b. GRANT NUMBER	
				5c. PROGRAM ELEMENT NUMBER	
6. AUTHOR(S)				5d. PROJECT NUMBER	
				5e. TASK NUMBER	
				5f. WORK UNIT NUMBER	
7. PERFORMING ORGANIZATION NAME(S) AND ADDRESS(ES) Geometrics, Inc.				8. PERFORMING ORGANIZATION REPORT NUMBER	
9. SPONSORING/MONITORING AGENCY NAME(S) AND ADDRESS(ES)				10. SPONSOR/MONITOR'S ACRONYM(S)	
				11. SPONSOR/MONITOR'S REPORT NUMBER(S)	
12. DISTRIBUTION/AVAILABILITY STATEMENT Approved for public release, distribution unlimited					
13. SUPPLEMENTARY NOTES SERDP Project MR-1568, The original document contains color images.					
14. ABSTRACT					
15. SUBJECT TERMS					
16. SECURITY CLASSIFICATION OF:			17. LIMITATION OF ABSTRACT SAR	18. NUMBER OF PAGES 83	19a. NAME OF RESPONSIBLE PERSON
a. REPORT unclassified	b. ABSTRACT unclassified	c. THIS PAGE unclassified			

Front Matter

Table Of Contents

Front Matter	ii
<i>Table Of Contents</i>	ii
<i>List of Acronyms</i>	iii
<i>List of Figures and Tables</i>	iii
<i>Acknowledgments</i>	vi
Executive Summary	1
Objective	1
Tasks	2
Summary of Results	3
Objective	6
Background	8
Materials and Methods	12
Results and Accomplishments	13
Task 1. Investigation of Magnetometry at High Cell Temperatures	14
1.1 Build prototype cells for initial measurements	14
1.2 Initial measurements of linewidth and sensitivity as a function of temperature.....	16
1.2 Demonstration of high performance signal detection	22
Task 2 Construction of MEMs Cells	27
2.1 Demonstration of angled interiors	27
2.2 Prototyping MEMs physics package	32
Task 3. Implementation of SERF Technique	48
3.1 Preliminary investigation of SERF in MEMS cells	48
3.2 Further investigation of SERF in MEMS cells	50
Task 4. Electronics Design	51
4.1 Physics package control circuitry	52
4.2 Signal interrogation circuit design	58
4.3 Performance Analysis	65
Concluding Summary	74
Appendices	76
Appendix A: List of Technical Publications	76
References.....	76

List of Acronyms

ADC	– Analog to Digital Converter
AM	– Amplitude Modulation
CAD	– Computer Aided Design
CMRR	– Common Mode Rejection Ratio
CPU	– Central Processing Unit
CSAM	– Chip scale atomic magnetometer
CSAC	– Chip scale atomic clock
DAC	– Digital to Analog Converter
DARPA	– Defense Advanced Research Projects Agency
DBR	– Distributed Bragg Reflector
DC	– Direct Current
EM	– Electromagnetic
ESD	– Electrostatic Discharge
FM	– Frequency Modulation
FFT	– Fast Fourier Transform
FPGA	– Field Programmable Gate Array
GHz	– Gigahertz
MEMS	– Micro-Electro Mechanical System
MF	– z-component Magnetic Quantum Number, M_F
MFTFM	– Microfabricated Total Field Magnetometer
MHz	–Megahertz
MIT	– Massachusetts Institute of Technology
NIST	– National Institute of Standards and Technology
PCB	– Printed Circuit Board
Physics Package	– The physical structure of the cell, laser diode, and light source.
QAM	– Quadrature Amplitude Modulation
RF	– Radio Frequency
RMS	–Root Mean Square
SERF	– Spin-Exchange Relaxation Free
SNR	– Signal to Noise Ratio
SQUID	– Superconducting Quantum Interference Device
UXO	– Unexploded Ordnance
VCSEL	– Vertical-Cavity Surface-Emitting Laser
VCO	– Voltage Controlled Oscillator

List of Figures and Tables

Figure 1.	Basic structure of an atomic magnetometer	1
Figure 2	Summary of performance measurements at various cell temperatures. Increasing the cell temperature increases the absorption. Using the dual-beam method allows for performance congruent with the project’s original goals.....	4
Figure 3	(a) Sensitivity of the wideband magnetometer: 10 pT / $\sqrt{\text{Hz}}$ between 100 and 400 Hz. (b) Bandwidth of the wideband magnetometer: 15 kHz.	4
Figure 4	Sketch of MEMS physics package design which was built in this project.	5
Figure 5	Linewidth of the alkali atom spin resonance as a function of the fraction of absorbed light, which is related to the alkali atom density. The increased linewidth at high densities leads to a magnetic field sensor with a higher bandwidth.....	7
Figure 6	Fundamental magnetometer sensitivity as a function of measurement bandwidth. The vapor density of ^{87}Rb is $10^{11}/\text{cm}^3$ at $\sim 60^\circ\text{C}$ and $10^{14}/\text{cm}^3$ at $\sim 180^\circ\text{C}$. The point labeled MFTFM refers to the target of SERDP project MM-1512.....	9

Figure 7	MEMS designs for chip-scale atomic magnetometers. (a) Cell design for achieving orthogonally propagating beams in a MEMS cell. (b) A design allowing implementation of the two-beam Mx and two-beam Mz geometries. (c) A design allowing implementation of the one-beam Mz geometry.	11
Figure 8	(a) Cell fabrication apparatus at NIST used for producing millimeter-scale alkali vapor cells. (b) Photograph of a typical Cs vapor cell.	14
Figure 9	Optical absorption spectra from six MEMS Cs vapor cells. The sharp features in each spectrum are the absorption lines from a large cell with no buffer gas for frequency calibration.	15
Figure 10	Optical absorption spectra from six MEMS Cs vapor cells at different buffer gas pressures. Increasing the buffer gas pressure broadens the optical linewidth considerably. The curves show are for a range of buffer gas pressure from 150 to 3000 Torr.	15
Figure 11	Characteristics of three methods of signal modulation and extraction	16
Figure 12	Mz Technique.....	16
Figure 13	Bell-Bloom Technique	17
Figure 14	Sensitivity and Bandwidth at 28% absorption	17
Figure 15	Sensitivity and Bandwidth at 64% absorption	18
Figure 16	Sensitivity and Bandwidth at 82% absorption	18
Figure 17	Summary of performance measurements with the Bell Bloom method at various cell temperatures. Increasing the cell temperature increases the absorption.....	18
Figure 18	Mx Technique	19
Figure 19	Experimental setup for measurement of the magnetometer signals at high cell temperature.....	20
Figure 20	(a) Resonance linewidth, extrapolated to low light power, as a function of cell temperature. (b) Sensitivity, as a function of temperature. The open points are for the Bell-Bloom method, while the solid points are the Mx method.....	21
Figure 21	Signal strength, as measured by the contrast, as a function of input optical power for several temperatures.	21
Figure 22	(a) Original Bell-Bloom design with a single, resonant laser. (b) Two-laser design in which one laser, circularly polarized and tuned to the optical resonance, pumps the atoms, and a second, probe laser, linearly polarized and detuned from the optical resonance, interrogates the atoms. The precession of the atomic spins is monitored via the polarization rotation of the probe.	22
Figure 23	Pump/probe scheme for optically thick cells. The pump field is pulsed to avoid optical power broadening of the Larmor resonance.	23
Figure 24	Experimental setup. The cesium atoms are confined in a microfabricated vapor cell of volume 1mm^3 . Light from the pump laser creates a polarization in the atoms, which is probed by a weak linearly polarized VCSEL. The modulation of the polarization rotation of the probe laser at the Larmor frequency is measured with a balanced polarimeter feeding into a lock-in amplifier.	24
Figure 25	Optical rotation signal of the Bell-Bloom wideband magnetometer as the magnetic test field is scanned. The optical density on resonance was ~ 4 (150 °C). Pump and probe power were 500 μW and 12 μW , respectively. The resonance width was measured as 18.5 kHz.....	25
Figure 26	(a) Sensitivity of the wideband magnetometer: 10 pT $\sqrt{\text{Hz}}$ between 100 and 400 Hz. (b) Bandwidth of the wideband magnetometer: 15 kHz.	25
Figure 27	Observed noise as function of probe light frequency detuning for an optical depth value equal to 0.55. Red points: noise in the absence of pump beam. Hollow green triangles: noise when the pump beam is present and the polarimeter is imbalanced. Hollow red circles: noise when the pump beam is present and polarimeter is	

	balanced. Blue dashed line: estimated photon shot noise of transmitted probe on resonance. Solid lines are used to guide the eye. Inset, optical rotation signal (blue trace) and optical rotation angle (red trace).....	26
Figure 28	Vapor cell with integrated multilayer thin film reflectors (on a US quarter for scale)	27
Figure 29	Fabrication of the bulk micro-machined silicon reflector preform with the high reflectance multilayer sidewall reflector, including the final anodic bonding and gas encapsulation process.	28
Figure 30	Reflectance from a single bulk micro-machined silicon sidewall reflector with and without multilayer reflectors.	30
Figure 31	Optical absorption in the vapor cell under elevated temperature (Tcell) under swept emission from a VCSEL due to the ⁸⁷ Rb D1 atomic transition.....	30
Figure 32	Optical efficiency of the vapor cell and cell preforms during return reflection with and without integrated reflectors.	32
Figure 33	CAD model of physics package.	32
Figure 34	Side view of physics package.....	33
Figure 35	a) CAD model for baseplate with VCSEL chip. b) Baseplate with chip resistor and chip thermistor attached to it, the baseplate is glued to a printed circuit board. The inset in b) shows the VCSEL chip wire bonded to the gold traces in the baseplate.	34
Figure 36	Laser source and optics subassembly.....	34
Figure 37	a) Exploded view of second subassembly. b) Microfabricated Cs vapor cell. c) Heaters. d) Top view of RF coils mounted on printed circuit board. f) Kapton sheets.	35
Figure 38	3D view of vapor cell assembly.	35
Figure 39	Heater configuration on prototype physics package.	36
Figure 39	Low magnetic field heaters.	37
Figure 40	a) Assembled physics package. b) CAD model of physics package.....	38
Figure 41	Dual-beam interrogation method.	38
Figure 42	Interrogation method using a single elliptically polarized beam.	39
Figure 43	a) Original VCSELs. b) New VCSELs.	40
Figure 44	a) Setup. b) Physics package electronics diagram. c) Magnetic resonance signal analysis setup. d) SNR measurement setup.....	43
Figure 45	Lock-in dispersive signal as a function of magnetic field detuning.....	43
Figure 46	Signal to noise ratio (SNR).	44
Figure 47	Magnetometer sensitivity as a function of magnetic resonance linewidth.....	44
Figure 48	Magnetometer frequency response.....	45
Figure 49	Signal to noise ratio (SNR) as a function of optical power.....	47
Figure 50	Magnetometer sensitivity as a function of optical power.	48
Figure 51	Results in the SERF regime	49
Figure 52	Linewidth of the magnetometer resonance as a function of cesium temperature (yellow trace). It has two contributions: Spin-exchange collisions at low cell temperatures (blue trace) and spin-destruction collisions at high cell temperatures (red trace) The red arrow indicates the point where the collision rate between the cesium atoms equals the Larmor frequency in earth's field.....	50
Figure 53	Electronics block diagram for the dual-beam geometry.	51
Figure 54	Electronics block diagram for the single-beam geometry.....	52
Figure 55	Waveform for cell heaters.	53
Figure 56	Required value for the constant, A, for desired power level.....	54
Figure 57	Efficiency of sine wave heating vs sine wave with 3 rd harmonic.	54
Figure 58	Heater amplifier printed circuit board, containing 4 power amplifiers.....	55
Figure 59	Heater amplifier.....	56

Figure 60 Laser modulation VCO.	62
Figure 61 Laser drive amplifier.	63
Figure 62 Photodiode preamplifier.	64
Figure 63 Canonical feedback oscillator.	66
Figure 64 Response of canonical oscillator.	66
Figure 65 More detailed circuit topology of self-oscillating magnetometer	67
Table 1. VCSEL parameters	40
Table 2. Dual-laser approach and single-laser approach comparison.	41
Table 3. Pump signal phase modulation	69
Table 4. Effect of modulation amplitude on signal phase	70
Table 5. Effect of modulation peak amplitude on signal phase.....	70
Table 6. Effect of pump signal on probe signal phase.....	71
Table 7. Required band pass characteristics	72

Acknowledgments

This material is based upon work supported by the Strategic Environmental Research and Development Program (SERDP) through the U.S. Army Corps of Engineers, Humphreys Engineering Center Support Activity under Contract No. W912HQ-07-C-0040. Any opinions, findings and conclusions or recommendations expressed in this material are those of the authors and do not necessarily reflect the views of SERDP or the U.S. Army Corps of Engineers.

Executive Summary

Objective

Magnetometers and electromagnetic (EM) devices are two of the most commonly used instruments for searching for UXO. Research in this area has progressed from the problem of detecting possible UXO items to that of discriminating between hazardous and non-hazardous underground objects. Accurate identification of underground items requires that as much information as possible be gathered about the anomaly. This includes taking a dense array of magnetometer readings as well as EM readings.

The magnetometer sensor of choice is typically an atomic vapor total field magnetometer. These devices have extremely high sensitivity and give readings that are independent of orientation. For EM systems, the sensor of choice has been a wire coil. A coil generates a voltage that is proportional to the time rate of change of the average magnetic field through the coil.

An ideal sensor would combine the advantages of both types of measurement by making a magnetic field reading from DC to about 10 kHz – covering the range of frequencies of both magnetometry and EM systems. In this project we investigated, designed, and prototyped small, wide bandwidth, extremely sensitive total field magnetic sensors. The sensing elements are approximately 20 mm³ in volume and have a noise level of below 10 pT/√Hz. The bandwidth of such devices exceeds 15 kHz, adequate for time or frequency domain electromagnetic (EM) measurements.

Improved bandwidth of a magnetometer also greatly improves the performance of systems measuring the DC magnetic field by allowing for faster sampling rates, and therefore higher density of samples at faster survey speeds. Airborne applications, for example, make good use of high bandwidths.

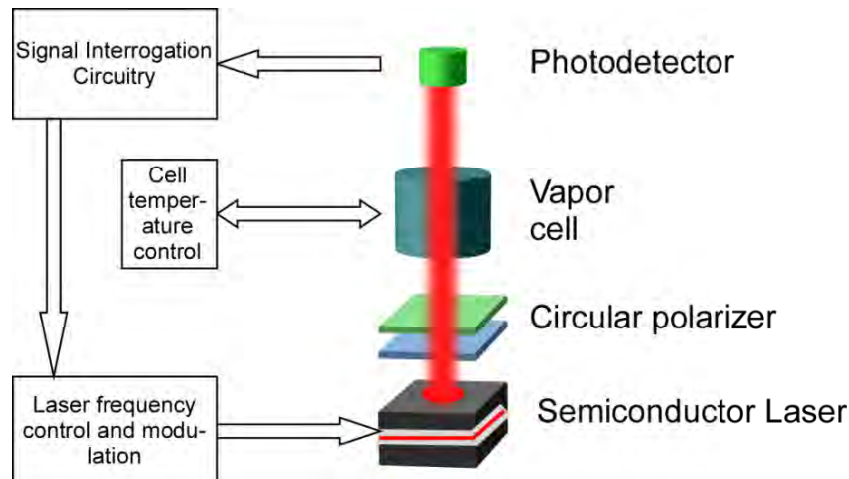


Figure 1. Basic structure of an atomic magnetometer

Recent advances in large-scale laboratory magnetic field sensors have demonstrated unprecedented improvements in device sensitivity^{1,2}. At present, the most sensitive atomic magnetometers, operated in gradiometer mode, achieve sub-fT/√Hz performance that exceeds even that of SQUIDs. In addition, the fundamental limits of sensitivity set by alkali-alkali spin-destruction processes are still two orders of magnitude below currently achieved sensitivity levels. In large part, these extreme sensitivities have been limited by researchers' ability to measure them – environmental noise leaking through reasonably-sized magnetic shields often obscures the device noise.

The fundamental limit to the sensitivity is usually set by spin-exchange collisions between alkali atoms that cause decoherence of the atomic spin precession and therefore broaden the resonance line. This fundamental limit has been stated as³

$$\delta B_{\min} = \frac{1}{\gamma_e \sqrt{n T_2 V t}}$$

where γ_e is the atomic gyromagnetic ratio (3.5 Hz / nT for ¹³³Cs), n is the density of alkali atoms in the cell, T_2 is the alkali spin precession lifetime, V is the volume of the cell and t is the integration time. At high alkali atom densities, the sensitivity of the magnetometer depends only on the volume of the cell as $\sim 1 \text{ fT}/\sqrt{\text{Hz}} \text{ cm}^{3/2}/V^{1/2}$.

Small, low-power sensors are intrinsically less sensitive than their laboratory counterparts. In large part, the reason for this is that atoms confined in small alkali vapor cells interact with the walls of the cell more often than they do in large cells. For a cell of volume 1 mm³, the fundamental spin-exchange-limited sensitivity according to the formula above is roughly 100 fT/√Hz. The bandwidth of the device, however, is limited mainly by the spin-precession lifetime, T_2 . At very high alkali atom densities, therefore, it is possible to generate resonances broadened substantially by spin-exchange collisions, while maintaining the high sensitivity through the increased signal-to-noise ratio created by the higher atom density.

We developed a magnetic field sensor that achieves a high sensitivity simultaneously with high bandwidth, small size and low power. The small size and low power operation is enabled by the use of technology used in micro electro mechanical systems (MEMS). This work complements our previous SERDP-funded work (MM-1512) developing chip-scale atomic magnetometers by examining the physics issues related to future sensor needs of SERDP. The high bandwidth is achieved by operating the alkali vapor cell at a high temperature, so that the alkali density is large and therefore the spin-exchange broadening is large. At a temperature of 130 °C, the alkali atom vapor pressure is roughly 10⁻³ Torr, corresponding to an alkali atom number density of 3×10¹³/cm³, and the spin-exchange linewidth is roughly 50 kHz. In the spin-exchange limit, the sensitivity remains roughly 100 fT/√Hz.

Tasks

The structure of an atomic magnetometer consists of the elements shown in Figure 1. Under SERDP project MM-1512 Geometrics, the National Institute of Standards and Technology (NIST), and Sandia National Laboratories succeeded in miniaturizing the elements of an atomic

magnetometer. In this project, we extended that work by exploring and extending the performance capabilities possible with such devices. The project consisted of the following tasks:

Task 1. Study Magnetometry at High Cell Temperatures

- 1.1 Build prototype cells for initial measurements
- 1.2 Initial measurements of linewidth and sensitivity vs temperature
- 1.3 Demonstration of high performance signal detection.

Task 2. Construction of MEMS Physics Package

- 2.1 Demonstration of angled interiors
- 2.2 Prototyping of MEMS packages
- 2.3 MEMS design and fabrication

Task 3. Implementation of SERF Technique

- 3.1 Investigate SERF in MEMS cells

Task 4. Electronics Development

- 4.1 Physics package control circuitry
- 4.2 Signal interrogation circuit design
- 4.3 Prototype and final design revisions

Summary of Results

We are very pleased with the results from this work, and excited about the potential for these devices. In the first year of this project, we fabricated the initial devices to be used in further testing for the fundamental performance. This included fabricating a range of small cells with various buffer gas pressures to study the performance of miniature magnetometers at high cell temperatures.

Measurements of the linewidth of the Larmor resonance confirmed that in Cs, a magnetometer bandwidth of 10 kHz can be achieved at a cell temperature of 135 °C. This was achieved in a cell containing Cs and ~350 Torr N₂. Measurements also confirmed the increased bandwidth that can be achieved at higher alkali atom densities.

Measurements as a function of cell temperature confirmed that at a cell temperature of 135 °C, the linewidth is dominated by spin-exchange collisions. This implies that the magnetometer is indeed operating in the appropriate high-density regime. We have also measured the magnetometer signal size as a function of the cell temperature. We found that at temperatures above ~ 100 °C, the signal does not continue to increase proportionally with the alkali density, but begins to saturate. This saturation is consistent with the effects of optical thickness in the cell, and was not unexpected.

In the first year of the project, we measured the sensitivity and linewidth attainable with a single laser beam. We noticed the sensitivity dropping due to the optical thickness of the cells, and did

not yet reach the program goals. We determined a more complicated dual-beam method was required, to pump the cell and probe it with different wavelengths.

In the second year we investigated novel schemes of probing the cell in a manner circumventing the difficulty due to the optical thickness. We used a dual-laser configuration, in which one laser is used to pump the atoms, while a second probe laser, linearly polarized and tuned off resonance, measures the atomic polarization via magneto-optical polarization rotation. Since the polarization rotation can be generated by pure phase shifts of the optical field, the probe can be strongly detuned from resonance, leading to reduced absorption and a corresponding reduction of the loss of sensitivity due to the cell optical thickness. The results, shown below, indicate that even extremely small sensors may simultaneously achieve high sensitivity and wide bandwidth.

Absorption (cell temp)	Sensitivity	Bandwidth
Single Laser Beam:		
28%	15 pT	3kHz
64%	35pT	4.5 kHz
82%	100pT	6.5 kHz
Dual Beam Method:		
82%	10pT	15kHz

Figure 2 Summary of performance measurements at various cell temperatures. Increasing the cell temperature increases the absorption. Using the dual-beam method allows for performance congruent with the project’s original goals.

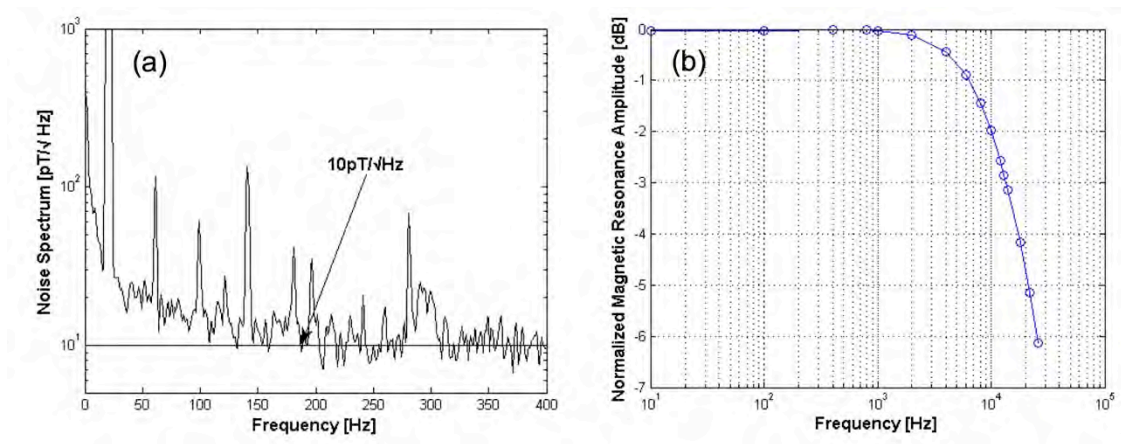


Figure 3 (a) Sensitivity of the wideband magnetometer: 10 pT /√Hz between 100 and 400 Hz. (b) Bandwidth of the wideband magnetometer: 15 kHz.

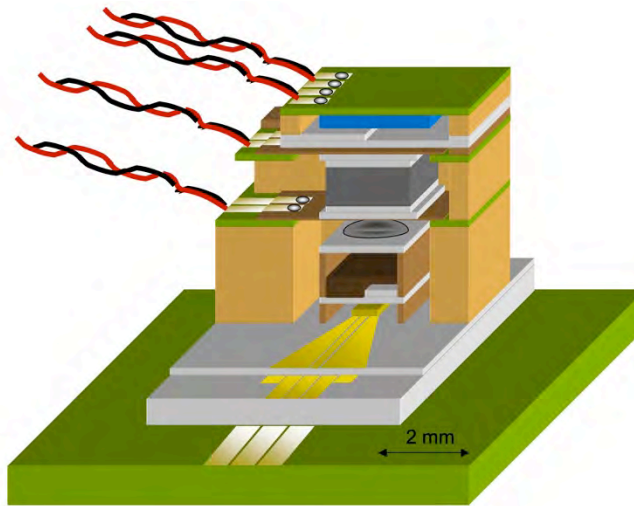


Figure 4 Sketch of MEMS physics package design which was built in this project.

In addition to the progress in evaluating the fundamental limits to the performance of the devices at high cell temperatures, we investigated several MEMS designs for devices, an example of which is shown in Figure 4. In addition, MEMS-based alkali vapor cells have been developed with internal surfaces which reflect light by approximately 90° from the vertical direction into the horizontal. High-reflection optical coatings have also been demonstrated, so that optical losses incurred in the propagation of the light through the cell are minimized. These cells appear suitable for magnetometers in which the pump and probe fields must propagate in perpendicular directions.

We also demonstrated magnetometry in the spin-exchange relaxation free (SERF) regime in a millimeter-scale alkali vapor cell. This measurement resulted in a sensitivity of $70 \text{ fT}/\sqrt{\text{Hz}}$ with a bandwidth of 290 Hz using a very simple excitation/detection scheme based on the optical absorption of a single laser beam. In this experiment the cell temperature was 152°C , with further increase in the cell temperature limited by the optical thickness effect described above. If the polarization-rotation solution can be applied in this situation, it seems likely that the bandwidth of the sensor could be increased significantly by operating at even higher cell temperatures with little loss in sensitivity.

We further built a prototype sensor exploring avenues for the fabrication of miniature physics packages.

Finally, we designed and prototyped electronics circuitry for operating the systems at wide bandwidth.

We had originally intended to build a complete system that could be tested in the field with an electromagnetic source. However, we encountered difficulties with manufacturing our prototype sensors (primarily with the heating elements) which prevented us from ultimately fabricating a

complete prototype sensor package. In addition, the electronics system proved to require a much more complicated digital control system than we were able to build. However, in the work that we did towards those goals, we achieved an excellent understanding of the requirements for these systems, and ultimately designed other approaches that are being implemented in follow-on projects and commercial products.

Objective

In this project we investigated and developed small, wide bandwidth, extremely sensitive total field magnetic sensors. The sensing elements are approximately 20 mm³ in volume and have a noise level of about 10 pT /√Hz. The bandwidth of such devices exceeded 15 kHz, impressive for rapidly acquired static magnetic field measurements and adequate for time or frequency domain electromagnetic (EM) measurements.

This was done by extending techniques that were developed by our own work and that of other researchers. Recent advances in large-scale laboratory magnetic field sensors have demonstrated unprecedented improvements in device sensitivity^{1,2}. At present, the most sensitive atomic magnetometers, operated in gradiometer mode, achieve sub-fT/√Hz performance that exceeds even that of SQUIDS. In addition, the fundamental limits of sensitivity set by alkali-alkali spin-destruction processes are still two orders of magnitude below currently-measured levels. In large part, these extreme sensitivities have been limited by researchers' ability to measure them – environmental noise leaking through reasonably-sized magnetic shields often obscures the device noise.

The fundamental limit to the sensitivity is usually set by spin-exchange collisions between alkali atoms that cause decoherence of the atomic spin precession and therefore broaden the resonance line. This fundamental limit has been stated as³

$$\delta B_{\min} = \frac{1}{\gamma_e \sqrt{n T_2 V t}}$$

where γ_e is the atomic gyromagnetic ratio (3.5 Hz/nT for ¹³³Cs), n is the density of alkali atoms in the cell, T_2 is the alkali spin precession lifetime, V is the volume of the cell and t is the integration time. At high alkali atom densities, the sensitivity of the magnetometer depends only on the volume of the cell as $\sim 1 \text{ fT}/\sqrt{\text{Hz}} \text{ cm}^{3/2}/V^{1/2}$.

Small, low-power sensors are intrinsically less sensitive than their laboratory counterparts. In large part, the reason for this is that atoms confined in small alkali vapor cells interact with the walls of the cell more often than they do in large cells. For a cell of volume 1 mm³, the fundamental spin-exchange limited sensitivity according to the formula above is roughly 100 fT/√Hz. The bandwidth of the device, however, is limited mainly by the spin-precession lifetime, T_2 . At very high alkali atom densities, therefore, it is possible to generate resonances broadened substantially by spin-exchange collisions, while maintaining the high sensitivity through the increased signal-to-noise ratio created by the higher atom density.

We built a magnetic field sensor that achieved high sensitivity simultaneously with high bandwidth, small size and low power. The small size and low power operation was enabled by the use of technology used in micro electro mechanical systems (MEMS)⁴. This work complements our previous SERDP-funded work developing chip-scale atomic magnetometers by

examining the physics issues related to future sensor needs of SERDP. The high bandwidth is achieved by operating the alkali vapor cell at a high temperature, so that the alkali density is large and therefore the spin-exchange broadening is large. At a temperature of 130 °C, the alkali atom vapor pressure is roughly 10^{-3} Torr, corresponding to an alkali atom number density of $3 \times 10^{13}/\text{cm}^3$, and the spin-exchange linewidth is roughly 50 kHz. In the spin-exchange limit, the sensitivity remains roughly 100 fT/ $\sqrt{\text{Hz}}$. Preliminary measurements demonstrating the increased bandwidth that can be achieved at higher alkali atom densities are shown in Figure 5.

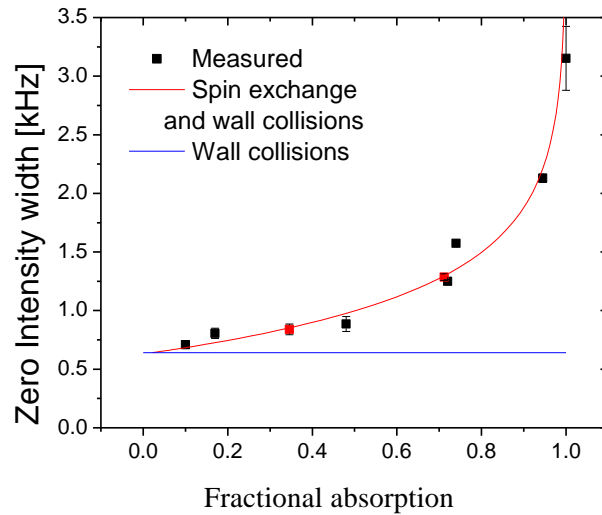


Figure 5 Linewidth of the alkali atom spin resonance as a function of the fraction of absorbed light, which is related to the alkali atom density. The increased linewidth at high densities leads to a magnetic field sensor with a higher bandwidth

Additional improvement in sensitivity can be obtained using the technique of spin-exchange suppression⁵, in which strongly polarized alkali atoms at high density interact in a weak magnetic field. In this regime, spin-exchange interactions are suppressed allowing a potential improvement in the sensitivity by a factor of about 30 to about 3 fT/ $\sqrt{\text{Hz}}$ in a cell of volume 1 mm³. This additional suppression is very difficult to measure in a conventional large cell since even Barkhausen noise from magnetic shields disrupts the atomic spins at a higher rate than Cs-Cs collisions. However, in highly compact cells, where the decoherence due to wall collisions is more rapid, this sensitivity gain may be observable and even useful.

Background

Sensitivity, bandwidth and size are in some ways complementary qualities in an atomic magnetometer. Atomic magnetometers are based on a precise measurement of the precession of the spins of atoms with one valence electron (alkali atoms) in a magnetic field. Since the atomic spin has a magnetic moment, the spin precession frequency is proportional to the field experienced by the atom, at least for weak magnetic fields: $\nu_0 = \gamma_e B_0$, where γ_e is the gyromagnetic ratio of the atom (3.5 Hz/nT for Cs atoms) and B_0 is the magnetic field at the location of the atoms. When the atoms are driven at this frequency ν_0 (for example, by applying an oscillating magnetic field) they all precess in phase with the driving field and collectively produce a measurable precessing magnetic moment, which can be detected with a probe beam. When confined in a vapor cell, the atoms also undergo a variety of decoherence events that cause their spin precession frequency to deviate from perfect sinusoidal motion. These events include collisions with other atoms and the walls of cell, and the effects of inhomogeneous magnetic fields. The rate and magnitude of the decoherence process can be characterized by a decoherence time, T_c , which determines the width $\Delta\nu$ of the resonant behavior of the spin precession in the frequency domain: $\Delta\nu = 1/\pi T_c$.

The decoherence time and corresponding resonance width determine both the sensitivity and the bandwidth of the magnetometer. The sensitivity can be expressed as

$$\delta B_{\min} = \frac{1}{\gamma_e T_c (SNR)} \quad (1)$$

where SNR is the signal-to-noise ratio. Thus, for a fixed signal-to-noise ratio, longer decoherence times imply a more well-defined precession frequency and therefore a higher magnetometer sensitivity. The bandwidth of the magnetometer on the other hand, is determined by the spectrum of the atomic response and therefore by the resonance width $\Delta\nu$. This can be seen by considering the response of the driven atomic system to a fast change in the DC field, B_0 , that defines the spin precession frequency with the condition that the driving frequency is kept constant. The steady state to which the system evolves is one in which the atomic spins still precess at the driving frequency but do so with a different amplitude and phase. Although the natural precession frequency of the atoms changes instantaneously with the DC field, the atoms' altered response to the driving field has a time constant equal to the transverse decoherence time of the spins. Therefore the effective bandwidth of the magnetometer is limited to $1/T_c$.

Thus we see that at a fundamental level, the magnetometer sensitivity and bandwidth are interrelated through the atomic coherence time, T_c . Frequently, high sensitivity is achieved at the expense of bandwidth by increasing T_c to as large a value as possible, for example by putting the atoms in a large cell to reduce the wall-induced contributions to the decoherence¹. This is the case for a recent magnetometer which achieved a sensitivity below 1 fT/ $\sqrt{\text{Hz}}$ by increasing the value of T_c to near 1 s^{2,3}.

As mentioned above, collisions of the atoms with the cell walls are a primary source of decoherence. Normally, a buffer gas is introduced into the cell to reduce the collision rate of atoms with the walls. In this case the atoms diffuse through the cell (which, for purposes of analysis, we assume to be a sphere), which reduces the collisional decoherence from the walls,

but adds collisional decoherence from the buffer gas atoms. The coherence time can in this case be described by

$$\frac{1}{T_c} = \frac{\pi^2}{R^2} D + n_{bg} \sigma_{bg} v, \quad (2)$$

where D is the diffusion constant of the alkali atoms in the buffer gas, R is the radius of the cell, n_{bg} is the density of buffer gas atoms, σ_{bg} is the collision cross-section of the alkali atoms with the buffer gas atoms, and v is the thermal velocity of the atoms. The first term in Eq. (2) is due to diffusion to the cell walls, while the second term is due to collisions with the buffer gas. It can therefore be seen that large cells lead naturally to long values of T_c and therefore result in magnetometers with high sensitivity and low bandwidth. Small cells, on the other hand, imply short coherence times and therefore lower sensitivity and higher bandwidth⁶.

As can be seen from Eq. (1), it is also possible to increase the sensitivity by improving the signal-to-noise ratio. In this case, the magnetometer bandwidth is not directly affected. The easiest way to affect the signal-to-noise ratio (SNR) is to change the number of atoms participating in the measurement. The value of SNR is limited at a fundamental level by shot noise in the measurement of the atom number: it is possible to measure $N_{at}=n_{at}V$ atoms per coherence time and therefore $SNR \propto \sqrt{N_{at}/T_c}$. Here V is the volume of the cell and n_{at} is the density of alkali atoms, which is determined by the operating temperature of the cell. This leads to a sensitivity of

$$\delta B_{\min} \propto \frac{1}{\gamma_e \sqrt{T_c n_{at} V}} = \frac{\sqrt{\Delta \nu}}{\gamma_e \sqrt{\pi n_{at} V}}. \quad (3)$$

The atom-shot-noise limited sensitivity as a function of magnetometer bandwidth is plotted in Figure 6 along with experimental data from some recent experiments.

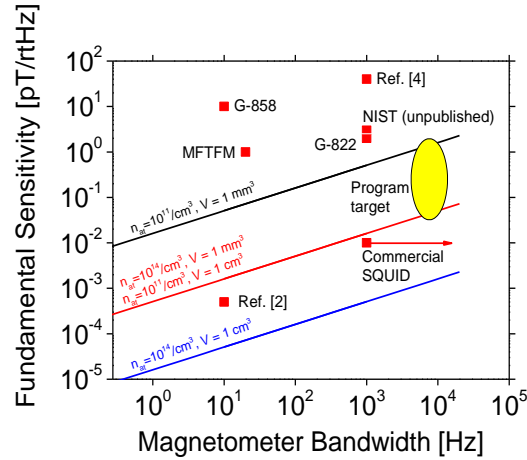


Figure 6 Fundamental magnetometer sensitivity as a function of measurement bandwidth. The vapor density of ^{87}Rb is $10^{11}/\text{cm}^3$ at $\sim 60^\circ\text{C}$ and $10^{14}/\text{cm}^3$ at $\sim 180^\circ\text{C}$. The point labeled MFTFM refers to the results of SERDP project MM-1512.

It is clear from Eq. (3) that high sensitivity is achieved with large cell volumes and high atom densities. However, there is an important limit to how high the atom density can be made. This limit is set by spin-exchange collisions between alkali atoms themselves, which dominate the spin decoherence when the alkali density is high. In this limit, the spin decoherence time is

$$\frac{1}{T_c} = n_{at} \sigma_{SE} v, \quad (4)$$

where σ_{SE} is the alkali-alkali spin exchange cross section (roughly equal to $2 \times 10^{-14} \text{ cm}^2$ for Cs) and v is the thermal velocity of the atoms. The magnetometer sensitivity is then independent of atom density since the improvement gained through increased signal-to-noise is offset by the increasing line width of the atomic resonance:

$$\delta B_{\min} \propto \frac{\sqrt{\sigma_{SE} v}}{\gamma_e \sqrt{V}}. \quad (5)$$

Thus, the optimal strategy for attaining the best possible sensitivity is to first reduce the cell decoherence rate (Eq. 2) to as low as possible (the largest cell), and then to increase the alkali atom density (by raising the temperature) until the spin-exchange decoherence rate (Eq. 4) is roughly equal to the cell decoherence rate. In this limit, the magnetometer sensitivity is determined only by the cell volume (see Eq. 5). By increasing the alkali density even more, one finds that the sensitivity is largely unaffected, whereas the device bandwidth increases as the line width increases.

A difficulty with this strategy in large cells is that as the alkali atom density increases, so does the optical absorption. As a result, it becomes more difficult to optically pump the atomic sample and detect the precessing polarization. An advantage is therefore gained through the use of very small vapor cells, which allow light to propagate into the interior even when the alkali density is high. In addition, the small size of the cell does not affect the sensitivity in the high density/high bandwidth regime since spin-exchange broadening is already large. A new optimization strategy therefore emerges, that enables both high bandwidth operation and high sensitivity in a very small cell volume. This strategy is as follows:

1. Determine the sensitivity/bandwidth values, according to Figure 6, taking into account that higher operating temperatures require larger electrical power to heat.
2. From the bandwidth value, determine the size of the cell and buffer gas pressure such that the wall- and buffer gas-induced collisions result in a decoherence rate equal to the desired bandwidth.
3. Operate the cell at a temperature such that the spin-exchange broadening is roughly equal to the cell broadening

Under these conditions, the sensitivity will be roughly equal to the fundamental limit set by Eq. (5), if the atomic signal can be detected with shot-noise limited precision.

This range of parameters has been largely unexplored because a) sensitivity has been deemed more important than device bandwidth for many applications and b) it has been difficult until now to fabricate highly miniaturized vapor cells. However, for geophysical applications in which the device is unshielded and the background noise level is in the range of $1 \text{ pT}/\sqrt{\text{Hz}}$, a magnetometer more sensitive than this is of little use. We are therefore willing to sacrifice some of the sensitivity that can be obtained in large devices for higher bandwidth and small size, both of which are important for geophysical applications.

One method we investigated of probing the resonance in an optically thick atomic sample was through the use of sidebands on the optical pumping laser generated through modulation of the laser injection current. In addition to providing a narrow-band light source with reduced electrical power requirements, the laser therefore serves an additional purpose, which is to enable the generation of both resonant and off-resonant optical fields. The injection current of the laser is modulated at a frequency such that either the first-order or higher-order sidebands are detuned from the resonance sufficiently to be transmitted through the vapor. Thus, the carrier can be mostly absorbed by the vapor and serves to optically pump the atoms into their polarized state and the sidebands can simultaneously be used to probe the precession of the atomic spins.

In the optical configuration shown in Figure 7 part of the diverging optical field emitted by the laser is reflected by the angled interior wall of the vapor cell and propagates in a direction perpendicular to the pump field. Because the sample is optically thick and there is a significant component of the atomic polarization in the longitudinal direction created by the pump beam, the carrier frequency of this reflected probe beam is strongly absorbed and produces almost no signal. However, the sidebands are transmitted and undergo a rotation of their polarization that depends on the precessing transverse polarization. By monitoring the polarization rotation of the probe beam using a second polarizer angled at 45° with respect to the initial light polarization, it is therefore possible to measure the transverse polarization with near shot-noise limited sensitivity.

Polarization rotation in a transversely-polarized atomic sample has been used frequently in the past⁷ to measure atomic polarization with a sensitivity close to the atom-shot noise limit. In this work we demonstrated that this technique can be used in the configuration described above, with the off-resonant light fields generated by a modulated semiconductor laser and directed into the transverse direction with the angled interior cell wall.

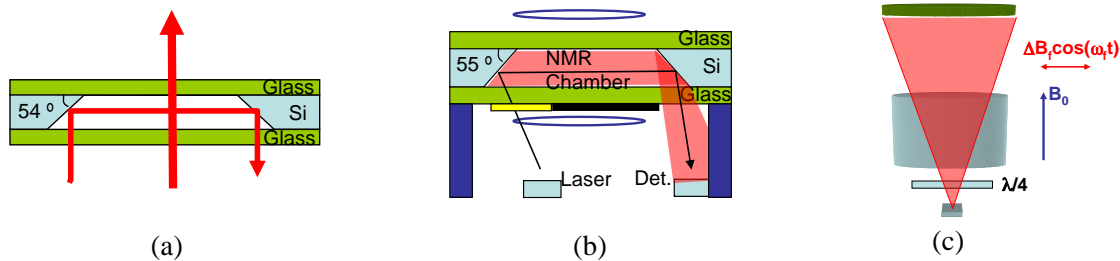


Figure 7 MEMS designs for chip-scale atomic magnetometers. (a) Cell design for achieving orthogonally propagating beams in a MEMS cell. (b) A design allowing implementation of the two-beam Mx and two-beam Mz geometries. (c) A design allowing implementation of the one-beam Mz geometry.

Materials and Methods

This project extends the work done in MM-1512, by using additional techniques developed by ourselves and other researchers. Recent advances in large-scale laboratory magnetic field sensors have demonstrated unprecedented improvements in device sensitivity. At present, the most sensitive atomic magnetometers, operated in gradiometer mode, achieve $\text{sub-fT}/\sqrt{\text{Hz}}$ performance that exceeds even that of SQUIDs. In addition, the fundamental limits set by alkali-alkali spin-destruction processes are still two orders of magnitude below current levels. In large part, these extreme sensitivities have been limited by researchers' ability to measure them – noise due to reasonably-sized magnetic shields often obscures the device noise.

The fundamental limit to the sensitivity is usually set by spin-exchange collisions between alkali atoms that cause decoherence of the atomic spin precession and therefore broaden the resonance line. At high alkali atom densities, the sensitivity of the magnetometer is inversely proportional to the square root of volume of the cell.

Hence, small sensors are intrinsically less sensitive than their laboratory counterparts. The reason for this is that atoms confined in small alkali vapor cells interact with the walls of the cell more often than they do in large cells. For a cell of volume 1 mm^3 , the fundamental spin-exchange limited sensitivity is roughly $100 \text{ fT}/\sqrt{\text{Hz}}$. The bandwidth of the device, however, is limited mainly by the spin-precession lifetime. At very high alkali atom densities, it is possible to generate resonances broadened substantially by spin-exchange collisions, while maintaining high sensitivity through the increased signal-to-noise ratio created by the higher atom density.

High densities will be achieved by operating the alkali vapor cell at a high temperature, so that the spin-exchange broadening is large, and therefore the bandwidth is high. At a temperature of $130 \text{ }^\circ\text{C}$, the alkali atom vapor pressure is roughly 0.001 Torr , corresponding to an alkali atom number density of $3 \times 10^{13}/\text{cm}^3$, and the spin-exchange line width is roughly 50 kHz . In the spin-exchange limit, the sensitivity remains roughly $100 \text{ fT}/\sqrt{\text{Hz}}$.

In this project, we extended the measurement of magnetometer performance using microfabricated cells into the higher temperature regime. We found that at higher temperatures simultaneous high sensitivity and wide bandwidth could be obtained. In addition, another regime, known as the Spin Exchange Relaxation Free (SERF) regime was explored. The SERF regime exists at magnetic field strengths lower than the Earth's field. Hence, some coils are required to null out the Earth's field. However, large sensitivities are obtainable in this regime, and the resulting sensors measure a vector component of the field. Thus, these sensors are quite different than other atomic magnetometers, and this work is therefore quite interesting.

Results and Accomplishments

There were four major tasks in our work on this project:

1. Magnetometry at High Cell Temperatures
 - a. Build prototype cells for initial measurements
 - b. Initial measurements of linewidth and sensitivity as a function of temperature
 - c. Demonstration of high performance signal detection
2. Construction of MEMS Physics Packages
 - a. Demonstration of angled interiors
 - b. Prototyping of MEMS physics packages
 - c. MEMS design and fabrication
3. Implementation of SERF Technique
 - a. Initial investigation
 - b. Further investigation
4. Electronics Development
 - a. Physics package control circuitry
 - b. Signal interrogation circuit design
 - c. Prototype and final design revisions

During this project, we were highly successful in demonstrating the potential of these devices and understanding the issues involved. Due to the extra complexity encountered in the practice of fabricating prototypes of the cell and electronics, we did not demonstrate a complete system as we had hoped. However, major milestones included:

1. Understanding the issues of optically pumping and probing miniature cells at high cell temperatures.
2. Methods of addressing the high optical absorption at these temperatures were demonstrated.
3. Several MEMS physics packages were made, allowing us to compare cell performance with different buffer gas pressures.
4. Results consistent with the projects goals were obtained with a dual-beam interrogation method in a bench-top environment
5. A physics package design was completed, and portions were fabricated. Practical constraints did not allow us to build a final complete prototype sensor .
6. Several designs for the electronics systems were prototyped and analyzed. We performed a thorough analysis of the requirements for the electronics systems. Some requirements turned out to be impractical to implement at a reasonable cost in a discrete design but could be implemented using integrated circuit techniques.
7. Overall, we showed it is possible to simultaneously achieve wide bandwidth and high sensitivity, and characterized several techniques for doing so with significant commercial potential.

Task 1. Investigation of Magnetometry at High Cell Temperatures

1.1 Build prototype cells for initial measurements

We fabricated a variety of MEMS-based vapor cells using the ampoule filling technique for testing at high cell temperatures. With this technique, the cell preform, consisting of a cm-scale piece of silicon 1 mm thick and with a 1 mm hole etched in it, is placed into a vacuum chamber. An ampoule containing CsCl and BaN₆ is positioned over the cell inside the chamber so that the neck of the ampoule is over the cell cavity. The ampoule is heated to ~ 150 °C causing the following reaction to occur: $\text{CsCl} + \text{BaN}_6 \rightarrow \text{Cs} + \text{BaCl} + 3\text{N}_2$. The N₂ is pumped away by the vacuum pump and the BaCl (a solid at room temperature) stays in the ampoule. The Cs accumulates at the neck of the ampoule and some Cs is deposited into the bottom of the cell preform. The ampoule is then moved away from the cell preform and a second glass wafer moved to be in contact with the upper surface of the Silicon. The chamber is then backfilled with a buffer gas of an appropriate pressure and the second glass wafer is then anodically bonded to the top Si surface sealing the Cs and the buffer gas inside the cell. A photograph of a typical cell is shown in Figure 8(b).

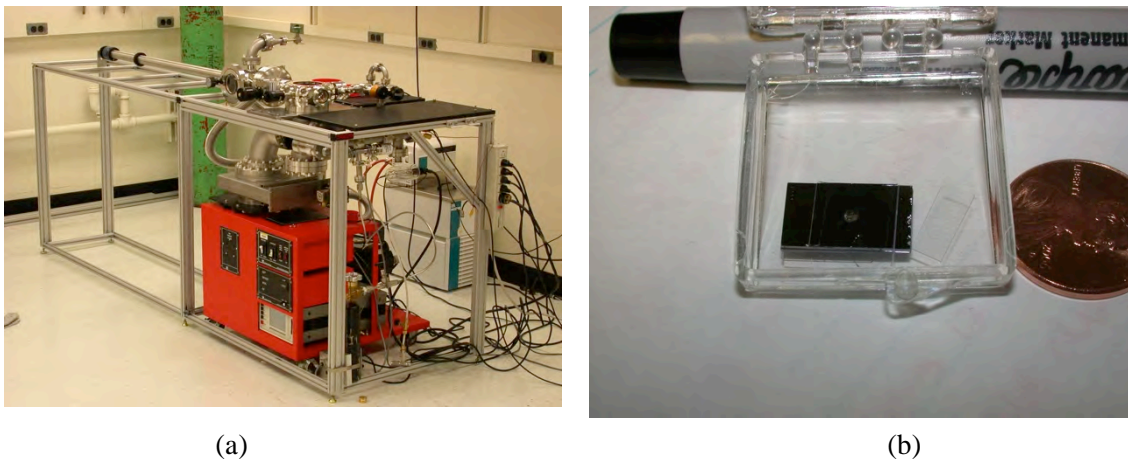


Figure 8 (a) Cell fabrication apparatus at NIST used for producing millimeter-scale alkali vapor cells. (b) Photograph of a typical Cs vapor cell.

The presence of Cs and the buffer gas pressure are confirmed through a measurement of the optical absorption spectrum of the cell. A laser is tuned roughly to the optical resonance in Cs at 894 nm and the laser frequency swept over the transition. The optical spectra from these cells are shown in Figure 9. The buffer gas pressure can be deduced from the width and shift of the optical spectra and corresponds to between 1000 and 1500 Torr of buffer gas.

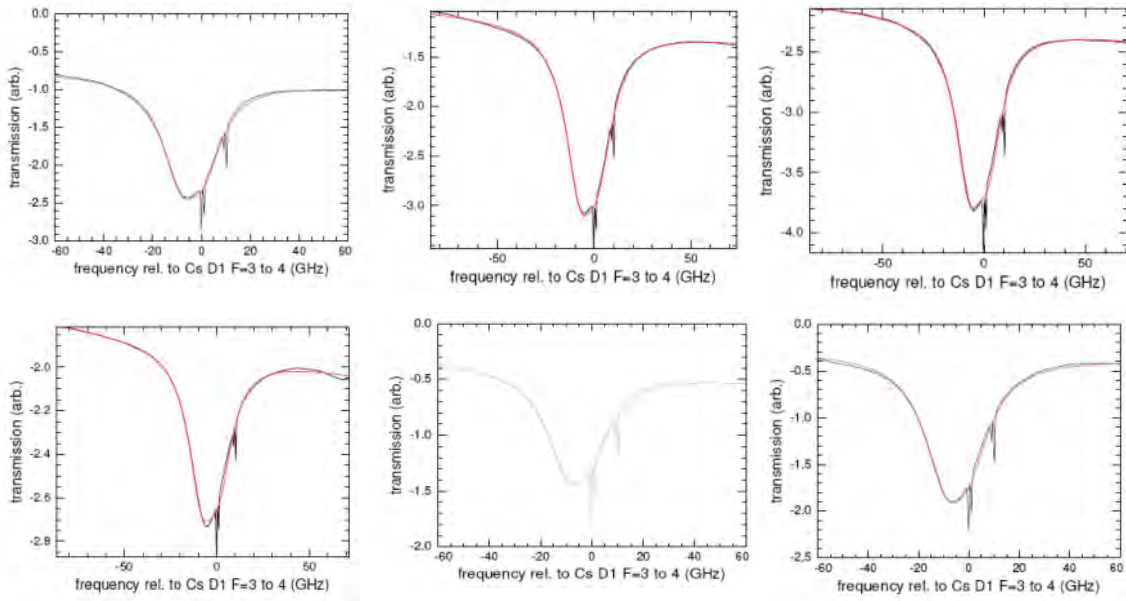


Figure 9 Optical absorption spectra from six MEMS Cs vapor cells. The sharp features in each spectrum are the absorption lines from a large cell with no buffer gas for frequency calibration.

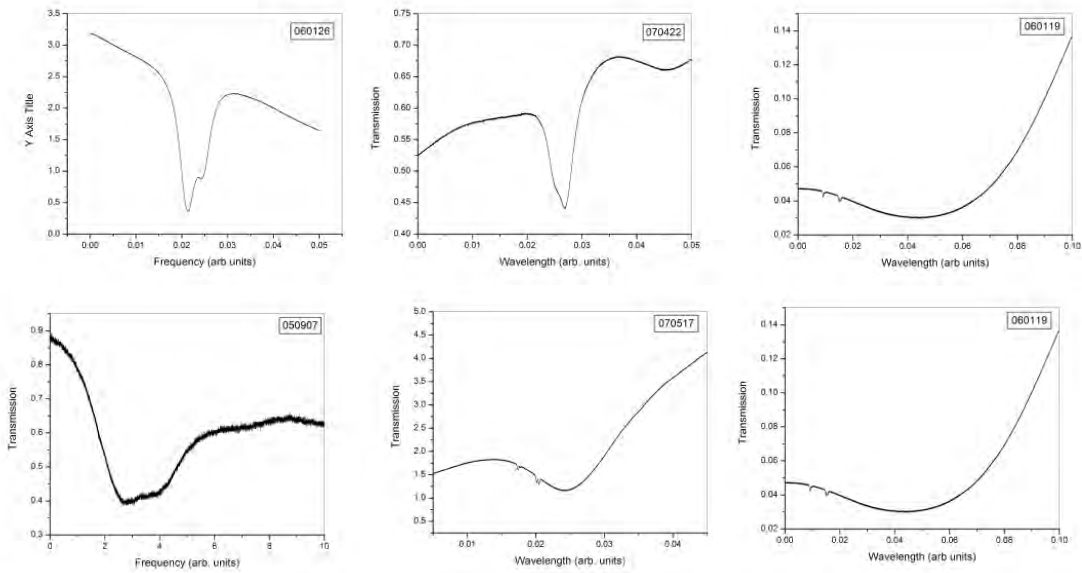


Figure 10 Optical absorption spectra from six MEMS Cs vapor cells at different buffer gas pressures. Increasing the buffer gas pressure broadens the optical linewidth considerably. The curves show are for a range of buffer gas pressure from 150 to 3000 Torr.

1.2 Initial measurements of linewidth and sensitivity as a function of temperature

We have explored three methods of interrogating the signal, measuring sensitivity and bandwidth as a function of cell temperature. The three methods are known as the Mz, Bell Bloom, and Mx methods. The three methods differ in the manner in which the Larmor frequency modulation is fed into cell. The Mx and the Mz method use coils to feed the modulation at the Larmor precession frequency. In the Bell-Bloom method, the laser light beam is either frequency or amplitude modulated at the Larmor frequency.

❖	Mz
➤	DC signal
➤	Equatorial dead zones
➤	Possible spin-exchange suppression
❖	Bell-Bloom
➤	AC signal
➤	Polar dead zone
➤	Frequency-modulated light
❖	Mx
➤	AC signal
➤	Equatorial and polar dead zones

Figure 11 Characteristics of three methods of signal modulation and extraction

Mz Magnetometer

This method uses a coil structure and an electronic feedback signal at the Larmor frequency. The DC absorption level rises sharply as the feedback signal approaches the resonance frequency. The electronics are more complex, but it does not require careful alignment between the coil axis and the optical axis. In addition, this method has an equatorial dead zone. Because this method is more complex, and has a disadvantageous dead zone, we did not pursue this method in detail in this work.

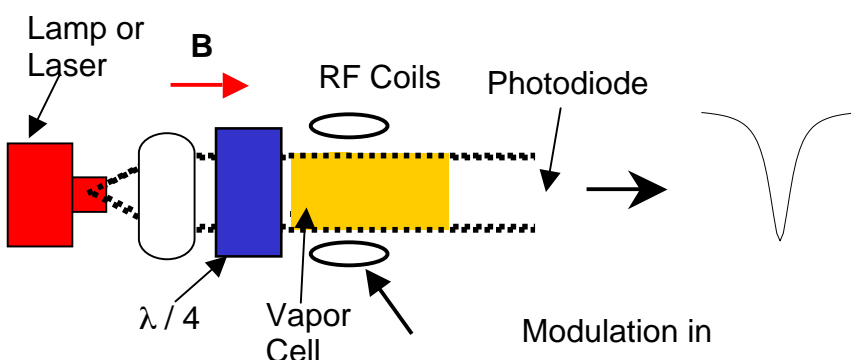


Figure 12 Mz Technique

Bell-Bloom Magnetometer

In the Bell-Bloom method, the modulation (either of frequency or intensity) is applied to the light itself. Therefore, no coils are needed, making the structure simpler and there is no equatorial dead zone. In the original method, which we call the Full-Frequency method, the modulation is applied at the Larmor frequency. This makes the electronics more complicated, and has other disadvantages. Therefore, we investigated a new method, where the modulation is at half the Larmor frequency, and a beat signal at the Larmor frequency is detected at the photodiode. This simplifies the electronics, at some expense of sensitivity. Still, the sensitivity is a very good 20 pT / $\sqrt{\text{Hz}}$. Since this results in a good performance magnetometer with only a polar dead zone and a very simple device structure, this is one of the methods we chose to implement.

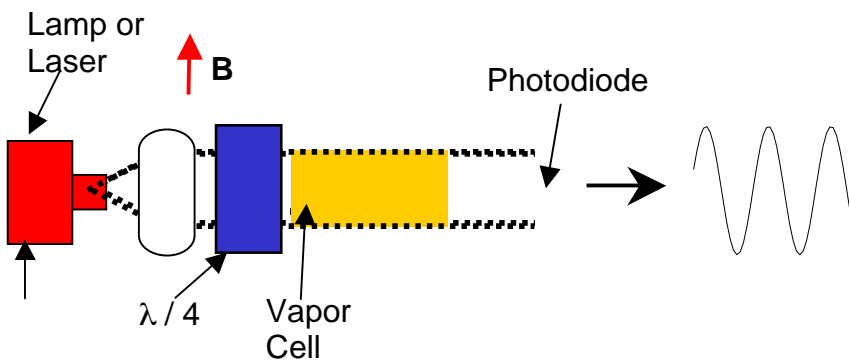


Figure 13 Bell-Bloom Technique

Bell Bloom Measurements

Results using the Bell Bloom modulation technique have been extensively investigated, using various waveforms to modulate the frequency of the laser. Results are shown in the figures below:

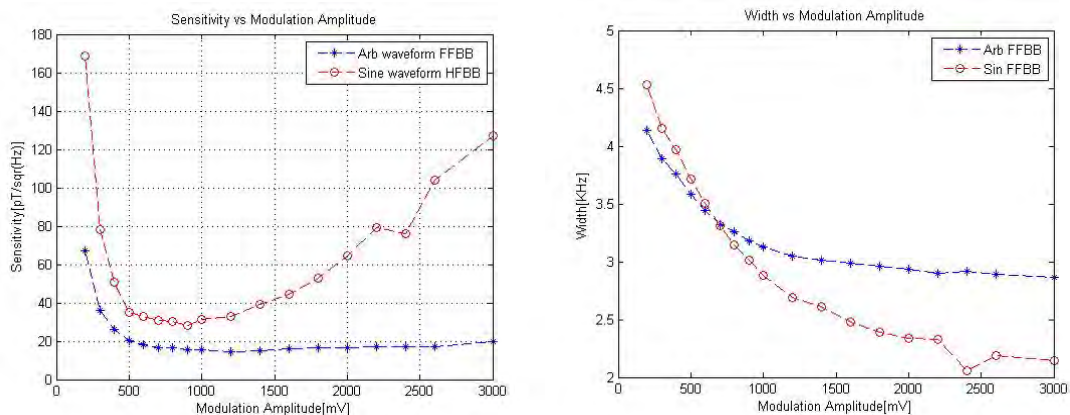


Figure 14 Sensitivity and Bandwidth at 28% absorption

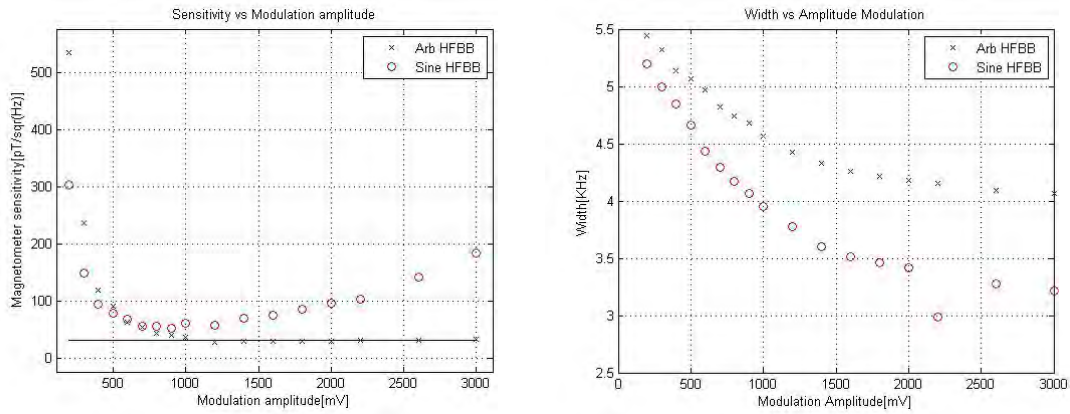


Figure 15 Sensitivity and Bandwidth at 64% absorption

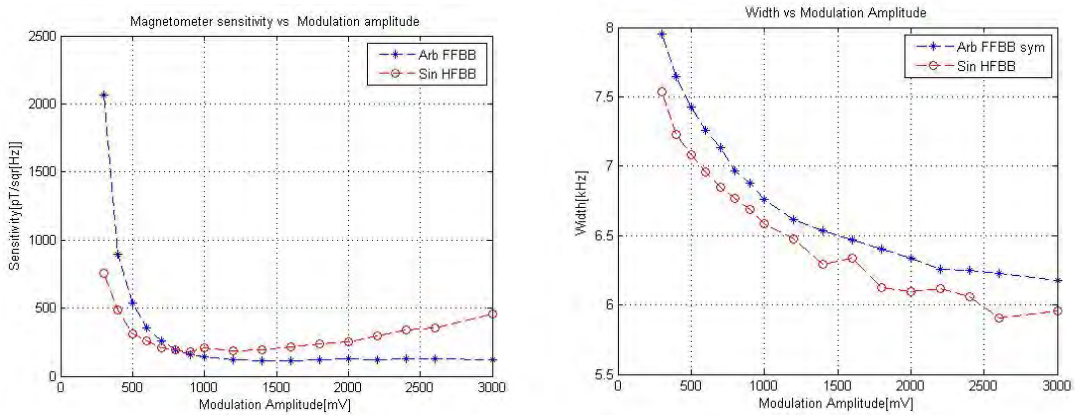


Figure 16 Sensitivity and Bandwidth at 82% absorption

Absorption (cell temp)	Sensitivity	Bandwidth
28%	15 pT	3kHz
64%	35pT	4.5 kHz
82%	100pT	6.5 kHz

Figure 17 Summary of performance measurements with the Bell Bloom method at various cell temperatures. Increasing the cell temperature increases the absorption.

Mx Magnetometer

This method of signal extraction is used by many commercial magnetometers, including the Geometrics G-858, for example. This method uses a coil of wire to apply a signal at the Larmor resonance (near 100-300kHz) to the atoms in the cell to modulate the population. The received signal is also at the Larmor frequency, in contrast to the Mz method. The electronics are more easily implemented, but the feedback coil axis must be carefully aligned with the optical axis to avoid significant heading errors. In addition, this method has both equatorial and polar dead zones. However, for small cells, this method proved to have the best sensitivity.

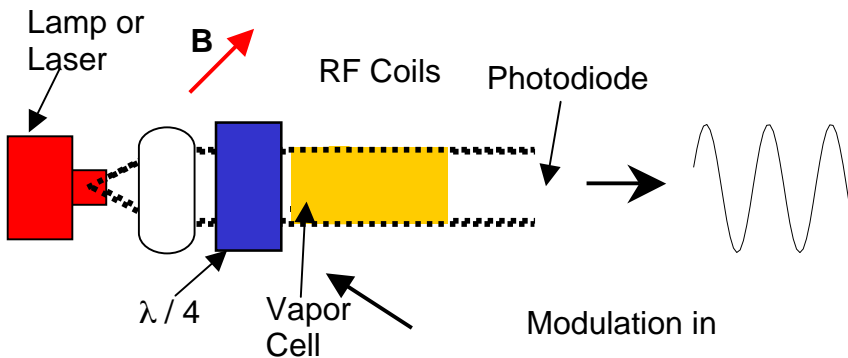


Figure 18 Mx Technique

We investigated the variation of the linewidth and signal size as a function of cell temperature. The cell temperature was elevated to the point that the cell became optically thick. A circularly polarized laser beam was directed into the cell to optically pump the atoms and a static magnetic field was applied oriented at 45 degrees with respect to the optical axis. A transverse RF field was applied and the magnetic field was scanned such that the Larmor frequency of the atoms swept over the frequency of the RF drive. The power transmitted through the vapor cell was detected with a silicon photodiode and demodulated with a lock-in amplifier. The in-phase and out-of-phase signals were observed on an oscilloscope, as shown in Figure 19.

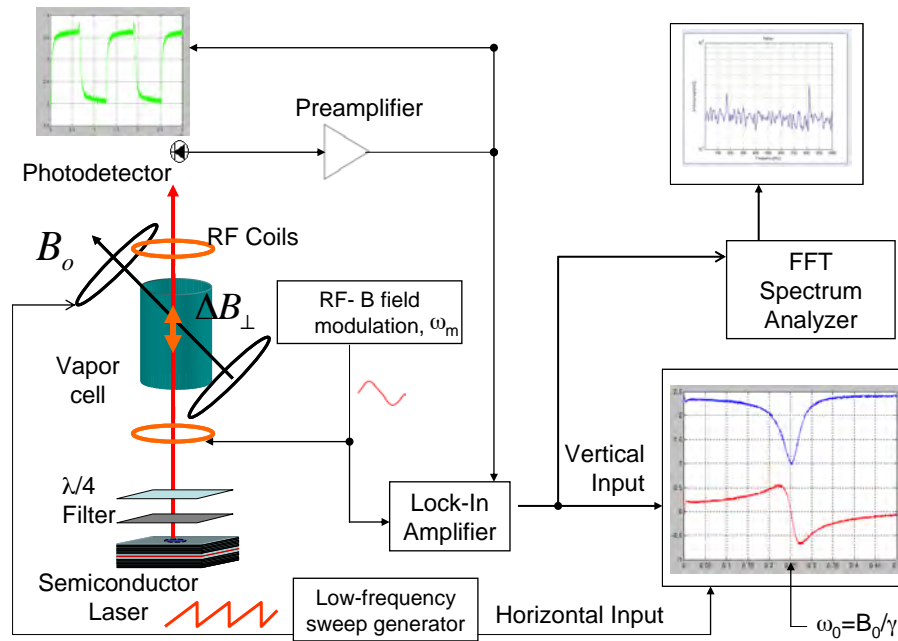


Figure 19 Experimental setup for measurement of the magnetometer signals at high cell temperature.

The width and height of the resonance was measured as a function of the temperature of the vapor cell and the intensity of the incident polarizing laser field. The height of the resonance was normalized to the optical absorption of the atoms in an unpolarized state. The unpolarized state was achieved either by applying a very large DC field or by reducing the optical intensity such that the optical pumping rate was much less than the atomic spin relaxation rate.

In Figure 20(a) the zero-intensity linewidth of the magnetic resonance is plotted as a function of cell temperature. It can be seen that above 90 °C, the linewidth begins a sharp increase as a result of spin-exchange broadening. In Figure 21, the signal contrast, defined as the signal divided by the optical absorption, is plotted for several cell temperatures as a function of the laser power at the input of the cell. As expected, the signal saturates at high light intensity as the atomic polarization becomes fully pumped. As the cell temperature increases, however, the cell begins to become optically thick, even when the optical pumping is strong. This causes a reduction in the signal since the light begins to be absorbed strongly by the atoms. This result shows that improvements may be made upon absorption monitoring of the atomic polarization at high alkali densities. It may be better to use polarization rotation of light that is detuned from the optical absorption to monitor the atomic polarization at high alkali densities.

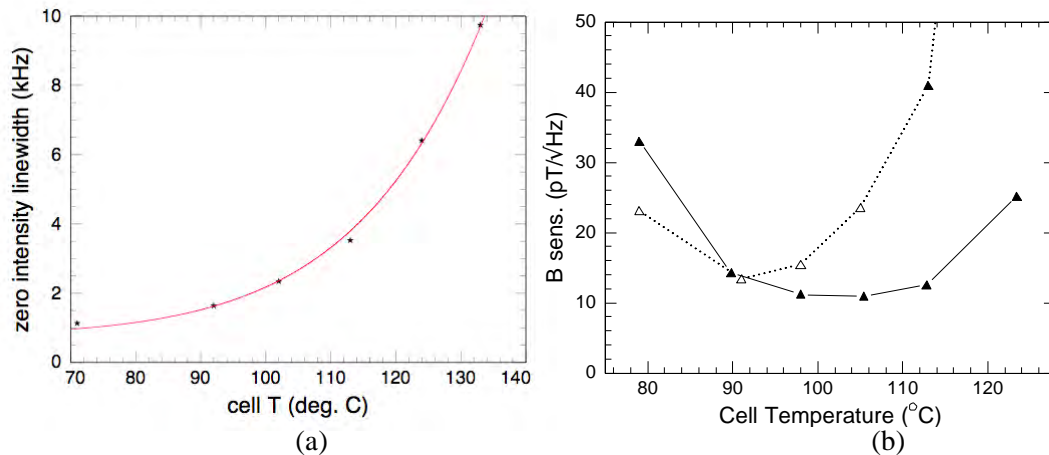


Figure 20 (a) Resonance linewidth, extrapolated to low light power, as a function of cell temperature. (b) Sensitivity, as a function of temperature. The open points are for the Bell-Bloom method, while the solid points are the Mx method.

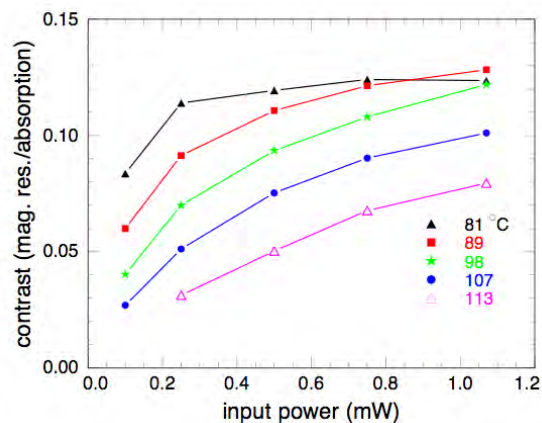


Figure 21 Signal strength, as measured by the contrast, as a function of input optical power for several temperatures.

The difficulty associated with the optical thickness of the cell can be addressed in several ways. One way is to reduce the size of the cell while keeping the density of alkali atoms (cell temperature) constant. Because there are now fewer atoms in the cell, the absorption is reduced. The smaller cell size does not affect the bandwidth of the magnetometer since we are assuming that the alkali density is large enough that spin-exchange collisions dominate the spin relaxation. However, the smaller size of the cell will result in reduced magnetometer sensitivity, which is of course a disadvantage of this scheme.

An improved method is to use a second light field detuned from optical resonance as a probe of the atomic polarization. Because of the detuning, the absorption of the light passing through the

cell is reduced. However, the light still experiences a fairly strong phase shift. While the absorption falls off as the inverse square of the detuning the phase shift falls off only as the inverse of the detuning. If the phase shift is used to monitor the atomic polarization therefore, the effects of the optical absorption can be largely eliminated while maintaining large signal-to-noise ratio simply by detuning the optical field sufficiently. This method was pursued next.

1.2 Demonstration of high performance signal detection

We therefore carried out the experiment shown in Figure 22(b) to verify the phase shift approach and determine the sensitivity scaling as a function of cell temperature. In this experiment, a strong, resonant circularly-polarized pump is applied to the atoms in the cell. In order to polarize the majority of the atoms in a cell which is optically thick, the pump field must have an intensity such that the optical pumping rate is much greater than the intrinsic relaxation rate of the cell. This normally would lead to significant power broadening of the Larmor resonance and associated degradation in the magnetometer sensitivity. However, we pump the atoms by pulsing the pump light field and then allowing the atomic spins to precess through free induction decay. During their free precession, the probe field will monitor their precession phase through polarization rotation to determine the Larmor frequency. After significant relaxation has occurred, the pump will be turned on again to repump the atoms. Since the pump field is not turned on for most of the time the atoms are precession, power broadening of the Larmor resonance is largely avoided. Plots of the described signals are shown in Figure 23.

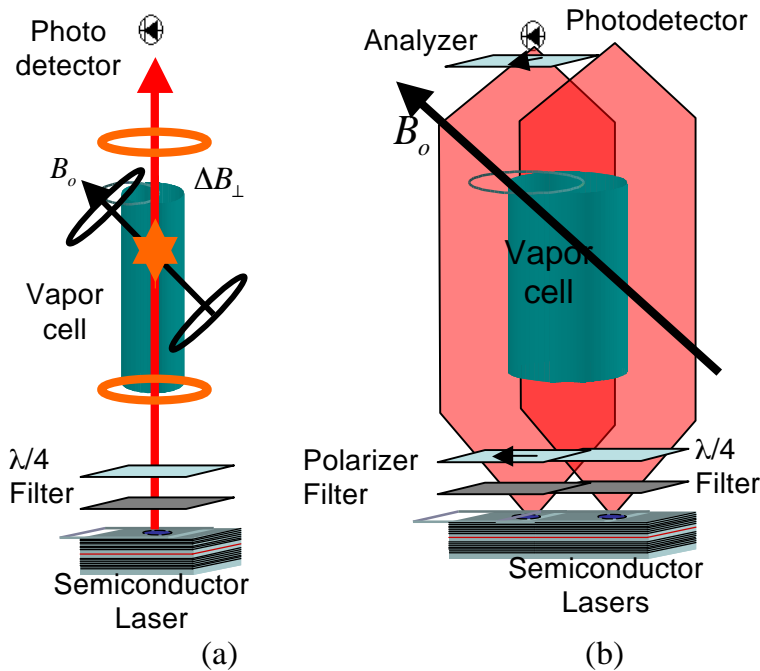


Figure 22 (a) Original Bell-Bloom design with a single, resonant laser. (b) Two-laser design in which one laser, circularly polarized and tuned to the optical resonance, pumps the atoms, and a second, probe laser, linearly polarized and detuned from the optical resonance, interrogates the atoms. The precession of the atomic spins is monitored via the polarization rotation of the probe.

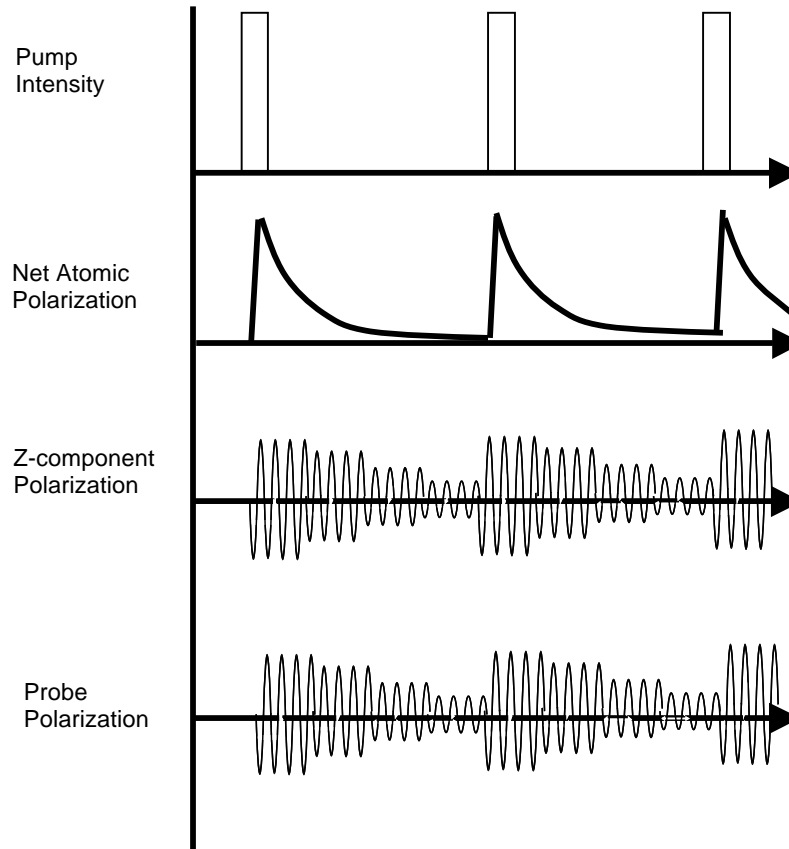


Figure 23 Pump/probe scheme for optically thick cells. The pump field is pulsed to avoid optical power broadening of the Larmor resonance.

The actual apparatus used to carry out the experiment is shown in Figure 24.

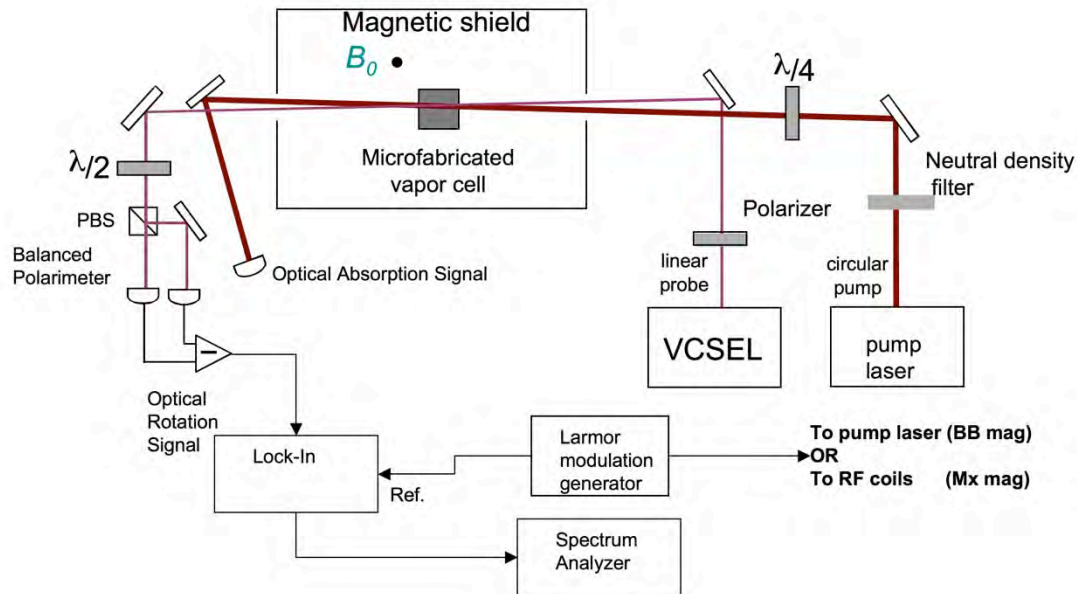


Figure 24 Experimental setup. The cesium atoms are confined in a microfabricated vapor cell of volume 1 mm^3 . Light from the pump laser creates a polarization in the atoms, which is probed by a weak linearly polarized VCSEL. The modulation of the polarization rotation of the probe laser at the Larmor frequency is measured with a balanced polarimeter feeding into a lock-in amplifier.

A circularly polarized laser at a wavelength of 894 nm, resonant with the cesium atoms inside the microfabricated vapor cell (1 mm^3) polarizes the atoms along the direction of the laser beam. A second, weaker, linearly polarized beam passes through the same vapor of atoms at a very small angle. The polarization of the atoms rotates the polarization of this probe beam. This rotation is detected with a balanced polarimeter; it consists of a polarizing beamsplitter and two photodetectors. The half waveplate in front of the polarizer is adjusted such that the polarimeter is balanced, i.e., equal light power is detected on both photodiodes, if no magnetic field is present. The output signal of the polarimeter is proportional to the rotation angle of the probe beam. Due to the precession of the polarized atoms in a magnetic field the polarization rotation becomes modulated at the precession frequency. It is detected with lock-in amplifier referenced to the Larmor frequency of the atoms. Such a signal can be seen in Figure 25, as the magnetic field is varied.

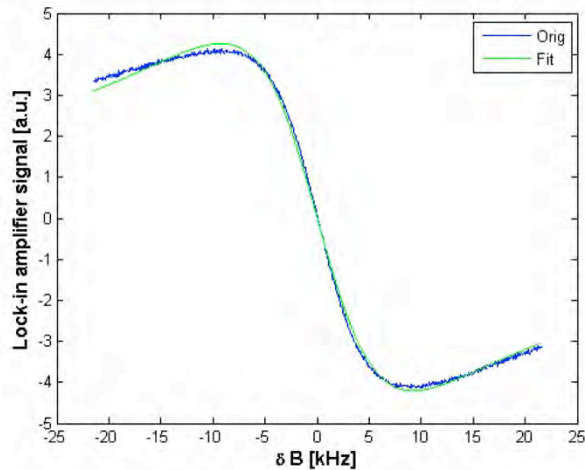


Figure 25 Optical rotation signal of the Bell-Bloom wideband magnetometer as the magnetic test field is scanned. The optical density on resonance was ~ 4 (150 °C). Pump and probe power were 500 μW and 12 μW , respectively. The resonance width was measured as 18.5 kHz.

The system is optimized to give a bandwidth above 10 kHz and a sensitivity below 10 pT/ $\sqrt{\text{Hz}}$. This is shown in Figure 26. The sensitivity and bandwidth are measured for the same experimental parameters. Therefore, we have demonstrated that a high sensitivity, wideband magnetometer is possible by raising the cell temperature and using the signal extraction techniques described above.

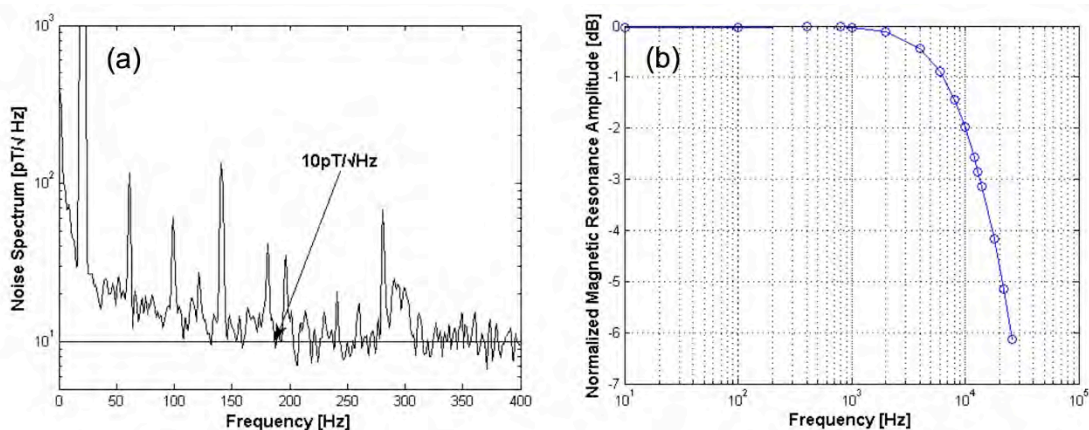


Figure 26 (a) Sensitivity of the wideband magnetometer: 10 pT/ $\sqrt{\text{Hz}}$ between 100 and 400 Hz. (b) Bandwidth of the wideband magnetometer: 15 kHz.

We also investigated the noise characteristics of this type of magnetometer. One of the major noise sources is the frequency noise of the vertical cavity surface emitting laser (VCSEL). VCSELs usually exhibit much larger frequency noise than usual edge-emitting laser diodes. This frequency noise can then be converted into amplitude noise on the detector by the absorptive slope of the atomic vapor. In order to reduce this FM-AM noise conversion, first, a large amount of nitrogen is added to the vapor cell. This broadens the optical absorption resonance and results in a shallower noise conversion slope. Second, the balanced polarimeter cancels the AM noise to first order, since the noise on the two photodetectors is correlated. Our measurements show that there is still another noise conversion process: The frequency noise from the laser gets converted into optical rotation noise. Since this noise is anticorrelated, it will not be canceled by the polarimeter. In order to investigate this type of noise in detail, the noise on the polarimeter was measured as a function of probe laser detuning. By detuning the laser, the noise conversion slope is varied and the shape of the noise profile can reveal information about the source of noise. The polarimeter was balanced for every detuning to separate the effect from FM-AM conversion.

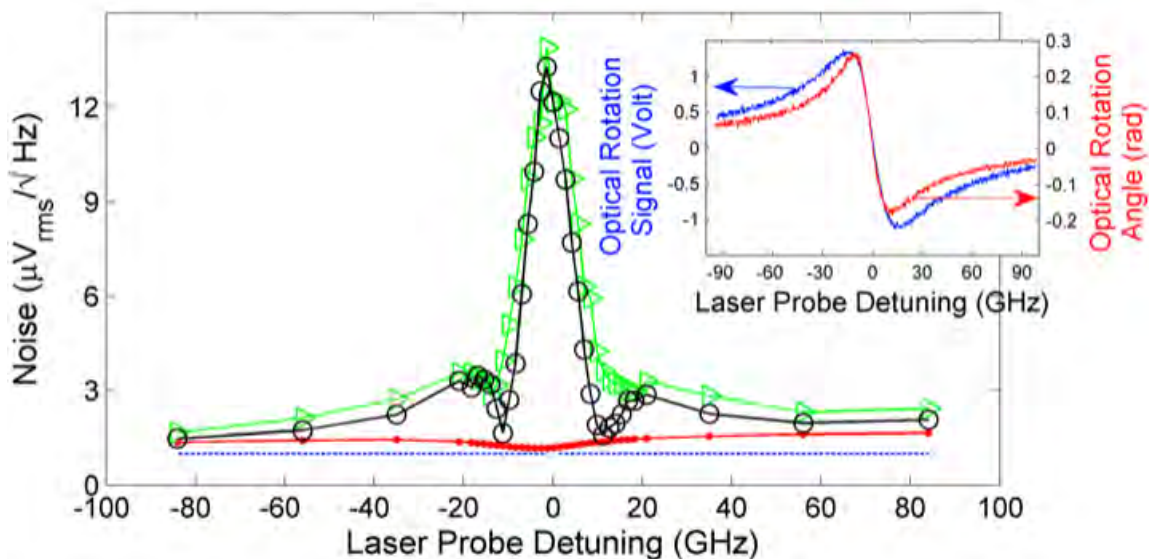


Figure 27 Observed noise as function of probe light frequency detuning for an optical depth value equal to 0.55. Red points: noise in the absence of pump beam. Hollow green triangles: noise when the pump beam is present and the polarimeter is imbalanced. Hollow red circles: noise when the pump beam is present and polarimeter is balanced. Blue dashed line: estimated photon shot noise of transmitted probe on resonance. Solid lines are used to guide the eye. Inset, optical rotation signal (blue trace) and optical rotation angle (red trace).

Figure 27 shows the noise as a function of probe frequency detuning. The green triangles show the noise for an unbalanced polarimeter and the black circles for the balanced case. The inset shows the polarimeter signal and the rotation angle as a function of detuning. We find that our model for FM-to-rotation conversion agrees well with the measured data (for more information see ⁸). Finally, we can see from the black trace in the Figure 27 that the laser detuning can be

chosen such that the noise is minimized at levels near the photon shot noise limit (red line in Figure 27). This was the method used to optimize the magnetometer performance.

Task 2 Construction of MEMs Cells

2.1 Demonstration of angled interiors

Partly supported by this work, NIST, along with M.A. Perez of the MicroSystems Laboratory and the University of California at Irvine, and U. Nguyen of the University of California at Berkeley, demonstrated techniques for making angled walls inside Cs vapor cells.⁹

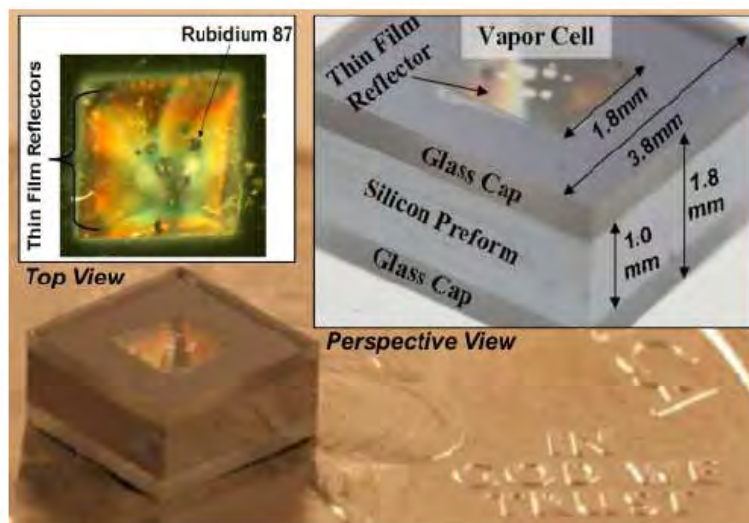


Figure 28 Vapor cell with integrated multilayer thin film reflectors (on a US quarter for scale) .

The Cs cells are made by etching holes in the silicon wafer. Making these walls angled is not really the problem. Actually, making them straight is a bigger problem, since silicon naturally wants to etch along its crystal planes, which are at an angle of 54 degrees to the wafer plane.

More interesting is making reflective edges that reflect a reasonable amount of light. Bare silicon edges will reflect only 33% of the incident light at the wavelengths of interest to us. Since a useful device would likely entail two reflections from such surfaces, a total of 89% of the light would be lost. Such a loss of light power would be highly undesirable.

Multilayer structures of thin films of dielectric material may be used to increase the optical efficiency of the reflector cell. In the Distributed Bragg Reflector (DBR), light reflected at the interface between each layer is designed to constructively interfere to maximize the total reflected optical power at a specific wavelength. The reflectivity is maximized if the structure is composed of alternating layers of two materials of different indices of refractions, and if the optical

thickness of each layer is one-quarter wavelength of the light to be reflected, such that

$t_{layer} = \frac{\lambda}{4n}$. The reflectance of such a structure is given by

$$R = \left(\frac{1 - \left(\frac{n_H}{n_L} \right)^{2p} \left(\frac{n_H^2}{n_S} \right)}{1 + \left(\frac{n_H}{n_L} \right)^{2p} \left(\frac{n_H^2}{n_S} \right)} \right)^2$$

where n_H and n_L are the higher and lower index of refractions of each of the thin film materials, respectively, p is the number of layer pairs, and n_S is the index of refraction of the substrate. It can be seen that reflectivity increases rapidly for increasing optical contrast (n_H / n_L) and for an increasing number of layers.

Several dielectric materials are available for deposition onto silicon structures using conventional thin film techniques. Amorphous silicon provides a high index of refraction of $n_H = 3.9$, while silicon dioxide (SiO₂) has a low index of $n_L = 1.45$ at 795 nm. Use of these materials yields a high optical index contrast ($n_H / n_L = 2:7$). On a silicon substrate, $p = 3$ layer pairs (six total layers) forms a mirror of $R = 0.997$, or better than 99% efficiency after two reflections.

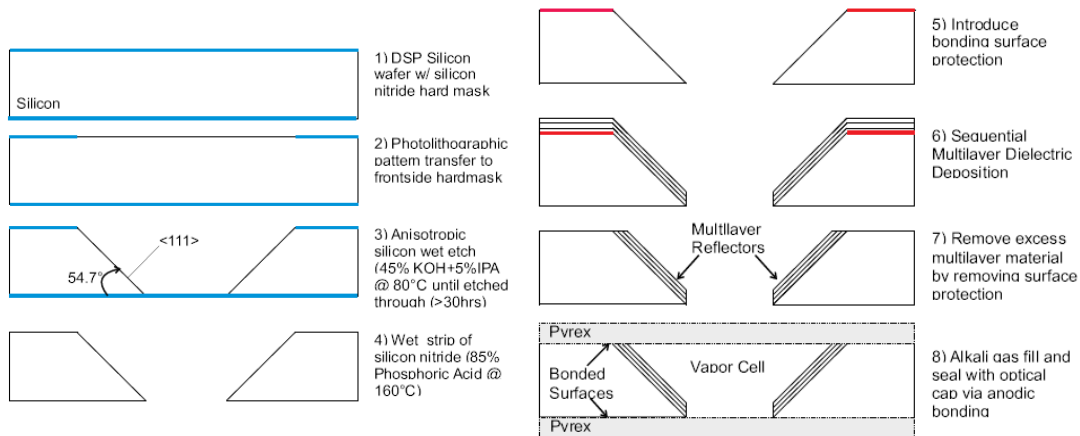


Figure 29 Fabrication of the bulk micro-machined silicon reflector preform with the high reflectance multilayer sidewall reflector, including the final anodic bonding and gas encapsulation process.

The fabrication of the cell is a hybrid of traditional bulk micromachining¹⁰, optical thin film deposition¹¹, and anodic wafer bonding¹². Referring to Figure 29, the first three steps are a traditional silicon wet through-etch. The next four steps are the processing related to the optical films. The final step is the encapsulation of alkali vapor and buffer gasses.

Step 1. We start with a 1 mm thick double side polished undoped silicon wafer. On each side of the wafer, a 3000 angstrom thick silicon nitride layer is deposited via Low Pressure Chemical Vapor Deposition (LPCVD). The silicon nitride is used as a wet etch hardmask.

Step 2. A 1.8 mm sided square is patterned lithographically using a AZ4620 photoresist mask. This mask is aligned to the <100> wafer flat. The cell window pattern is transferred to the silicon nitride hardmask via a short Reactive Ion Etch (RIE).

Step 3. The patterned wafer is immersed in a bath of 45% (by volume with water) potassium hydroxide (KOH) to which is added 5% (by volume) isopropyl alcohol (IPA). The bath is heated to 80 C, causing the exposed silicon to etch at 0.5 μm / min revealing the surfaces of the <111> crystalline planes. This forms a cell with flat, angled sidewalls inclined at 54.7 degrees to the wafer surface. The etch is allowed to progress through the wafer, typically taking more than 30 hours.

Step 4. The silicon nitride hardmask is chemically removed via a hot 160 °C phosphoric acid dip.

Step 5. The top surface of the etched silicon is stamped onto a shallow photoresist film and allowed to dry, which provides protection to the anodic bonding surfaces during subsequent deposition.

Step 6. The optical films are sequentially deposited by plasma enhanced chemical vapor deposition (PECVD) via a PlasmaTherm 790. A cross section of a structure after Step 6 is shown in inset 3 of Figure 29.

Step 7. The final cell preform is fabricated by removing the top surface protection via a fuming sulfuric acid dip, resulting in the lift-off of the excess thin film material and cleaning of the surfaces.

Step 8. The preform is filled with the alkali material. The filling method consists of combining BaN_6 and $^{87}\text{RbCl}$ inside a glass ampoule. The ampoule nozzle is aligned to the cell preform within a vacuum chamber and heated to release ^{87}Rb into the cell preform. Then buffer gases are released into the chamber and the cell is sealed via anodic bonding between two Pyrex 7740 plates. In this case, the vapor cell was filled with ^{87}Rb along with 153 Torr Xe and 1100 Torr N_2 buffer gases. The top Pyrex plate allows optical access to the vapor.

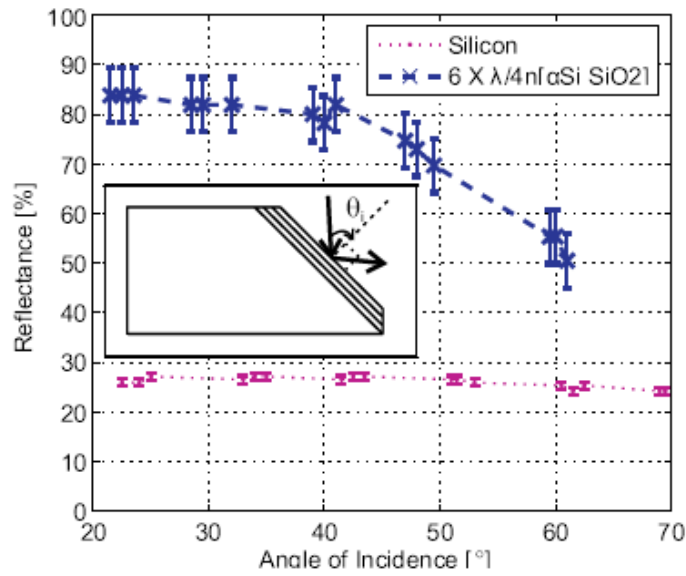


Figure 30 Reflectance from a single bulk micro-machined silicon sidewall reflector with and without multilayer reflectors.

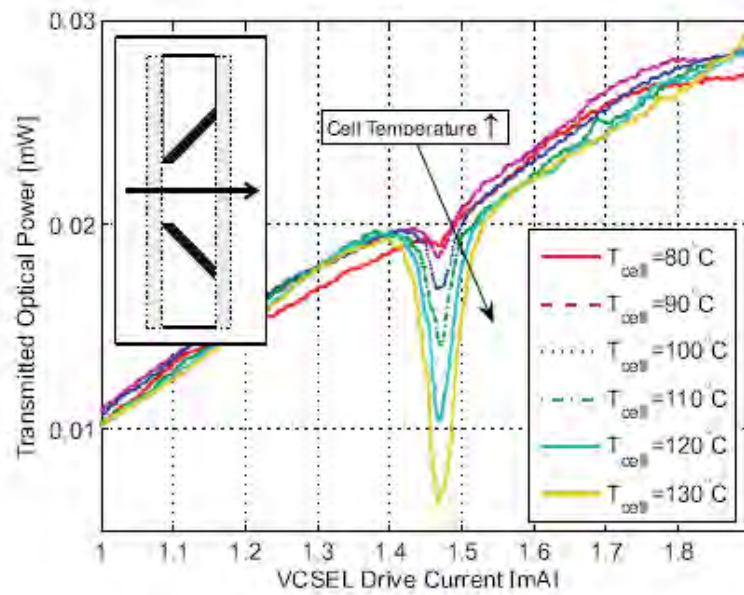


Figure 31 Optical absorption in the vapor cell under elevated temperature (T_{cell}) under swept emission from a VCSEL due to the ^{87}Rb D_1 atomic transition.

Results

To characterize the reflection of an individual etched sidewall, a cell after Step 7 of fabrication was split and mounted on a rotation stage. In the experiment we used a single mode VCSEL (manufactured by ULM) temperature stabilized at 20 °C. The collimated light beam from the VCSEL was directed at the surface. The reflected beam was collected and the power was monitored by a photocollector at different reflection angles of incidence. The power collected is normalized by the VCSEL emission power, as shown in Figure 30. The reflective surfaces of the cell are characterized to have a reflectance over 80% for incident angles up to 40° which is almost three times greater than that of identically etched bare silicon sidewall reflector, which exhibits a reflectance under 30%.

To characterize the optical absorption by the encapsulated vapor, the light from the VCSEL was passed directly through the complete vapor cell, shown in Figure 28. A small resistive heater was used to elevate the cell temperature, increasing the vapor pressure of the ⁸⁷Rb within the enclosed cell. The emission wavelength of the VCSEL was swept by varying the drive current at constant VCSEL temperature from approximately 794.5 nm at 1.0 mA to 795.1 nm at 2.0 mA. At increased vapor pressure under elevated temperatures, wavelength swept VCSEL light transmitted through the cell showed significant absorption at the D₁ atomic transition of ⁸⁷Rb (794.8 nm in air), demonstrating alkali vapor encapsulation (Figure 31).

The VCSEL beam was then directed onto one sidewall of the cell. The beam was reflected through the cell and redirected back towards the plane of emission by the reflector on the opposite sidewall, where the optical power is collected and monitored. The temperature of the cell was held fixed at a temperature of 100 °C using feedback control and the VCSEL drive current is tuned until a pronounced absorption peak is detected indicating vapor cell interrogation under retroreflected light (Figure 32). When normalized by the optical power of the source, under this retro-reflective path, an optical efficiency of 40% for the reflector cell was demonstrated. This is four times better than the 10% retro-reflection efficiency from a similarly etched silicon cell preform.

However, not included in the efficiency of the bare silicon preform are losses due to the cap window and scattering from the condensed rubidium, which are losses additional to reflector inefficiencies. An optical efficiency approaching 80% was observed in a preform incorporating thin film reflectors fabricated side-by-side with the complete vapor cell. Comparison between this preform and the vapor cell indicates that the multilayer reflectors improve the optical efficiency by a factor of eight for an optical path with two reflections.

We conclude that such techniques, while not simple, could be used in order to obtain desirable performance features using perpendicular light beams. However, for many purposes, simpler geometries will provide adequate performance without this complexity.

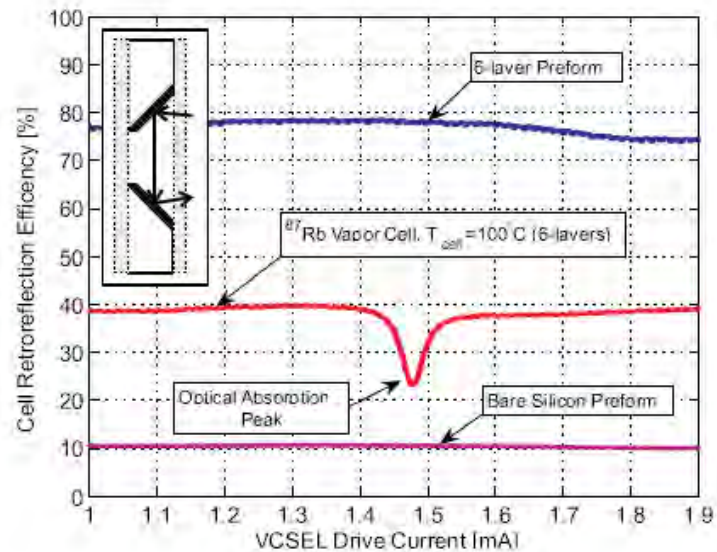


Figure 32 Optical efficiency of the vapor cell and cell preforms during return reflection with and without integrated reflectors.

2.2 Prototyping MEMs physics package

The purpose of the physics package is to implement the operating configuration using millimeter-scale components. The physics package (see Figure 33 and Figure 34) is comprised of two main subassemblies; one containing the lasers and collimating-polarization optics, while the other one contains the vapor cell, heating elements, and a polarization analyzer.

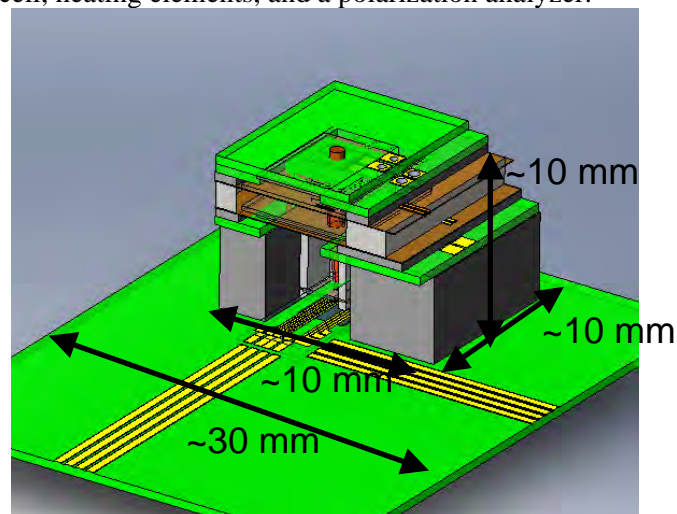


Figure 33 CAD model of physics package.

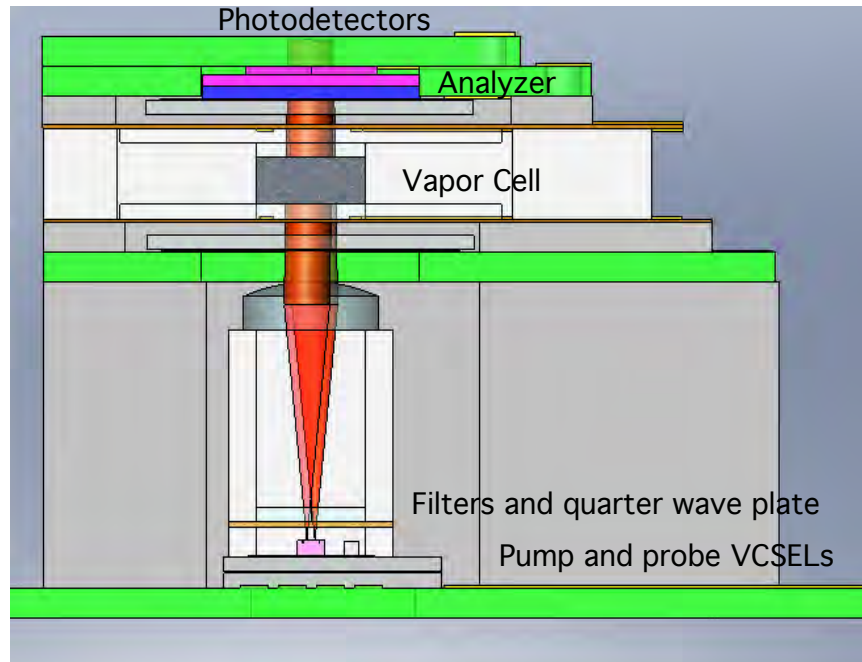


Figure 34 Side view of physics package.

Laser Source and Optics Subassembly.

A chip with two independent vertical-cavity surface-emitting lasers (VCSELs) provides the light for pumping and probing of the ^{133}Cs atoms respectively. The chip is mounted onto a pyrex baseplate as shown in Figure 35. The baseplate is mounted on a printed circuit board with patterned gold traces to bring electrical signals to and from the device. The baseplate routes the VCSEL's driving current through gold-leads. A chip-resistor, mounted near the VCSEL chip, provides the heating power necessary to bring the VCSEL's light frequency near resonance with the ^{133}Cs D_1 optical transition. In order to sense its temperature, a chip-thermistor is mounted near to the VCSEL-chip. The fine tuning of the light optical frequency is achieved by the driving current of the VCSEL. The subassembly is completed with a stack of optical elements that prepare the polarization state of the laser beams and collimates them (see Figure 36).

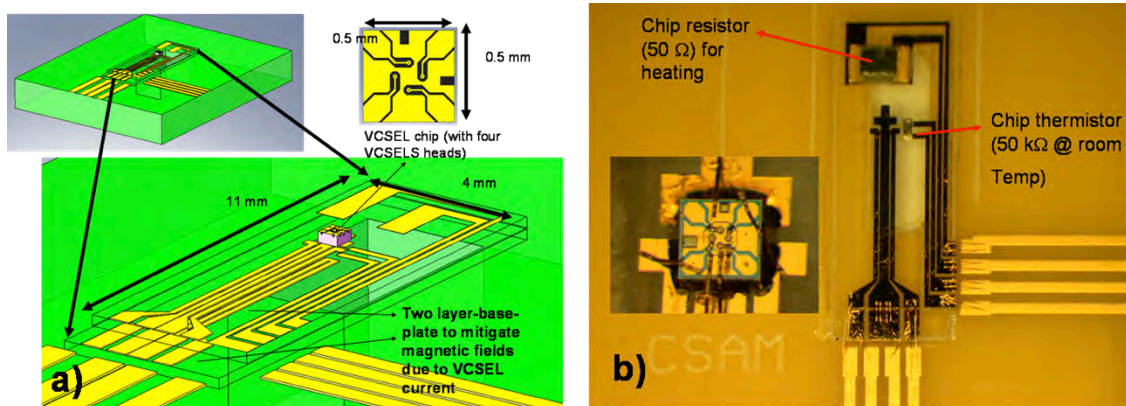


Figure 35 a) CAD model for baseplate with VCSEL chip. b) Baseplate with chip resistor and chip thermistor attached to it, the baseplate is glued to a printed circuit board. The inset in b) shows the VCSEL chip wire bonded to the gold traces in the baseplate.

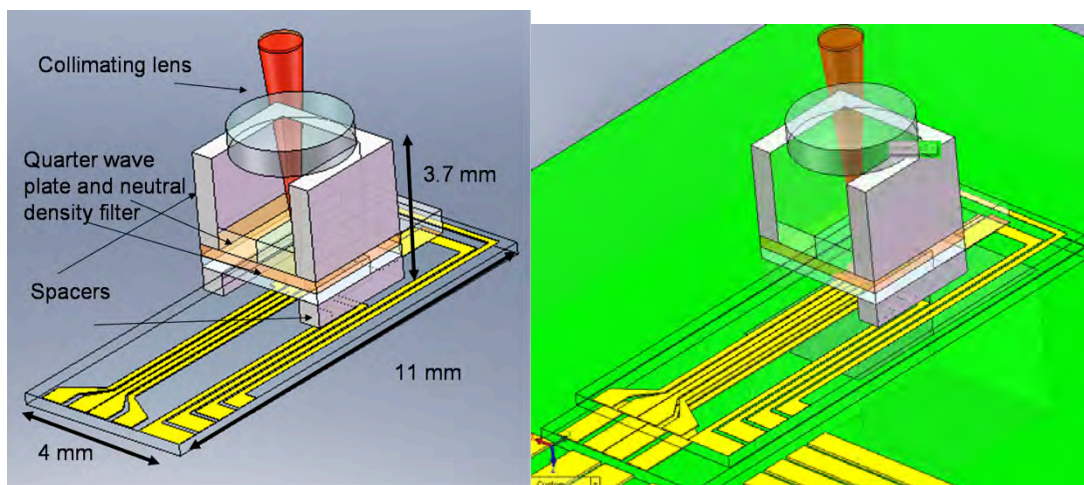


Figure 36 Laser source and optics subassembly.

Vapor cell, heating elements and polarization analyzer subassembly

The second subassembly, shown in Figure 37 and Figure 38, consists of a tower containing the microfabricated vapor cell, vapor cell's heaters, RF coils, a polarization analyzer, and spacers.

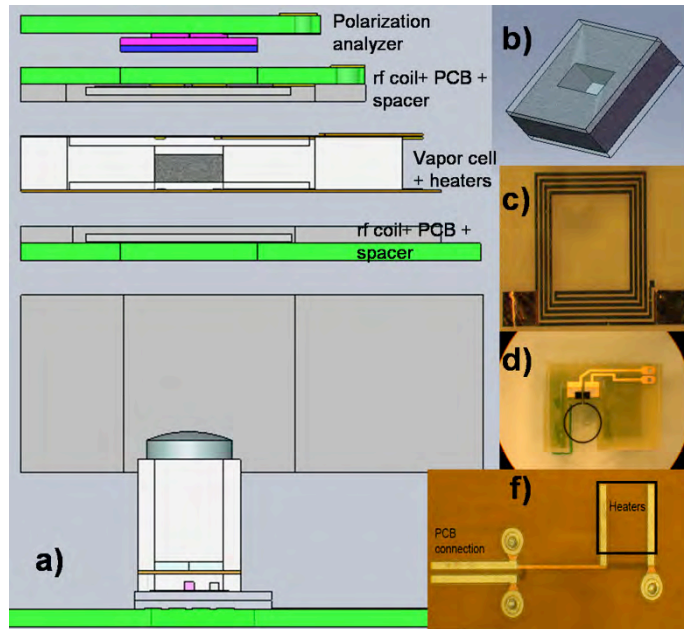


Figure 37 a) Exploded view of second subassembly. b) Microfabricated Cs vapor cell. c) Heaters. d) Top view of RF coils mounted on printed circuit board. f) Kapton sheets.

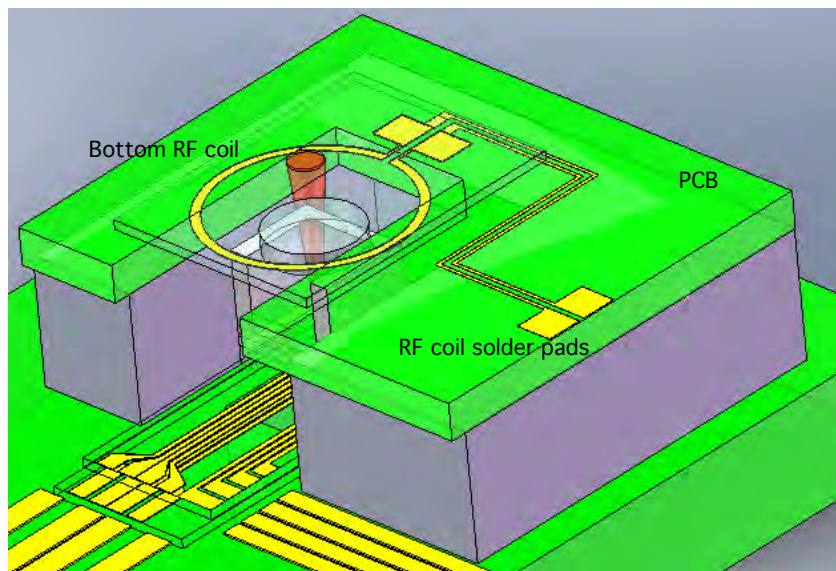


Figure 38 3D view of vapor cell assembly.

The microfabricated cell is filled with ^{133}Cs atoms and ~ 1000 Torr of N_2 buffer gas. The overall vapor cell microfabrication process has been discussed in section 1.1 of this report. The vapor cell is sandwiched between two resistive heaters, which were purposely designed to mitigate the magnetic field produced by the current flowing through them. A more detailed description of the heaters is presented in the section below. Kapton sheets with low thermal conductivity act as a support frame for the stack of vapor cell and heaters. In addition, the kapton sheets have electrical conductive pads to bring the current to the heaters from the electronics control system. A single turn coil is placed on both sides of the stack of vapor cell and heaters. The two coils were placed for flexibility, in order to test the Mx mode of operation. The coils are formed by patterning gold on a glass wafer. The upper part of the tower is comprised by a polarization analyzer (one half-wave plate, two crossed polarizers and two photo-detectors). Finally, spacers made out of Ultem plastic are placed where needed.

Design, fabrication and test of heaters

The resistive heaters were designed to mitigate the magnetic field produced by the current flowing through them. To achieve this, titanium traces were patterned onto a Pyrex substrate ($200\ \mu\text{m}$ thick), then a thin-film transparent insulator layer ($1\ \mu\text{m}$ thick) was deposited on top of the titanium traces, so that a second pattern of traces (mirror of the first one) could be placed on top of the first one. In this way, the magnetic field produced by the current flowing through the first titanium layer is highly mitigated by the one produced by the current flowing through the second titanium layer.

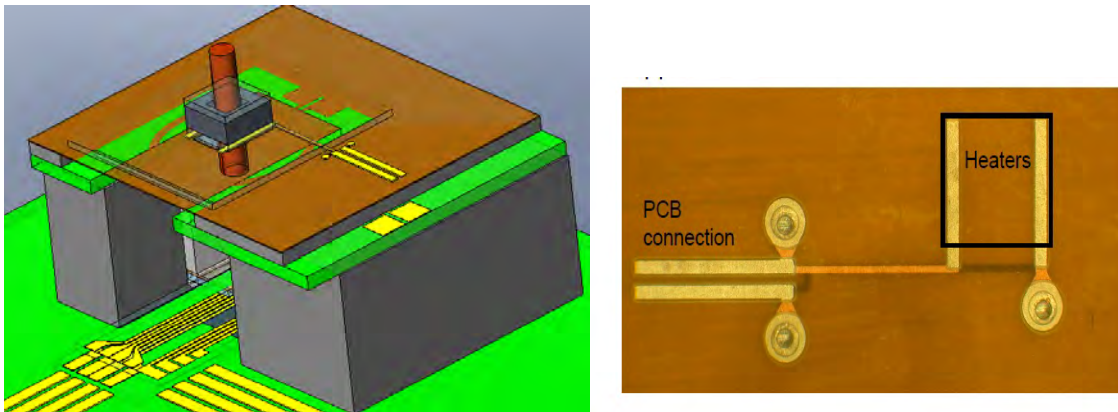


Figure 39 Heater configuration on prototype physics package.

The heaters were tested to determine their reliability and performance limits. Specifically, we wanted to determine the heater's temperature breakdown, current breakdown and heating power breakdown. Overall, the fabricated heaters achieved a 50% yield. From our tests we determined that the heaters can withstand temperatures as high as $170\ ^\circ\text{C}$. Above this temperature the heater starts turning yellowish and then burns. The heaters can support up to 550mW of heating power before they start turning yellowish, which is plenty of heating power to achieve the operating

temperature of our device. The resistance of the heaters ranges between 500Ω to $2 \text{ k} \Omega$, and is a function of the heater's temperature. Finally, the tests indicate that the heaters can support AC heating, which can mitigate the effects of the magnetic field produced by the heater's current on the atoms.

Low magnetic field heaters

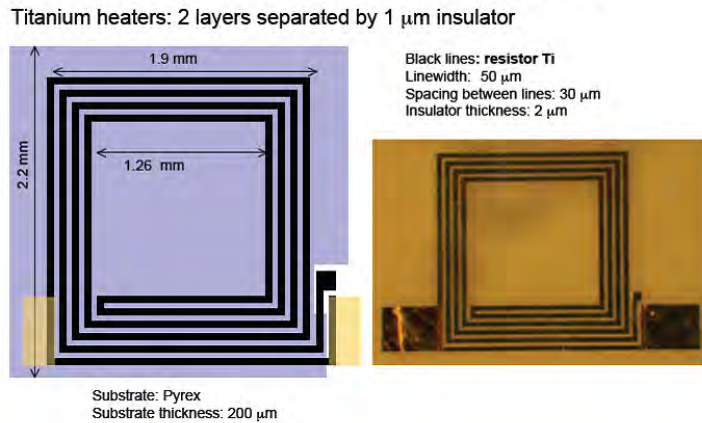


Figure 40 Low magnetic field heaters.

Assembly of physics package

We assembled a total of four physics package prototypes. The first three prototypes failed in the early assembling stages because the laser light sources (VCSELs) died while being characterized in the laboratory. The cause was a problem with the VCSEL's driving electronics. This problem was addressed by adding a protection circuit to keep from overdriving the VCSEL under certain conditions.

For our final prototype, we had run out of VCSELs that were originally designed in. A second batch of VCSELs was obtained from a different supplier. The dimensions and properties of these new VCSELs are slightly different from the original ones. The original prototype was to have used two VCSELs, while with the new geometry, only a single device can be used. Since the objective of this project was to research methods in interrogating sensors as well as investigating methods for assembling physics packages, we decided to analyze a single-beam interrogation approach.

In this revised version of the original design, the pump and probe action of the laser light is performed by a single beam instead of two independent beams. This change will yield a decrease in the intrinsic signal (optical rotation) of the device that can be overcome by either using amplifying-signal techniques or operating at higher atomic densities. A picture of the final assembled physics packaged is shown in Figure 41a, while Figure 41b shows a 3D model of the original design.

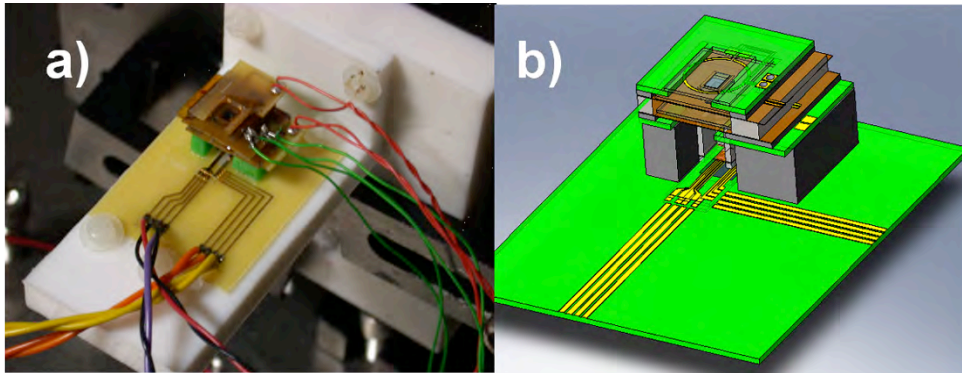


Figure 41 a) Assembled physics package. b) CAD model of physics package.

Changing from a two-laser approach to a single laser approach

In this section, we analyze the differences between a single-beam and a dual-beam interrogation method. The dual-beam method is shown in Figure 42, while the single-beam method is shown in Figure 43.

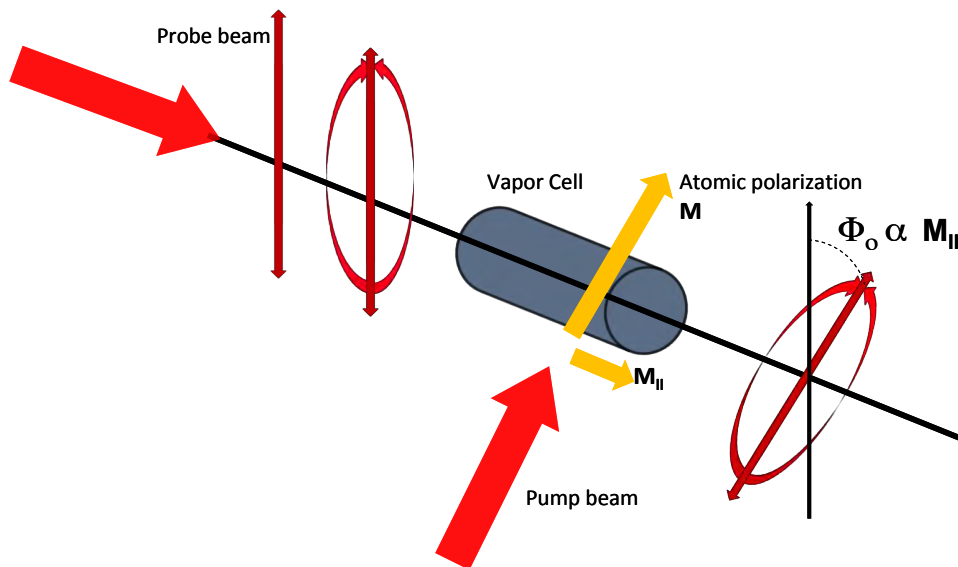


Figure 42 Dual-beam interrogation method.

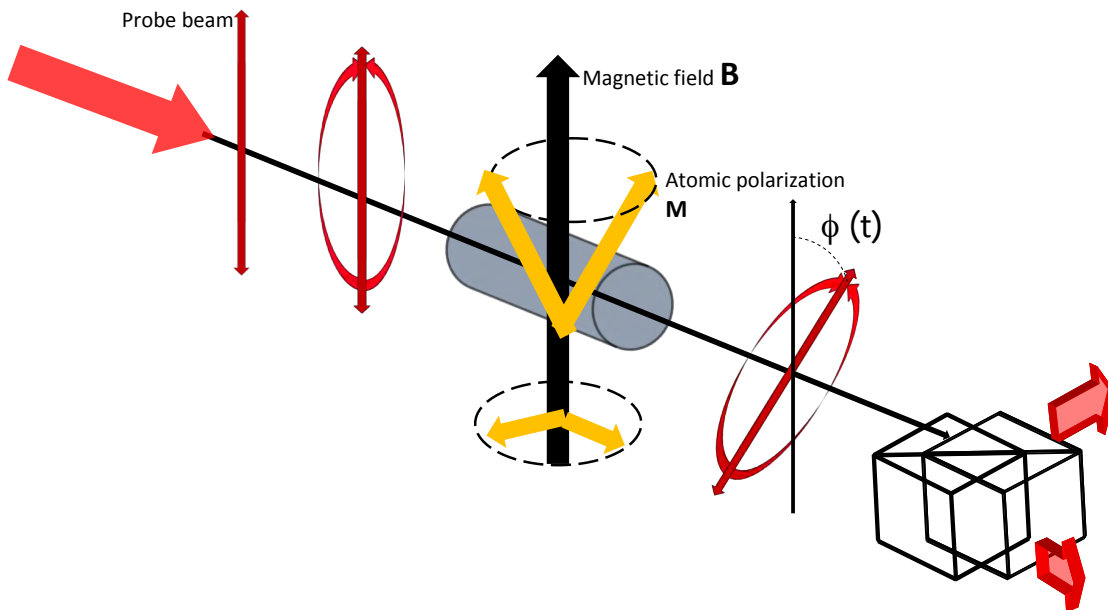


Figure 43 Interrogation method using a single elliptically polarized beam.

From the experiments performed on the laboratory optical bench, the dual beam method allows for higher performance. However, in order to build a prototype using miniature components, we decided to design a version using a single laser beam. This was due to a practical necessity as described below, as well as a desire to explore this possibly simpler implementation.

The first generation of the physics package was designed relying on the dimensions and characteristics of the original VCSELs. In particular, the spacing between the two VCSELs heads in the chip and their beam divergence angle. These two features drive some of the dimensions in the physics package, one of them the maximum distance between the polarization optics and the VCSEL chip. If the pump and probe laser beams overlap as they propagate through the polarization optics, then some portion of the transverse profile (or the whole profile) of the probe beam will become circularly polarized yielding a reduction in the optical rotation of the probe.

As mentioned above we changed VCSELs. The spacing between the two VCSELs heads in the new chip is smaller (by a factor of four) than the spacing between the heads in the original chip. Likewise the beam divergence angle of the new VCSELs is larger (by a factor of three). Because of these changes both beams overlap as they propagate through the polarization optics and a linearly polarized probe laser beam cannot be generated.

The spacing between the two VCSELs heads in the chip and their beam divergence angle also drive the minimum distance between the vapor cell and the VCSEL-chip that allows both beams to overlap at the vapor cell. In addition, the laser beam diameter is determined by the divergence

angle of the light beam, which in turn determines the minimum size of the window in the vapor cell.

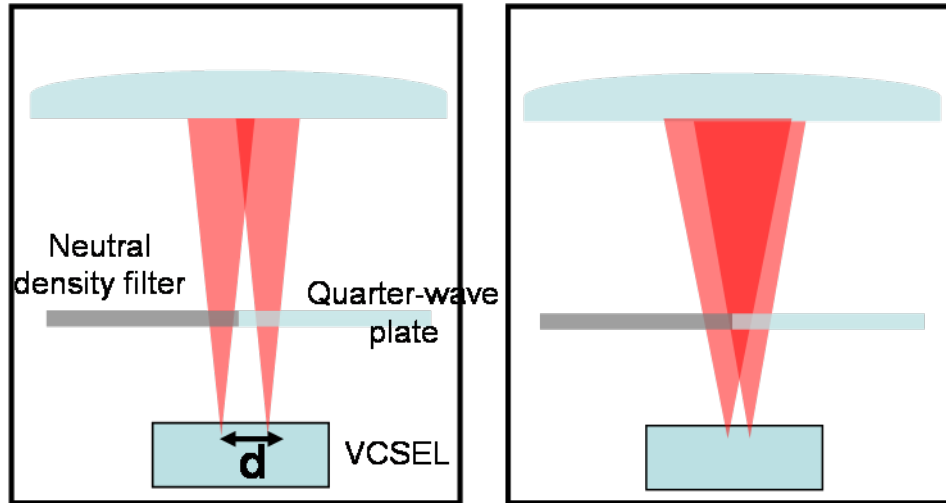


Figure 44 a) Original VCSELs. b) New VCSELs.

An alternative would have been to mount two chips instead of one and use the two VCSEL heads which were farther apart. In this case we would have had to change other parts in the physics package. Therefore, we opted not to follow this route for the following reasons. First, there was indication that we could operate a wide band atomic magnetometer using one single beam and the existing physics package. The device sensitivity could degrade but not its bandwidth. Second, we struggled to obtain laser sources at the D_1 transition of Cs atoms. Using two chips instead of one would empty our stock of laser sources. In case something failed we would have no backup devices.

Parameter	Original VCSELs	New VCSELs
Spacing between VCSELs heads	150 μm	40 μm
Beam divergence at half angle	5 $^\circ$	15 $^\circ$
Operating temperature	~ 55 $^\circ\text{C}$	~ 75 $^\circ\text{C}$
Operating injection current	~ 2 mA	~ 2 mA
Optical power	~ 600 μW	~ 100 μW

Table 1. VCSEL parameters

Operation of wide band atomic magnetometer with an elliptically polarized pump-probe laser beam.

The operating configuration of a single beam wide band magnetometer is similar to the one for the dual-laser design. The wide bandwidth (10 kHz) is achieved by operating the vapor cell at high temperatures (above 130 °C), such that the relaxation time of the alkali atoms yields roughly the desired bandwidth. Probing is still performed by phase-shift detection. However in the single beam approach one single, off-resonant, elliptically polarized laser beam is used for both pumping and probing. This scheme has been carried successfully before¹³ for a magnetometer operating in the SERF regime.

Table 2. Dual-laser approach and single-laser approach comparison.

Approach	Two laser beam	One laser beam
Pumping	A dedicated circularly polarized laser beam tuned on resonance optically pumps the atomic sample.	Pumping is achieved by the unbalance between the two circular components in the laser light. Laser light is tuned off-resonance. Pumping efficiency is decreased by a factor $\sqrt{2}$ with respect on-resonance pumping.
Probing	A dedicated linearly polarized laser beam is tuned off resonance. The phase shift between its circular components is detected using a polarization analyzer.	The phase shift between the two circular components of the laser light is detected using a polarization analyzer. Detection efficiency is decreased by a factor $\sqrt{2}$.
Bandwidth	The bandwidth is achieved by operating the device at high temperatures, such that the relaxation time of the alkali atoms yields roughly the desired bandwidth.	The mechanism is the same as the one for the dual-laser approach. No change in bandwidth due to operation with a single laser beam.
Noise due to beam steering.	Noise at low frequencies is degraded due to the relative motion between the probe and pump beams at the vapor cell.	No noise due to beam steering, because there is only one single beam. Noise at low frequencies is expected to be lower.
Ease of electronic control.	The injection current for each laser needs to be controlled independently from each other.	Only one laser to be electronically controlled. It is expected, this yields a simpler control system.
Device measurement bias due to light-shifts.	No light-shifts when the pump laser is tuned on resonance with the optical transition.	Some light shift (less than 1 nT) since the light is tuned off-resonant and there is some degree of circular polarization.

After fixing the problem causing the failure of the previous prototypes we started assembling the fourth physics package. We assembled ~80% of the physics package and performed some device characterizations before it failed. The failure of the fourth prototype was different from the previous ones. In this prototype, it was the heating element that failed instead of the laser source. The failure happened as we were finishing the assembly process (e.g. attaching the miniature polarization analyzer to the physics package). We did not have enough components to start assembling a fifth physics package. However, we were able to characterize the performance of the magnetometer before the integration of its polarization analyzer. These results are shown below.

Device Characterization.

The magnetic field to be measured is provided by Helmholtz coils and a solenoid. The net magnetic field produced in this configuration is oriented at 45 degrees with respect to the optical beam propagation axis. The RF coils in the physics package are used to coherently drive the precession of the atomic spin about the static magnetic field at the Larmor frequency. The ^{133}Cs atomic spin precession modulates the light intensity and optical rotation of the transmitted light. The optical rotation is measured using an external balanced polarimeter. Our current design incorporates a miniature balanced polarimeter to be placed at the top of the physics package. However, for the measurements reported here the transmitted beam was analyzed using a balanced polarimeter external to the physics-package (see Figure 45a).

The signal from the balanced polarimeter was sent to a Lock-in amplifier (Figure 45c) so that the magnetic resonance line could be recorded. For the measurement of the frequency response and noise, the signal from the balanced polarimeter was sent to a spectrum analyzer (see Figure 45d). The magnetic resonance signals are generated by slowly ramping the static magnetic field near the resonance and recording the dispersive signal obtained from one of the Lock-in outputs upon proper adjustment of its phase. Typical magnetic resonance signals are shown in Figure 46.

The SNR was determined using the amplitude of the magnetic resonance signal acquired by the Lock-in, and by measuring the noise of the Lock-in output channel with the spectrum analyzer while the magnetic field was on resonance. However, for most of the measurements the SNR was determined by directly sending the signal from the balanced polarimeter to a spectrum analyzer while tuning the magnetic field on resonance (Figure 47). Both methods yield similar values for the SNR.

Sensitivity measurements were carried out at different vapor cell temperatures. By increasing the temperature the spin-exchange relaxation rate increases as well, which in turn broadens the magnetic resonance signal. The sensitivity versus measured magnetic resonance linewidth is shown in Figure 48.

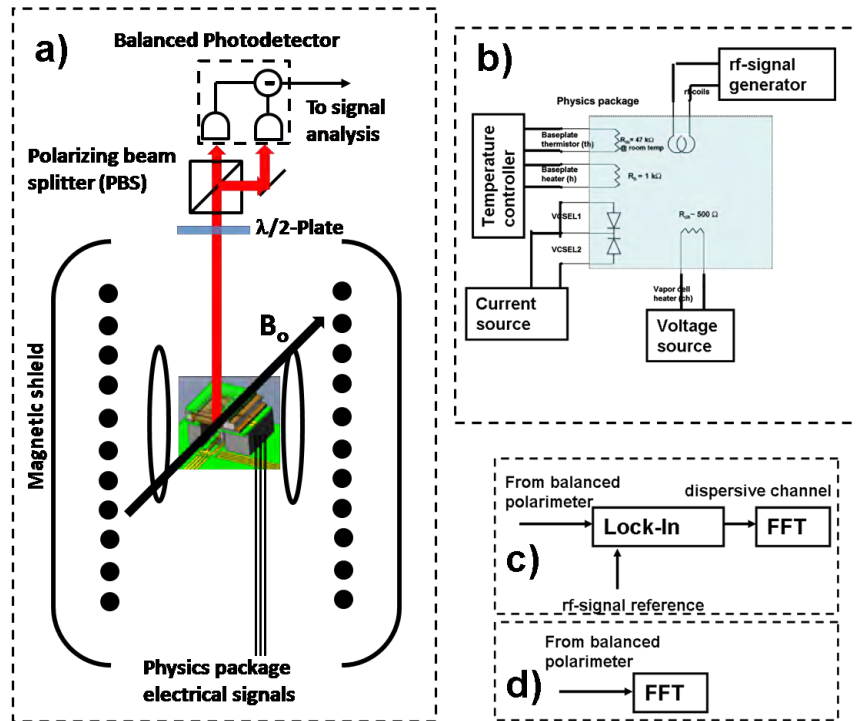


Figure 45 a) Setup. b) Physics package electronics diagram. c) Magnetic resonance signal analysis setup. d) SNR measurement setup.

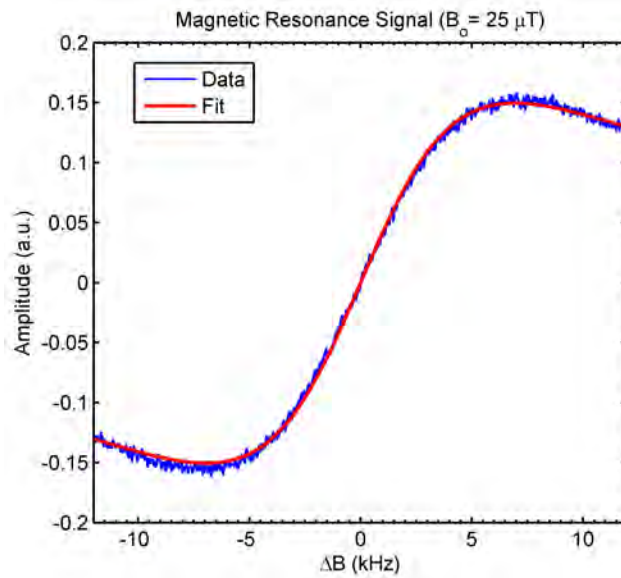


Figure 46 Lock-in dispersive signal as a function of magnetic field detuning..

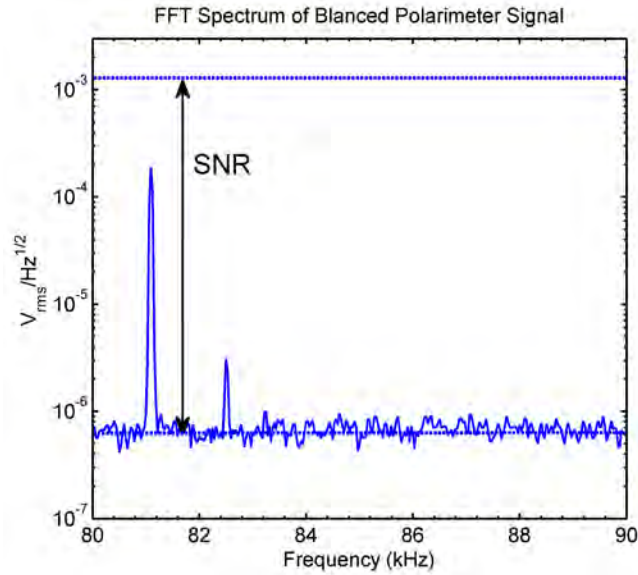


Figure 47 Signal to noise ratio (SNR). The reference for SNR is the signal voltage (the sin wave at 81 kHz) appropriately scaled by the length of the FFT

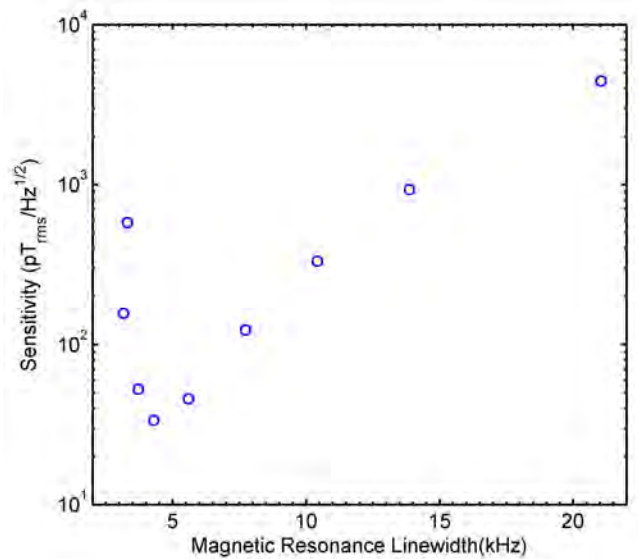


Figure 48 Magnetometer sensitivity as a function of magnetic resonance linewidth.

At low temperatures, the sensitivity is limited by the low levels in the atomic density. At higher temperatures, the sensitivity is limited by the light intensity at the vapor cell. The best sensitivity measured in the device was $33 \text{ pT}_{rms}/\sqrt{\text{Hz}}$ at a magnetic resonance linewidth of 4.3 kHz. A sensitivity of $927 \text{ pT}_{rms}/\sqrt{\text{Hz}}$ was measured at a magnetic resonance linewidth of 13.6 kHz.

Further improvement on the sensitivity was achieved by injecting more light into the vapor cell, i.e. a sensitivity of $600 \text{ pT}_{\text{rms}}/\sqrt{\text{Hz}}$ at a linewidth of 13.6 kHz and a 3dB cut-of frequency of 9.6 kHz.

For the bandwidth measurements, the signal from the balanced polarimeter was sent to the FFT spectrum analyzer. The magnetic field was tuned on resonance, and a small sinusoidal modulation, with a modulation frequency within the 0.1-10 kHz range, was superimposed. The amplitude of the first sideband at different modulation frequencies was measured using the FFT spectrum analyzer.

Figure 49 shows the frequency response of the magnetometer. The measured 3dB cut-of frequency corresponds to 9.6 kHz, while the measured linewidth of the magnetic resonance signal was 13 kHz. The measured sensitivity was $0.6 \text{ nT}_{\text{rms}}/\sqrt{\text{Hz}}$ in an ambient field of $23.2 \text{ } \mu\text{T}$.

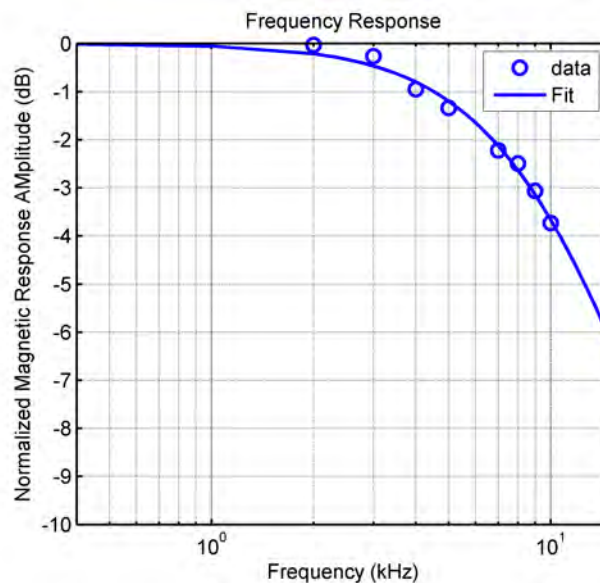


Figure 49 Magnetometer frequency response.

Analysis of Results.

The magnetic sensitivity of the current device is limited by its signal-to-noise ratio (SNR). In order to reach a magnetic sensitivity below $10 \text{ pT}_{\text{rms}}/\sqrt{\text{Hz}}$ at a bandwidth of 10 kHz, a SNR on the order of $10^5/\sqrt{\text{Hz}}$ is necessary. However, in this regime the SNR achieved in the device is on the order of $10^3/\sqrt{\text{Hz}}$. The noise in the measured signal is limited by photon-shot noise. Because of this, the SNR of the device is limited by the light levels available at the vapor cell. Higher levels in the light intensity would yield higher values of SNR.

Currently the light level at the vapor cell is limited by the light beam diameter (2 mm at the $1/e^2$ power level). The window aperture of the vapor cell is 1 mm^2 , whereas the beam transverse area is $\sim 3.14 \text{ mm}^2$, thus the beam is clipped by the cell's window. Furthermore, some of the light is lost by reflection at the different glass slides between the VCSEL and the vapor cell (e.g. quarter wave plate, RF coil, and vapor cell glass window). All these losses result in a coupling of about 16% of the light power into the vapor cell, yielding light power levels of about $10 \text{ }\mu\text{W}$ at the vapor cell.

In order to understand the effects of the pumping light on the sensitivity of the device it is useful to look at the SNR. In the limit of small optical rotation angles, and assuming a photon-shot noise limited signal, the SNR of the magnetometer can be approximated by the equation below

$$SNR = \frac{1}{\sqrt{2}} \sqrt{\frac{tP_o \exp\left[-OD \frac{1}{1+x^2}\right]}{h\nu_o}} OD \varepsilon P_z \frac{x}{1+x^2} \sin(2\theta)^2 \quad (6)$$

where t is the measurement integration time, P_o corresponds to the optical power at the vapor cell in the absence of atoms, h is Planck's constant, ν_o is the optical frequency for the ^{133}Cs D_1 transition, OD is the optical depth on resonance, x is the detuning of the light normalized to the linewidth of the optical transition, P_z is the degree of spin polarization (Eq.(7)), ε is the contrast of the signal, and θ is the orientation of the QWP fast axis with respect to the incoming linear polarization. Typical values of these parameters in the current device are shown below:

Parameter	Value
P_o	$\sim 10 \text{ }\mu\text{W}$
OD	$\sim 2-3$
x	~ 1
P_z	$0.01 \text{ @ } R_{\text{rel}} = 10^4 \text{ s}^{-1}$
ε	$0.01 - 0.8$
θ	22.5 degrees

The strength of the SNR in Eq.(6) is dominated by the level of spin polarization achieved by the pumping light. The degree of spin polarization can be approximated by :

$$P_z = \frac{R_{op}}{R_{op} + R_{rel}} \quad (7)$$

where R_{op} represents the optical pumping rate, and R_{rel} is the relaxation rate. The relaxation rate is roughly equal to the bandwidth of the magnetometer. Given a constant optical pumping rate, a higher bandwidth is achieved at the expense of lower spin polarization levels and SNR, which in turn degrades the sensitivity of the magnetometer.

Figure 50 shows the SNR of the magnetometer as a function of optical power at the vapor cell. The hollow circles show measurements carried out in the physics package. The solid line represents the estimated SNR given by Eq.(6) and assuming a light beam's transverse area of 1mm^2 , a contrast $\varepsilon = 0.045$, and a normalized light detuning $x = 1$. The relaxation rate (R_{rel}) is assumed to be equal to the measured magnetic resonance linewidth (e.g. 13 kHz). We observe that more than $100\ \mu\text{W}$ of optical power are needed to achieve SNR levels on the order of $10^5/\sqrt{\text{Hz}}$. This represents a limitation of the current design; the current available VCSELs can output no more than $100\ \mu\text{W}$ of optical power. Finally, the sensitivity of the magnetometer can be obtained directly from the SNR and linewidth, the sensitivity as a function of optical power is shown in Figure 51.

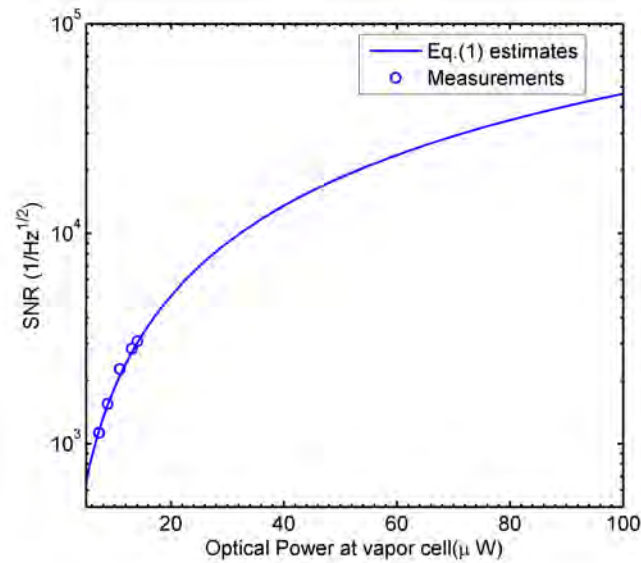


Figure 50 Signal to noise ratio (SNR) as a function of optical power.

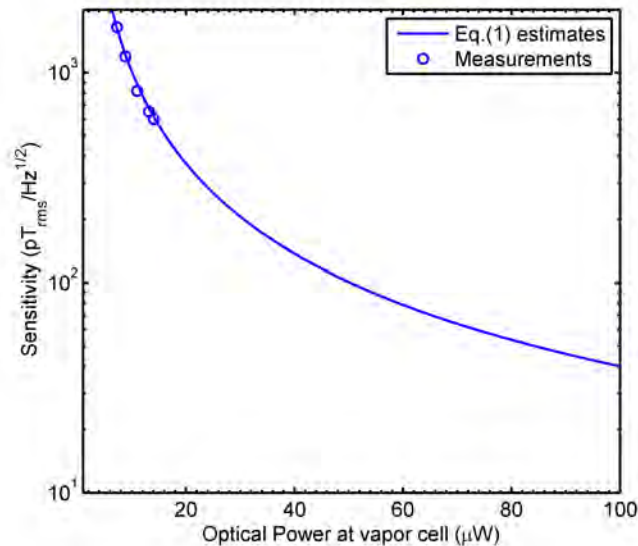


Figure 51 Magnetometer sensitivity as a function of optical power.

The sensitivity of the current device can be improved by injecting more pumping light into the vapor cell. One way to do this is by changing the collimating optics of the device so that the optical beam's transverse size is smaller than the vapor cell window. Another way is to place the vapor cell inside an optical cavity, reflecting the probe beam through the cell several times to increase the effective interaction.

Task 3. Implementation of SERF Technique

3.1 Preliminary investigation of SERF in MEMS cells

In this section, we describe our work investigating the spin-exchange relaxation free (SERF) regime in miniature magnetometers. This shows promise for very high sensitivities, just as in large cells. However, the drawback is that it works only at low fields. For magnetometry in the Earth's field, either we need to raise the temperature even further, or use feedback coils to reduce the field to a level less than about 200 nT. Both are possible and will be investigated in the future. In any case, showing the extremely high sensitivities achievable in such small cells was a major event. This work received a "Top 10" award from MIT's Technology Review.

The SERF regime has shown promise to rival even SQUIDs in sensitivity. In the SERF regime, the Larmor precession frequency is much lower than the spin exchange collision rate. In this case, individual atoms do not lose their polarization during a collision. Therefore, the collision has no ill-effects in terms of reducing the sensitivity, and very high sensitivities are possible.

From the resonance characteristics and noise level, a magnetic field equivalent noise spectrum was determined and is shown by the red trace in Figure 52b. Throughout much of the spectrum, between 10 Hz and 200 Hz, the noise is found to be below $70 \text{ fT}/\sqrt{\text{Hz}}$. This SERF measurement represents an improvement by a factor of almost 100 over previous results in microfabricated vapor cells. Excess amplitude noise from the laser is thought to be the main factor limiting sensitivity in the single-beam configuration. For comparison, the sensitivity obtained under similar conditions using an orthogonal pump-probe configuration is shown by the grey trace in Figure 52. The reduced noise in the 100–200-Hz band occurs in part because the laser-amplitude noise is suppressed by the differential detection in the Faraday rotation measurement. The use of a single-light-field configuration leads to a considerable simplification in the optical arrangement when compared with the two-beam pump-probe configuration, but suffers from increased susceptibility to laser-amplitude noise. We note, however, that laser-amplitude noise cancellation can be achieved in the single-beam configuration when the system is operated in the gradiometer mode or when the optical power at the entrance to the cell is monitored.

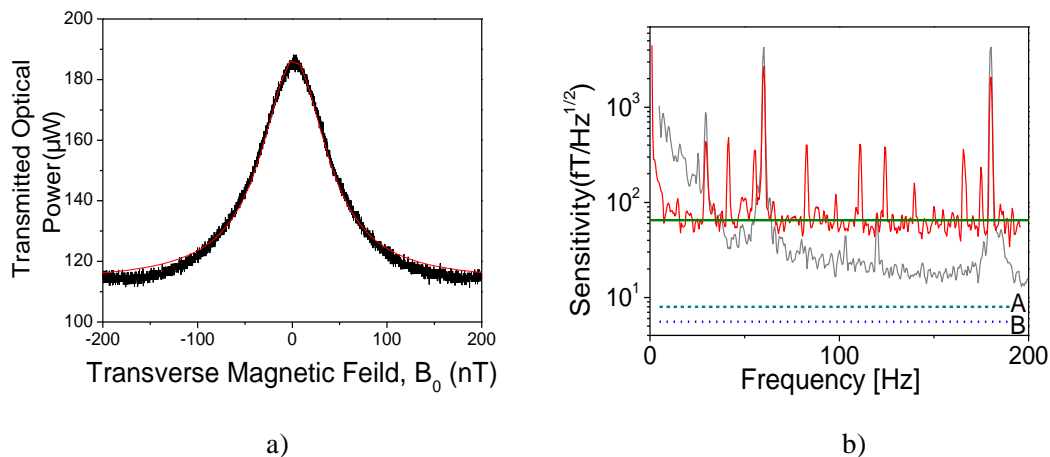


Figure 52 Results in the SERF regime.

The results presented above show that a SERF magnetometer with a sensitivity below $100 \text{ fT}/\sqrt{\text{Hz}}$ is feasible in a MEMS alkali vapor cell using a simple, single-beam optical configuration. This suggests that highly sensitive SERF magnetometers can be made equally small and low in power by using similar MEMS fabrication techniques. Magnetic noise originating from electric currents in the various active and passive components will undoubtedly be more important for highly compact devices. Our estimations, however, suggest that this noise is either negligible on a millimeter length scale or can be mitigated with minor modifications to the optical design or the electronic packaging.

3.2 Further investigation of SERF in MEMS cells

In the first part of this task, we performed initial investigations of the spin-exchange relaxation free (SERF) regime in miniature magnetometers. We developed a magnetometer based on a $2 \times 1 \times 3 \text{ mm}^3$ MEMS cell with a sensitivity below $70 \text{ fT}/\sqrt{\text{Hz}}$. It used a single laser beam in a very simple setup. In order to reach these extremely good sensitivities, we had to operate the magnetometer in a magnetically shielded environment.

We also investigated the performance of such a magnetometer in the Earth's field. In order to do that we set up a new laser system with a stronger pump laser and a weak probe laser. Furthermore, we designed and built a low-noise shielded environment to perform such measurements under controlled conditions. Here, we added a ferrite shield as the inner layer of our two-layer mumetal shield. Ferrite as a non-conducting material does not produce magnetic noise due to thermal currents inside the shielding material. The noise of this shield is $4 \text{ fT}/\sqrt{\text{Hz}}$, while a mumetal shield of the same dimensions would produce $25 \text{ fT}/\sqrt{\text{Hz}}$.

We performed the experiment in the following manner: In order to extend the SERF regime into the earth field the collisions between the alkali atoms have to be much faster than the Larmor precession rate ($\sim 175 \text{ kHz}$ in earth field for cesium). This is done by increasing the alkali density, i.e., heating the cell. For cesium the temperature required would be above $250 \text{ }^\circ\text{C}$, and for rubidium even $300 \text{ }^\circ\text{C}$.

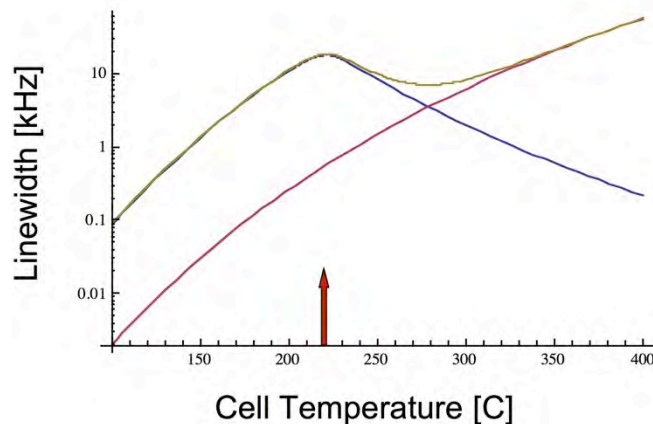


Figure 53 Linewidth of the magnetometer resonance as a function of cesium temperature (yellow trace). It has two contributions: Spin-exchange collisions at low cell temperatures (blue trace) and spin-destruction collisions at high cell temperatures (red trace) The red arrow indicates the point where the collision rate between the cesium atoms equals the Larmor frequency in earth's field.

Figure 53 shows a calculation of the resonance linewidth as a function of cell temperature (yellow line) (see ¹⁴ for details). At lower temperatures, the line width increases proportional to the cesium density due to spin-exchange collisions. It reaches a maximum when the alkali collision rate is equal to the Larmor frequency (blue line). At higher temperatures, the collisional

relaxation due to spin-exchange becomes suppressed and the line narrows, until it is limited by spin-destruction collisions (red line). We therefore tried to operate the magnetometer around 275 °C (for cesium). At this high density, it is difficult to obtain efficient pumping of the atoms, since all light resonant with the atoms will be absorbed within a few hundred micrometers of the cell. This problem is circumvented by choosing the right detuning of the pump laser from optical resonance. The magnetic field is then measured in a resonant way as a modulation signal of the probe laser rotation. This is different from usual low-field SERF magnetometers that measure the DC absorption. A series of measurements can be carried out measuring the linewidth (bandwidth) of the magnetometer as a function of cell temperatures (above 200 °C) for different detunings and intensities of pump and probe lasers. This would allow for the optimization of the performance of the magnetometer.

Task 4. Electronics Design

In this section we describe our work in designing and prototyping the electronics system for operating and interrogating the physics package. The previous results described utilized lab instrumentation to drive signals into the cells. This allowed us to determine the characteristics of the magnetic resonance and the requirements for the electronics.

Block diagrams of the required electronics for dual- and single-beam geometries are shown in Figure 54 and Figure 55.

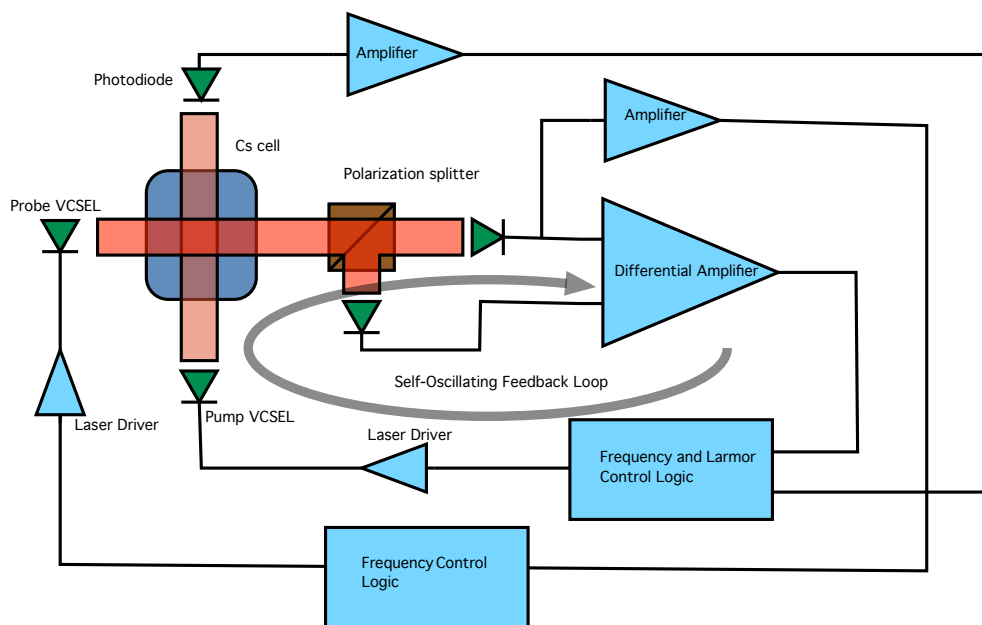


Figure 54 Electronics block diagram for the dual-beam geometry.

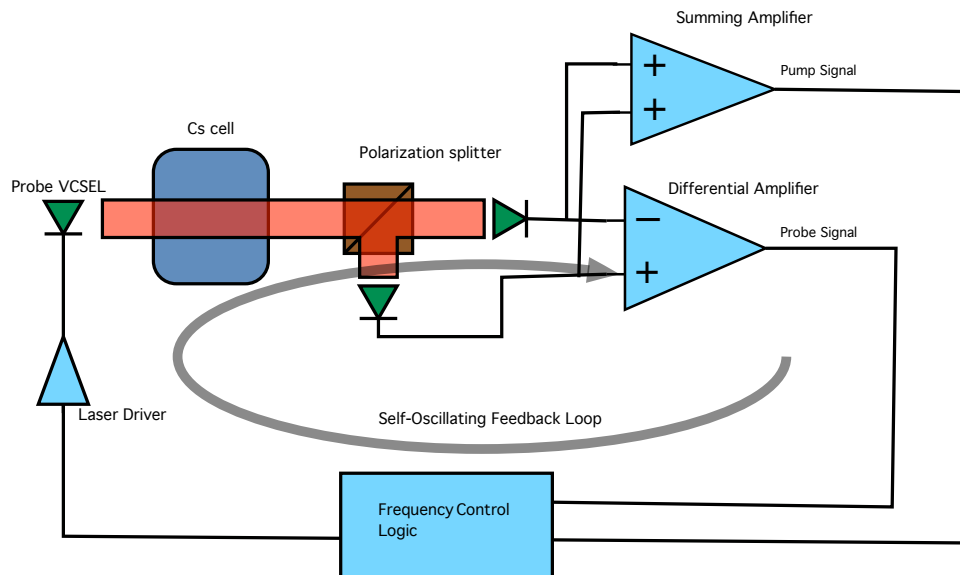


Figure 55 Electronics block diagram for the single-beam geometry.

Low noise is achieved through the differential polarization analyzer, where much of the laser amplitude and frequency noise is seen as a common mode signal and subtracted out in the differential amplifier. More detail on the various functions is described in the specific tasks below.

4.1 Physics package control circuitry

The physics package control consists of the following elements:

Cell heating and control. This system must minimize stray magnetic fields and ensure that the frequencies used in generating the heater signal do not interfere with the operation of the magnetometer.

Laser frequency control. The laser frequency is modulated by making changes in the junction temperature. This is done in two stages. A coarse heater is used to heat the VCSEL chip itself. The current through the junction also modulates the junction temperature. The thermal time constant of the junction plays a significant role in modulating the laser frequency. The response of the laser's frequency as the input current is modulated is significantly phase shifted and delayed.

Cell heating

Heating with a sine wave allows for low noise operation, since there are no higher harmonics of the heater signal, but is very inefficient. The highest efficiency would be obtained by modulating with a square wave, but this has far too many higher-order harmonics to be tolerated. We have opted to make a compromise heating system where we apply a wave form with the shape of:

$$Y = \sin(t) + A\sin(3t)$$

If we normalize the waveform so that its peak-to-peak amplitude is as large as the supply voltages will allow, we get wave shapes as shown in Figure 56:

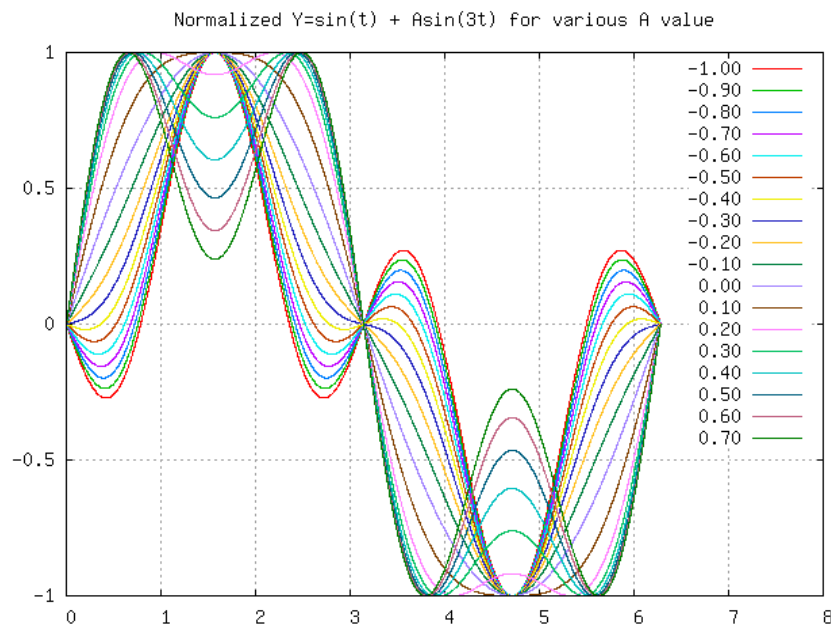


Figure 56 Waveform for cell heaters.

The range of A values from -1 to +0.2 are the most interest. The RMS value of the waveform varies with the value of A over that range. If we compute the power into a load, assuming 1V supplies and a 1 Ohm load, we can graph the necessary value for A for various amounts of power, as shown in Figure 57.

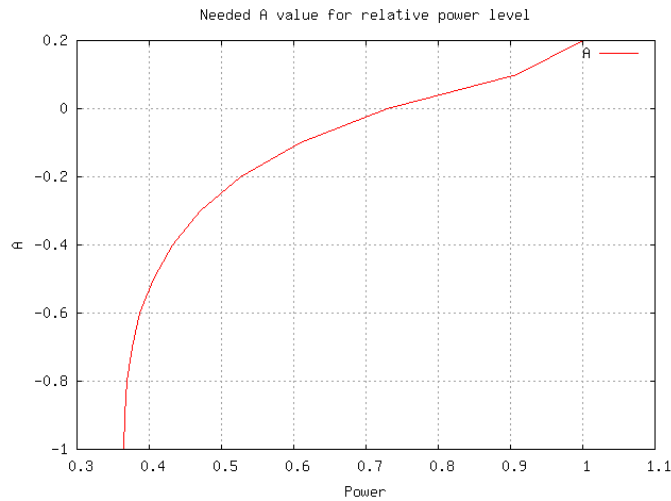


Figure 57 Required value of the third-harmonic amplitude, A, for desired power level.

From Figure 57 we see that we can obtain about a three-fold range of the power in the heater by changing the 3rd harmonic content. For lower power levels, a relative 3rd harmonic setting of -1 can be maintained as the total amplitude is reduced.

Figure 58 show a graph comparing the efficiency of the above method compared to a simple sine function.

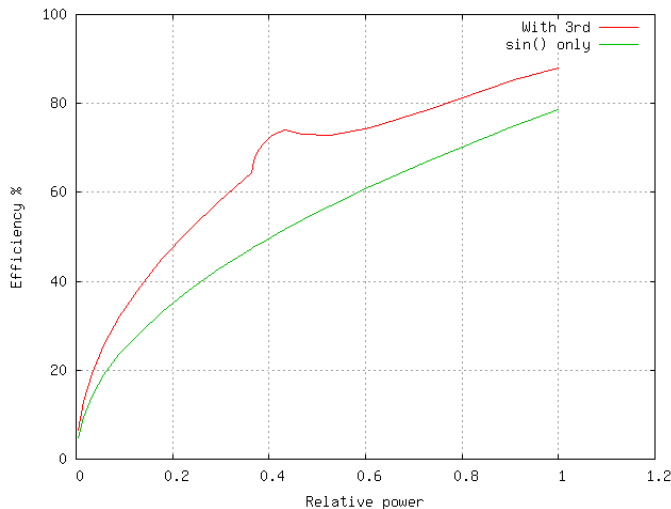


Figure 58 Efficiency of sine wave heating vs sine wave with 3rd harmonic.

There are many considerations in choosing the frequencies we can use for heating. First of all, the frequency must be a multiple of the typical measurement frequency of the counter so that we don't see a beat between the fields the heater creates and the measurement process. Secondly, the frequency must be such that it does not beat with the Larmor servo's modulation or the low harmonics of it. Thirdly, the frequency must be low enough that we can be sure that the

harmonics for distortion in the Larmor band are small. Finally, the heater frequencies must not beat with the Laser servo's modulation.

Heater amplifiers

This circuit is essentially an audio power amplifier for the heater waveforms. The heater waveforms are made on the DAC board and then amplified in this circuit.

The heater PCB consists of 4 identical audio power amplifiers. These are used in pairs to drive the heaters. By using a balanced drive on the heaters, we eliminate most of the electrostatic coupling from the heater into the photo cell circuits.

The first thing we do to the heater waveform is remove any DC and strip off any high frequencies. This makes a clean signal centered around the half way point of the power supply. U1C and U1D invert the signal for the inverted side of the balanced drive.

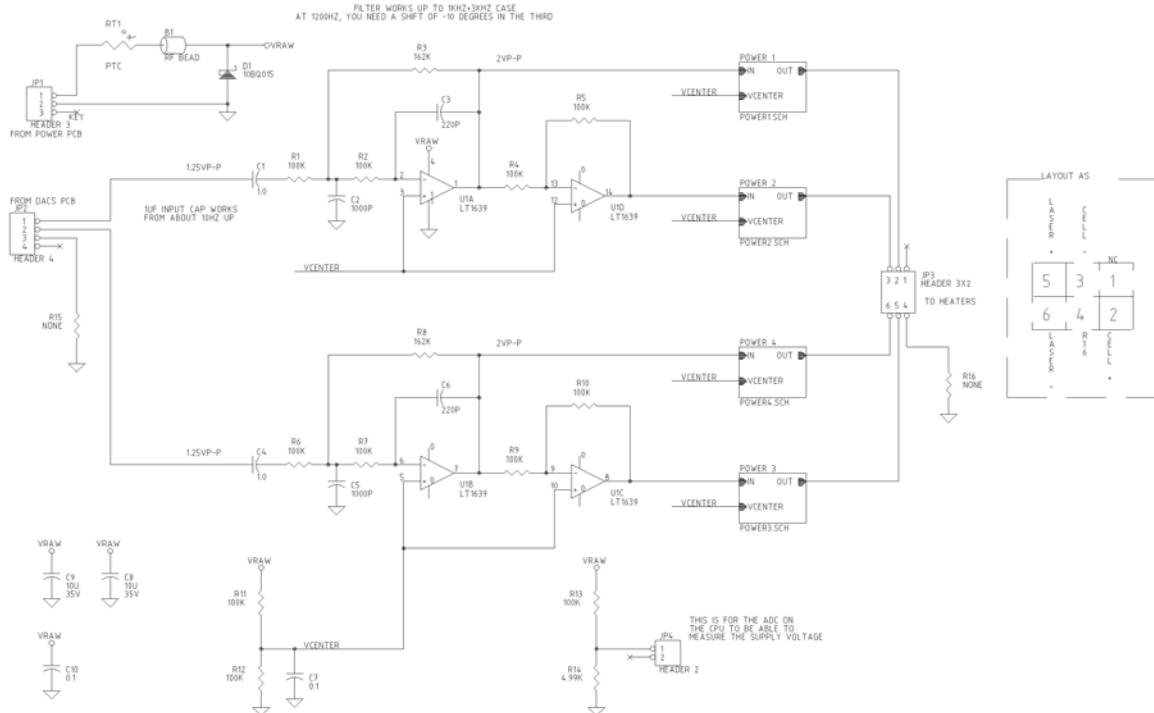


Figure 59 Heater amplifier printed circuit board, containing 4 power amplifiers.

There are 4 identical amplifiers, one of which we describe here. Please refer to Figure 60.

If we ignore Q201 and Q202 and consider R203 to be zero ohms, the circuit looks like a simple non-inverting amplifier with a gain of about 6. R201 and R202 would determine the gain.

Still consider R203 as a short and examine Q201 and Q202. If U201 must deliver current to pull its output up, it must be drawing a current on its positive supply pin. This current will bias Q201 on and Q201 will help the op-amp pull up on the voltage. The action is much the same when the op-amp pulls down. Q202 turns on, pulling down the voltage.

Now consider when R203 has its actual value. U201 is now pulling up and down on a point connected to R203 and R204. R203 and R204 work as a voltage divider so that the op-amp's output has a smaller voltage swing than the output of the circuit. This means that Q201 and Q202 will make the actual swing on the load and the op-amp won't be doing the hard work.

For very small swings and light loads, the op-amp doesn't pass enough current to turn on Q201 or Q202. It is the output of the op-amp via R203 that drives the load. This makes the voltage on pin 6 of U201 look distorted even though the output isn't. Near the zero crossing, the output of the op-amp must swing much faster than it normally does for the rest of the waveform.

Q201 and Q202 don't act instantly. This delay could lead to instability but C201 prevents U201 from reacting to this small delay. C201 provides local feedback that is not delayed by the transistors.

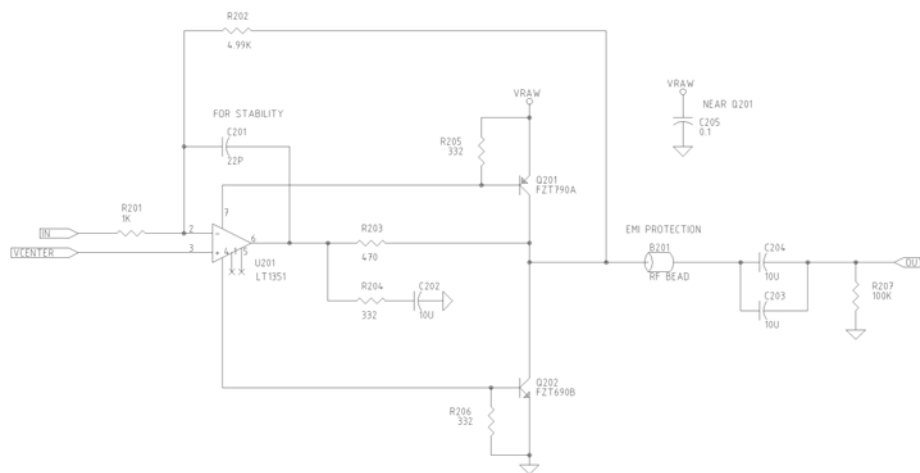


Figure 60 Heater amplifier

Laser Frequency Control

The frequency of the laser is controlled by the VCSEL heater and the current through the device. The VCSEL heater provides a coarse frequency control, and the junction current provides a finer frequency control (through the heat generated in the junction) as well as a light amplitude control. These currents are controlled by a microprocessor, which must first find the proper Cs line, then lock onto it.

Finding the initial lock

The software that does the locking process implements a state-machine which steps through states that represent the same operations as a person would do when locking the laser onto the absorption line.

Initial State: This is the state that is caused by a reset or power on. All of the internal variables are set to their default values and the software steps to the next state after one millisecond.

Wait-For-Cell State: The laser system can't be locked until the cell reaches the operating temperature. The state machine will remain in this state for several minutes in a cold environment. Once the cell has reached temperature, the software will step to the next state.

Search-Cold State: With the laser heater set to its minimum value, the software checks for the detection of the absorption line. On some lasers, the running temperature of the laser will be only slightly higher than that of the cell. This check allows these lasers to be used in production sensors.

Search-Up State: The laser heater is gradually increased while looking for the absorption line. Normally, the line will be detected at some point and the state machine will jump to the "Large sweep tuning state". Extra states exist as protection against unexpected situations such as the case of a system being tested. Depending on the specific laser, this state may last as long as 20 seconds.

Search-Hot State: If the laser heater reaches the maximum allowed it is held at that limit for a fixed time while the software continues to check for the absorption line. This state should not be used in a working system.

Search-Down State: The laser heater is slowly decreased while the software checks for the absorption line. When the heater reaches the minimum, we loop back to the "Search Cold State".

Large-sweep-tuning state: A larger than normal sine wave is applied to the laser current. This takes the laser's wavelength past the absorption line twice per cycle. The laser's heater is slightly adjusted up or down as needed to center the sine wave on the absorption line. The software remains in this state for nominally 0.1 seconds. It only leaves this state when the alignment error is under 1% of the sine wave's amplitude.

Centering-tuning state: The amplitude of the sine wave in the laser current is reduced and the center line is moved to the optimal value over the period of one second.

Large-Modulation State: The servo operation is enabled with the amplitude of the sine wave larger than normal so that the servo rapidly moves to its final value. The software remains in this state for a nominal time of one second.

Final-Servo State: The amplitude of the sine wave is reduced to its final value and the servo is now operating normally. The state machine remains in this state until the power is turned off.

Decoding of the laser's alignment once locked:

The laser alignment is indicated by a signal on the photo detector as the laser is dithered back and forth slightly by a small sine wave in its current. Because the absorption line is composed of two lines that are broadened, the signal on the photo cell contains a strong component at the fourth harmonic of the dither frequency and any error in alignment of the line creates a strong third and fifth harmonic and almost no fundamental component.

The normal lock-in amplifier method will not work for a signal of this type. Instead of multiplying by a sine function before integrating, a waveform composed of weighted odd harmonics is used. The resulting error signal is not linear but is monotonic with misalignment. It is a close match to the hyperbolic sine function, which the servo design assumes.

The alignment error decoding software applies a two-pole low pass filter to the error signal. One pole is nominally at 27Hz and can be ignored from a servo stability point of view. The dominant pole is at 1.7Hz and must be considered in the servo design. The sampling rate of the ADC is 40KHz and thus Nyquist is well above the frequencies of interest in the servo design.

4.2 Signal interrogation circuit design

Probe modulator

Theory of Operation:

In systems such as atomic clocks and “swept” magnetometers, the electronics must tune an oscillator such that it operates at the center of some resonance in a quantum physical system. This may be achieved by using the fact that the effect of a signal applied to the quantum physics is strongest when the signal is tuned to resonance and decreases when the signal is mistuned. As the frequency of the signal applied to the quantum physics is varied slightly, the decrease in the effect of the signal for each direction of variation is measured. If there is a difference between the amount of decrease for the two directions, the center of the sweep is adjusted to make them equal. In this way, the electronics will have its center frequency aligned with the quantum physical resonance.

There are several issues which must be addressed in the design. The modulation of the frequency needed for detecting the center of resonance should not be allowed to appear in the output signal needed for counting. In addition, the modulation must be symmetrical about the center. The simplest frequency modulation methods do not have good enough linearity to ensure symmetry. Furthermore, when a signal is frequency modulated wide side bands are created, following the

shape of a Bessel function. This can cause a problem in magnetometers because some of the energy in the side bands appears at low frequencies, where the magnetometer signal of interest lies.

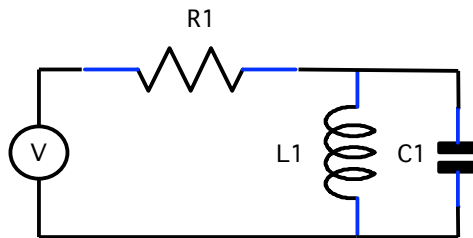
Some quantum physical signals are decreased by the existence of these side bands, because they cause the resonant line to broaden but do not contribute any information about the alignment between the signal and the resonant frequency. If we construct the waveform from a small collection of discrete frequencies near the resonance, the resulting waveform will not have any energy far from the resonance. If the discrete frequencies are symmetrical about a central “carrier frequency”, the relative effect of the frequencies to each side of the carrier can be used as the method of detecting the mistuning.

A three-frequency electronic circuit will serve as an analogy:

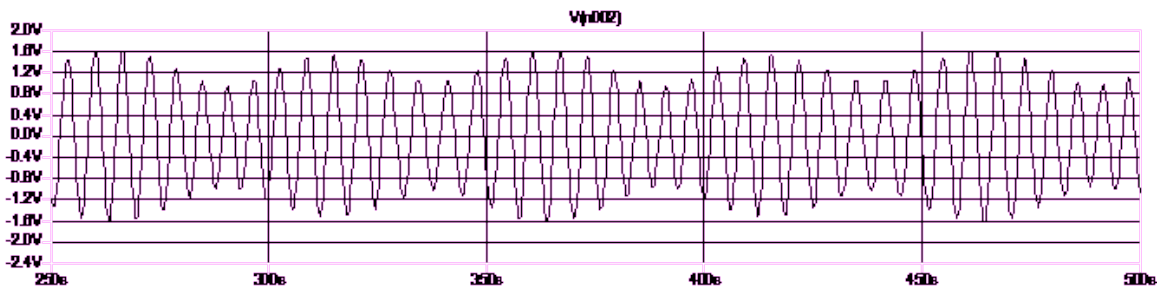
If we apply:

$$V = \cos(2\pi \cdot 0.149154 t) + \sin(2\pi \cdot 0.159154 t) + \cos(2\pi \cdot 0.169154 t)$$

to a tuned circuit such as :

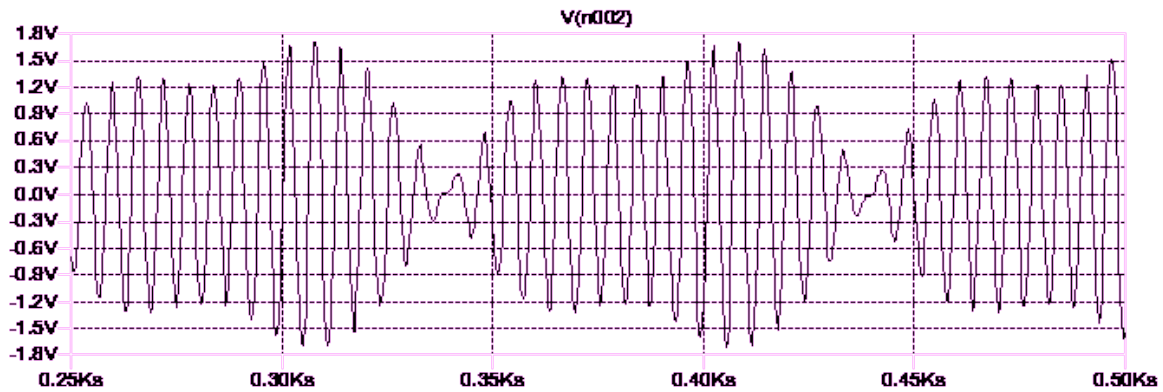


the voltage across L1 is shown below:



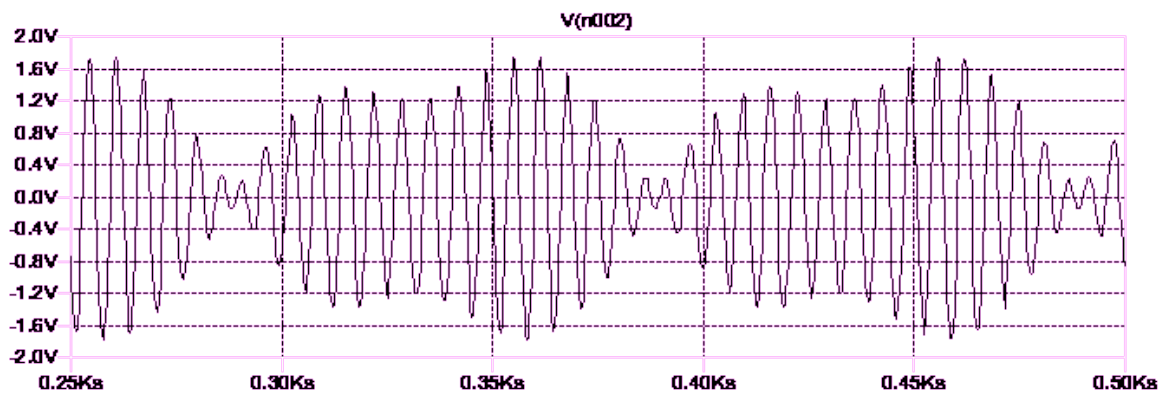
Note that the amplitude modulation appears to be at 0.02Hz.

If the value of L1 is changed to 1.1, this causes a misalignment between the carrier and resonance:



Notice that there is now a large 0.01Hz component obvious in the signal.

If the value of L1 is changed to 0.9, this causes a misalignment in the other direction:



Notice again that large 0.01Hz component, but the phase of the modulation has been inverted.

Quantum physical systems internally respond to the composite signal in a very similar manner. Commonly, the envelope of the waveform is what is available as the output of the system. It is easy for the electronics to decode the modulation seen to create an error signal.

There are two methods for the production of the collection of frequencies. One is easier to implement digitally in some programmable device such as an FPGA and the other is easier to implement in a more analog method.

Digital method:

In a digital system, performing a multiply is much more expensive than adding in terms of logic gates or processor cycles. The design for the digital case avoids multiplications.

The digital method is most efficiently explained in the form of pseudo code with embedded comments:

```

inputs:
    Frequency : integer          -- May not be in Hz
    Offset : integer             -- May not be in Hz
output:
    Y : integer                  -- connects to the DAC
declare variables:
    X1, X2, X3 : integer
begin code:
    X1 = NinetyDegrees           -- Starting point when
    X2 = 0                       -- .. power is first applied
    X3 = NinetyDegrees           -- .. to the system.

    Repeat forever
        wait for edge of input clock
        X1 = X1 + (Frequency - Offset) -- Step forwards in time
        X2 = X2 + Frequency          -- Any carries out of the tops
        X3 = X3 + (Frequency + Offset) -- .. of the values are discarded
        Y = sin(X1) + sin(X2) + sin(X3)
    end of repeat loop

```

In actual implementation, the repeat loop may take 3 cycles of the input clock to complete so that the $\sin(\omega t)$ function can be implemented as a simple table look up. A new value of Y would be built up in a temporary variable and only transferred to Y when the whole value is computed

Analog balanced modulators are often used in radio electronics. Given a carrier and a modulation frequency signal inputs, they produce an output that contains frequency components at the sum and difference of the inputs. We use a similar method which we call Quadrature Amplitude Modulation(QAM). QAM is a method of modulating a signal using a balanced modulator. It requires that a balanced modulator be fed with a version of the carrier signal that has been shifted in phase by 90 degrees. Given a modulating signal with amplitude A, we have:

$$Y = \sin(\omega t) + A\cos(\omega t)$$

Using an analog multiplexer, one can construct a stepwise approximation to a sine wave. This is done by applying the voltages for various the points on the desired waveform to the inputs of the multiplexer, and clocking the multiplexer through those values.

If a stepwise approximation of the signal is acceptable, the same multiplexer can construct both the $\sin(\omega t)$ and the $A\cos(\omega t)$ terms of the equation above. Each input of the multiplexer is fed with the sum of the two voltages or currents. The multiplexer then steps through the wave form as in the simple sine wave case.

Circuitry

We construct a Larmor signal and modulate it for the laser drive. The modulated Larmor signal goes to the DACs board where the amplitude and direction of the laser modulation is controlled.

The laser modulation generator

This circuit takes in an error signal to steer a Voltage Controlled Oscillator (VCO) and a modulation signal and produces a Quadrature AM modulated output and a copy of the VCO for the counter. The process is broken into two main parts.

The VCO section:

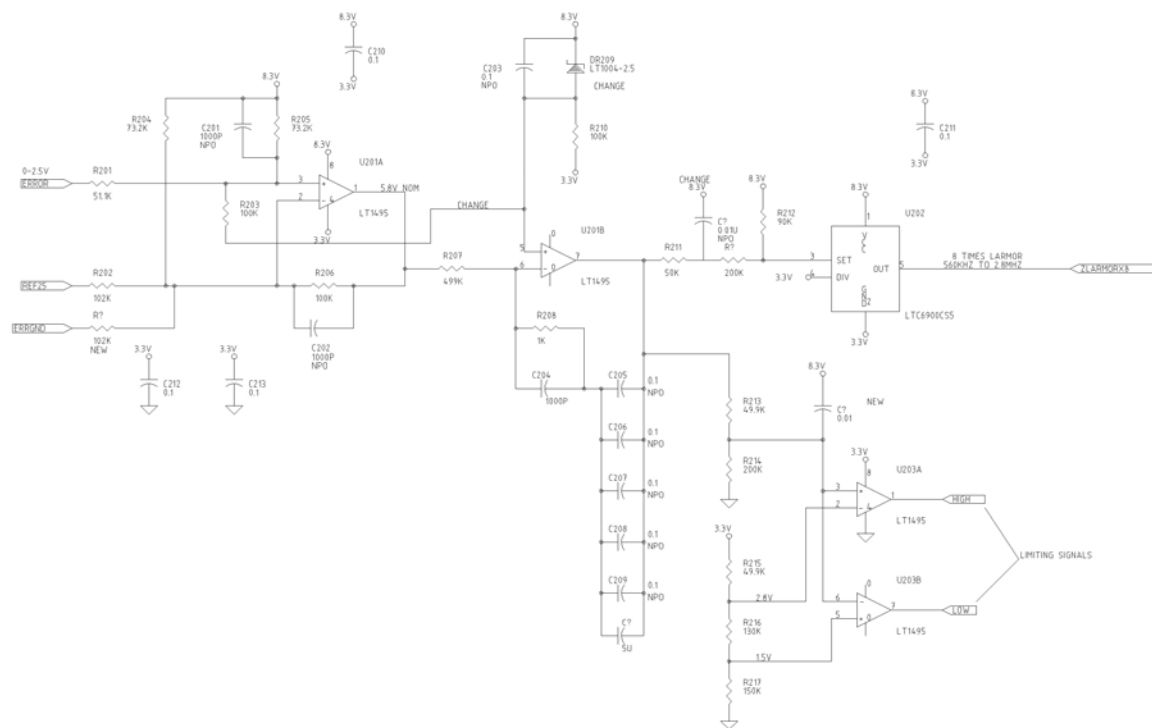


Figure 61 Laser modulation VCO.

U201A is a differential amplifier that changes the center point of the error signal from 1.25V to 5.8V. This is done because this entire circuit is powered from the 5V difference between the 8.3V and the 3.3V. These supplies are used to save overall system power.

U201B is an integrator. R207 and the parallel combination of C205 through C209 sets the rate at which the integrator responds to a signal from U201A. R209 and R210 make the center point for the input to this integrator 5.8V. This means that, ideally, 5.8V from U201A would cause the output of U201B not to move. U201A produces 5.8V when the DAC on the CPU is producing 1.25V.

Normally the gain of an integrator falls off as frequency increases. R208 and C204 create a flat section in this curve from about 16Hz to about 8KHz. This is done because we need to be able to follow 180Hz radiation from the power lines.

U202 is a resistor controlled oscillator that is slightly modified. R212 would normally set the frequency of this oscillator. The set pin is held by internal circuits at 1V less that the plus supply and the current through R212 would set the frequency. R211, in this design, takes some current away from the set pin and thus lowers the frequency. This is how the frequency control is performed.

Laser drive amplifier:

The laser current circuit is easiest to explain if we at first ignore the capacitors. The reference and the DAC output are combined by R401 and R402 to make the current setting. This allows the current to be set over a 2:1 range.

J401 is the connection to the laser. There is a 1K resistor at the laser for ESD protection. The laser its self has about a 2V forward drop.

R411 and R412 pull the inputs of U401 up to the middle of its span but do not affect the gain of the amplifier circuit because the impedances on the two inputs are matched.

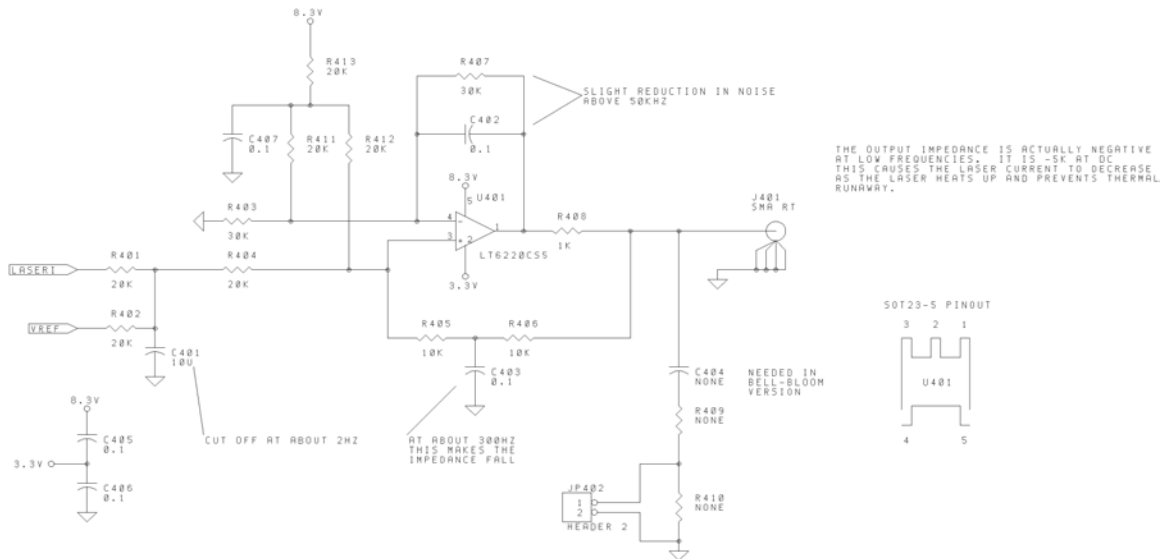


Figure 62 Laser drive amplifier.

Photodiode preamplifier

Our photodiode preamp design is intended to produce very low noise performance with a low power consumption.

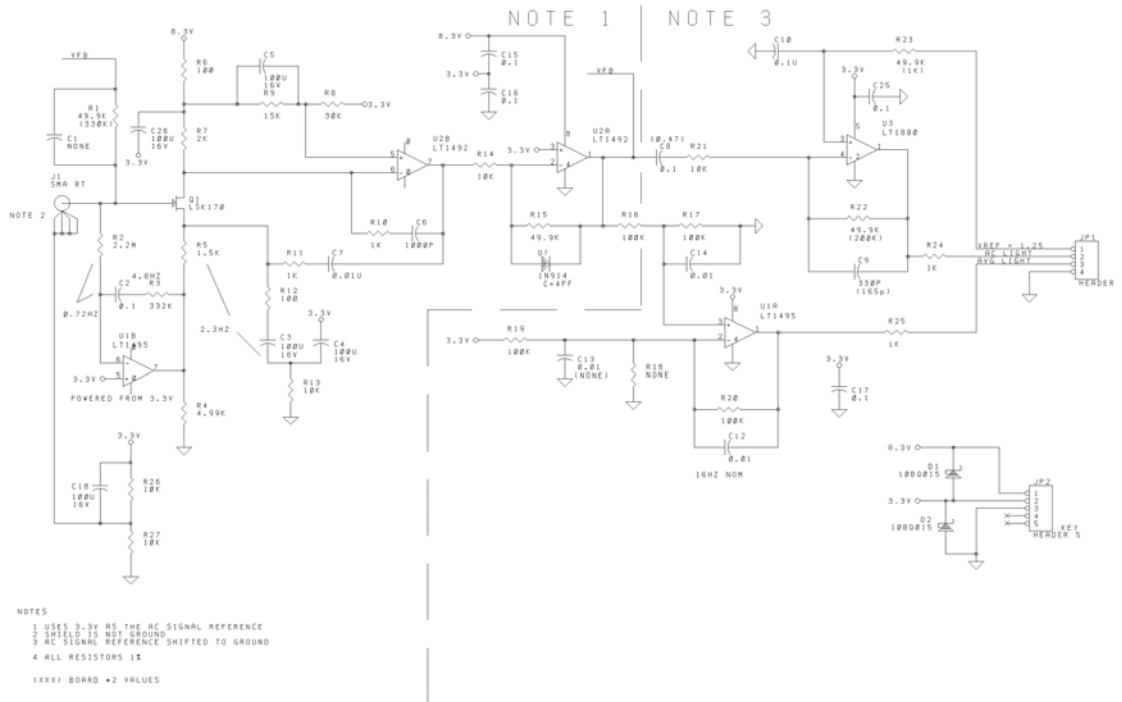


Figure 63 Photodiode preamplifier.

The circuit is a transimpedance amplifier with a few extra elements added.

The gate of Q1 is very similar to the inverting input of an op-amp. The feedback through R1 creates a low impedance at that point. The circuit is easiest to understand by first assuming the gain is such that the AC voltage on the gate is small.

The source of Q1 has a slightly complicated circuit connected to it. The important parts here are R12, C3 and C4. These provide a fairly low impedance AC path to ground for the source of Q1. This means that the current from the source to drain of Q1 will vary greatly for small changes in the gate voltage on Q1.

The drain of Q1 gets a DC current through R7. The AC portion of the current flows to the inverting input of U2B. The inverting input of U2B presents a low impedance to the drain of Q1 so that the drain capacitances of Q1 have less impact on the performance of the circuit.

R10 and C6 set the gain of the U2B stage. The gain at DC is very large. At higher frequencies it decreases because the reactance of C6 decreases. In this range, it produces a phase lag of nearly 90 degrees. When the reactance of C6 falls below the resistance of R10 the gain stops decreasing and the phase lag is reduced towards zero.

The feedback through C7 and R11 to the source of Q1 makes the gain of the entire circuit from Q1's gate to U2B's output very nearly equal to 10. This removes most of the unit to unit variations in Q1's gain.

U2A is a simple inverting amplifier with a gain of 5. This brings the total gain to this point to a total of 50. This is enough so that the input impedance of the whole circuit is about 1K. To see this, assume that the gate of Q1 varies up and down by 1mV. The output of U2A will vary down and up by 50mV so R1 will have about 51mV on it, so about 1uA of modulation in the current will be seen. From Ohms law, 1mV/1uA comes out to 1K.

At this point we have completed the description of the transimpedance function. The following circuitry further amplifies and filters the signal before it is sent to the ADC. The upper circuit is a high pass filter that only passes the AC signal. The lower circuit passes the low frequency part of the signal. Using two amplifiers in this manner has the advantage that we can use different gains for the two paths so that each path uses most of the dynamic range of the ADC it is applied to.

Now consider U1B on the left side of the schematic. This op-amp monitors the average voltage on the gate of Q1 and adjusts the current through R5 to keep that voltage at exactly 3.3V. This means that it trims out any shifts in the gate cutoff voltage of Q1. This op-amp is very slow and very low current. R4 is used to provide enough current.

R26 and R27 set the voltage on the shield of J1. The difference between this voltage and 3.3V is what sets the back bias on the photodiode. A small back bias on a photodiode decreases its capacitance. Too much back bias will cause noise from leakage currents.

The C3, C4 and R13 circuit is used because we need to ensure that the capacitors never get reverse biased.

R6, C6, and C25 are necessary to keep any AC on the +8.3V power supply out of the signals on Q2B. Because of the circuit topology, R7 and the voltage drop on R9 determines the operating current of Q1. The feedback loop works to keep the voltage drop on R7 equal to that on R9.

4.3 Performance Analysis

As noted before, there are many ways to operate an optically pumped magnetometer. In this project, we considered many possible methods, including single and dual beam, swept systems and self-oscillators, polarization-rotation and absorption probe methods.

Since we wish to obtain a wide-band signal, we wish to operate the sensor as a self-oscillator. The frequency of oscillation is proportional to the magnetic field, and since we wish to follow rapidly changing magnetic fields, we will need to follow a rapidly changing oscillation frequency. The fastest way to do this is with a self-oscillator, which uses feedback at the resonant frequency to oscillate at the Larmor frequency. Methods that determine the resonant frequency by scanning a signal source across the resonance in some manner require a lot of computational power to track a rapidly changing resonance.

A simple block diagram of a feedback oscillator is shown in Figure 64. The cesium cell is represented by the filtering network, H , and our electronics is represented by the amplifier feedback element, G .

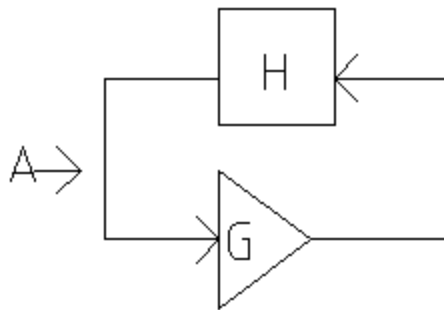


Figure 64 Canonical feedback oscillator.

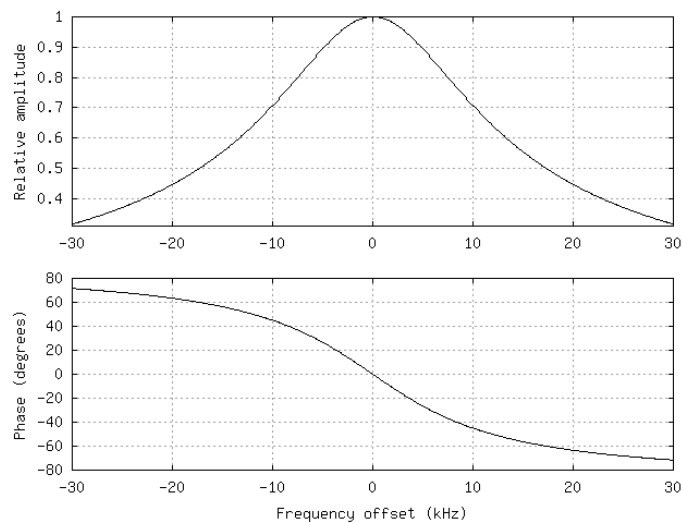


Figure 65 Response of canonical oscillator.

An oscillating system such as that shown will oscillate at the frequency for which the feedback is in phase with the input (as long as the gain at that frequency is greater than unity). Any phase shifts in the circuit elements will change the frequency of oscillation. Thus, an essential element of our design analysis is the consideration of the phase shifts that arise in the various elements of the oscillating system.

For good magnetometer operation, the phase shift of the amplifier must be small, nearly constant, and repeatable from unit to unit. Small phase shift will cause the oscillation frequency to be offset from the Larmor by some amount. If this offset is known and constant, it may be corrected for. If this offset drifts, this will cause low frequency noise.

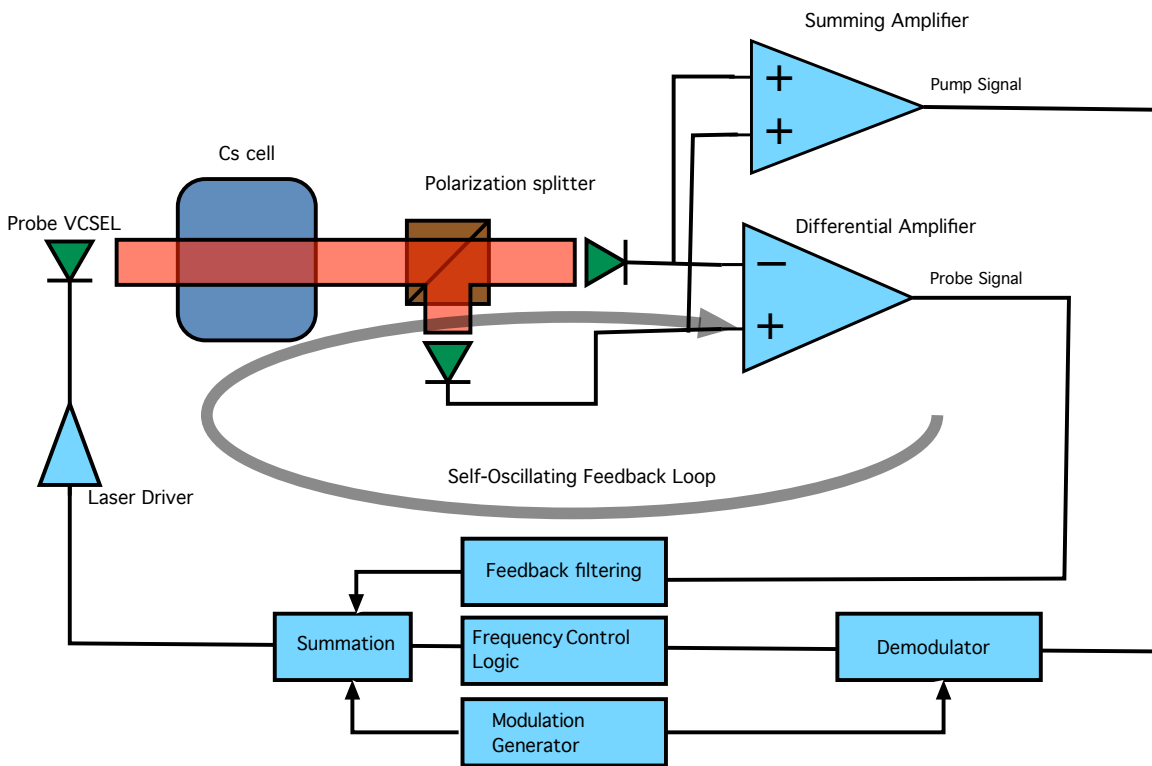


Figure 66 More detailed circuit topology of self-oscillating magnetometer

Feedback Loop Analysis

Figure 66 shows in more detail the topology we are working with. There are several sources of phase shift and noise that must be carefully considered. The following issues are among those that need to be addressed in order to have a properly working magnetometer

First of all, it is frequency modulation of the laser light that carries our signal information. The frequency of the laser is controlled by the temperature of the laser junction, which is controlled

by the input current. The thermal time constant is very near the band of interest, leading to rapidly changing phase across our signal band. As noted above, changes in phase mean a change in the magnetometer output, and these must be very carefully known and controlled.

Secondly, our signal of interest is that due to the polarization rotation of the probe beam. This rotation causes small changes in signal amplitude at the output of the differential amplifier. However, the pump beam must also be modulated at the Larmor frequency, producing a common-mode amplitude variation. This common mode signal amplitude is two orders of magnitude larger than our probe signal of interest. Thus, with a finite common-mode-rejection-ratio, there is a second parasitic feedback loop in our circuit. This feedback loop is not affected by the Larmor resonance, and could therefore oscillate at any frequency, and prevent the desired oscillations at the Larmor frequency. This effect is made much worse if the pump laser is modulated by high frequencies, as the CMRR must be very low over a wide frequency range.

Finally, because the phase shift is only a gradual function of frequency due to the high temperature and buffer gas pressure of this sensor, slight variations in phase have a large effect on the frequency of oscillation, and therefore, the magnetometer output. Phase shifts are a function of component values, which drift with temperature. This effect must be carefully analyzed.

Laser Modulation Analysis

The target phase accuracy and the phase vs frequency slope determine the maximum unit-to-unit variation in the total phase shift as 0.03149 degrees. Further, this determines the position of the poles for the filters in the Larmor loop. The high cut pole must be at least 6.68 MHz, and the low cut pole below 3.662 kHz. Given the drift in Hz per degree C, we can write the allowed phase variation as 0.0001574 degrees (phase shift) per degree C. This further limits the high- and low-cut poles in the system.

At this point we consider two methods of modulating the pump beam. With sine-wave modulation the pump frequency sweeps smoothly on and off the absorption line. We may also use a square-wave modulation, in which the laser jumps on the line and off the as quickly as possible. We consider in detail the sin-wave modulation method below.

We need the absorption in the cell to have an AC component that is in phase with the Larmor signal. Because the pump laser's wavelength depends on the temperature of the active part of the laser, there is a lag between the current to the Laser and the absorption. The driver circuit needs to correct for this by causing a phase lead in the current. Because the light produced by the laser depends on the current, the required phase lead is not simply equal to the phase lag of the thermal time constant. Because the thermal time constant decreases the amplitude of the wavelength modulation, the amplitude of the current modulation must compensate for this too.

The calculation is done by assuming no phase shift in the pumping light's modulation and then computing the phase of the Larmor that would be produced. Once this phase is known, we know the amount of phase correction to apply to the pump drive signal to obtain zero phase.

The fact that the optical line is composed of two lines, one for the MF=3 and one for the MF=4, makes the calculation more complex. As the laser is swept onto the line from the "lower current" side, it at first pumps the MF=3 state more strongly. Near the peak of the swing, the Laser is pumping the MF=4 state more strongly. After the peak, the laser again sweeps through the part of the line where the MF=3 is pumped more strongly.

The current, which is modulating the wavelength, also affects the light intensity. We must compute the amount of light and the percent absorption at each point in the cycle and multiply the two to compute the amount of light absorbed at each instant in time.

Because the MF=3 and MF=4 absorption curves differ, the calculations must be done for each line independently and then added. The Larmor frequencies of the MF=3 and MF=4 differ slightly. We must select a compromise Larmor frequency and adjust the phase of the computed MF=3 and MF=4 Larmors accordingly. For this compromise, the Ideal Larmor condition is used.

The nonlinear nature of these effects causes the correcting phase to be a nonlinear function of the Larmor frequency. For this reason a table of several points across the band of interest must be produced. The tables below summarize our analysis of these effects on the phase of the signal around the oscillation loop. The final column shows the accuracy this requirement imposes on the component values of the circuits.

Larmor kHz	Corrected Amplitude mAp-p	MF=3 phase Degrees	MF=4 phase Degrees	Combined phase Degrees	Required accuracy %	Required tempco PPM
69.97	0.4369	19.86	20.84	20.23	8.545	7.455
101.1	0.4738	26.83	28.25	27.36	6.084	5.308
132.2	0.53	32.42	34.26	33.11	4.828	4.212
163.3	0.5731	36.76	39.01	37.6	4.088	3.567
194.4	0.6314	40.04	42.71	41.04	3.617	3.156
225.6	0.6937	42.48	45.54	43.63	3.303	2.882
256.6	0.7589	44.25	47.7	45.54	3.09	2.696
287.7	0.8263	45.49	49.32	46.93	2.944	2.568
318.8	0.8955	46.33	50.52	47.9	2.845	2.482
349.9	0.9661	46.84	51.37	48.54	2.782	2.427

Table 3. Pump signal phase modulation

Since typical temperature coefficients for precision components are about 50 ppm / °C, the above requirements are very strict. The best that might be accomplished using custom components might be about 5 ppm. Better than that requires integrated circuit techniques, which are beyond the scope of this work.

Changes in the amplitude of the modulation of the pump laser and value at the positive peak both affect the phase difference between the pump modulation and the absorption.

Larmor kHz	MF=3 phase effect Degrees / GHz	MF=4 phase effect Degrees / GHz	Combined phase effect Degrees / GHz	Required accuracy %	Required tempo PPM
69.97	-0.1628	-0.096	-0.138	10.56	528.1
101.1	-0.2341	-0.139	-0.1985	7.344	367.1
132.2	-0.3042	-0.181	-0.258	5.648	282.3
163.3	-0.3727	-0.223	-0.3166	4.605	230.2
194.4	-0.4394	-0.264	-0.3737	3.901	195
225.6	-0.504	-0.3044	-0.4292	3.3397	169.8
256.6	-0.5663	-0.3438	-0.4828	3.019	150.9
287.7	-0.6259	-0.3823	-0.5346	2.737	136.3
318.8	-0.6828	-0.4198	-0.5842	2.495	124.7
349.9	-0.7369	-0.4563	-0.6316	2.308	115.4

Table 4. Effect of modulation amplitude on signal phase

Larmor kHz	MF=3 phase effect Degrees / GHz	MF=4 phase effect Degrees / GHz	Combined phase effect Degrees / GHz	Required accuracy %	Required tempo PPM
69.97	0.1569	0.05895	0.1923	7.581	379
101.1	0.2256	0.0849	0.2766	5.271	263.5
132.2	0.2932	0.1106	0.3595	4.055	202.7
163.3	0.3592	0.136	0.4408	3.307	165.3
194.4	0.4235	0.1611	0.5201	2.803	140.1
225.6	0.4858	0.1856	0.5971	2.441	122
256.6	0.5458	0.2097	0.6715	2.171	108.5
287.7	0.6032	0.2331	0.7431	1.962	98.07
318.8	0.6581	0.256	0.8116	1.796	89.79
349.9	0.7101	0.2781	0.8769	1.662	83.1

Table 5. Effect of modulation positive peak value on signal phase

Preamplifier analysis

The preamplifier and subtraction circuit design will depend partly on the amount of modulation of the pump light that is seen at the photo detectors. The phase change here will depend on many factors. The absorption in the cell is at its maximum just after the light from the Laser is at its maximum. For this reason a phase near 180 degrees is to be expected at low frequencies.

The component of the effect from the pumping light that is in phase with or at inverse to the Larmor will only increase or decrease the amplitude. The component that is at right angles will pull the oscillation frequency. This latter is the more important effect as it will change the magnetometer reading or, in the extreme case, prevent oscillation at the Larmor frequency.

The component of the pump signal that is at right angles to the Larmor determines the amount of gain mismatch the system can withstand. The component of the Pump signal that is in phase with the Larmor determines the phase matching needed.

Larmor kHz	Amplitude uA	Phase Degrees	Preamp gain match percent	Preamp gain Tempco PPM / °C	Preamp phase match degrees	Preamp phase Tempco degrees / °C
69.97	0.972	121.2	0.5054	25.26	0.4787	0.002393
101.1	1.006	99.24	0.4232	21.16	1.49	0.007449
132.2	1.051	80.55	0.4054	20.27	1.396	0.006976
163.3	1.105	64.89	0.42	21	0.5135	0.002567
194.4	1.167	51.86	0.4578	22.88	0.3341	0.00167
225.6	1.236	41.04	0.5178	25.88	0.2583	0.001291
256.6	1.311	32.04	0.6043	30.21	0.2167	0.001083
287.7	1.391	24.52	0.7283	36.41	0.1903	0.000951
318.8	1.474	18.22	0.912	45.59	0.172	0.000859
349.9	1.561	12.91	1.205	60.23	0.1582	0.000791

Table 6. Effect of pump signal on probe signal phase

The above requirements for the precision of the component values are many orders of magnitude better than can be achieved. This will cause poor performance of the magnetometer at low frequencies.

Based on the requirements for the phase performance and the practical component values, we can compute the limits on the frequencies of the poles in the photo-preamplifier that are imposed by these requirements.

Larmor kHz	High Pass kHz	Low Pass kHz
69.97	5.85	837.5
101.1	26.28	388.6
132.2	32.2	542.5
163.3	14.6	1821.9
194.4	11.3	333.5
225.6	10.1	5001
256.6	9.7	6784
287.7	9.55	8662
318.8	9.57	10620
349.9	9.6611	12672

Table 7. Required band pass characteristics

The feedback resistance of the transimpedance amplifier and the capacitance of the photocell and associated cable form a low pass filter. This filter is part of the closed loop of the transimpedance amplifier and impacts the stability of the system and the bandwidth of the photo-preamplifier.

The amplifier section used in the transimpedance must provide enough gain and a small enough phase shift to ensure that the bandwidth and phase requirements of the complete system are met. The two transimpedance amplifiers must also match each other. For this reason a compound transimpedance amplifier design is used.

During the time that the pump Laser is on the sloping part of the absorption line, noise on the current can modulate the wavelength and hence the absorption. When the Laser is far from the line or tuned to the peak, this effect does not occur. This effect interacts with the brightness of the Laser at each instant in time. For this reason, the conversion factor from noise on the pump current to noise in the magnetometer depends on the Larmor frequency. This noise gets to the photodetector in three ways.

The first and most obvious is that when the wavelength is on the slope of the absorption, the amount of light reaching the photodetector varies. This will interact with any imperfection in the subtraction to appear as noise in the Larmor path.

The second and third ways are by variation of the amount of pumping of the MF=3 and MF=4 states. When the laser is on the MF=3 edge of the line, the variations in the wavelength will mostly cause variations in the phase of the MF=3 Larmor.

As the wavelength nears the center of the line, a partial cancellation of the noise will happen because any motion towards the MF=4 side of the line will simultaneously increase the pumping of the MF=4 state and decrease the pumping of the MF=3 state. We can handle this by computing the magnitude and phase of the sensitivity to noise for both the MF=3 and the MF=4 states and then adding as vectors.

Because there are nonlinearities, noise near the harmonics of the Larmor will be hetrodyned down to near the Larmor and thus become noise within the measurement bandwidth of the magnetometer. The thermal time constant of the pump Laser attenuates this effect at high Larmor frequencies.

Conclusion

In this section, we summarized the performance considerations of the electronics design as a whole, and analyze the performance of the present design. We conclude that a single beam interrogation method will not allow for high performance and practical electronics limitations limit the performance greatly from the shot-noise-limited performance that is theoretically achievable. Sources of practical error are primarily component tolerance and drift specifications that limit the rejection of unwanted signals and the stability of the low frequency performance of the magnetometer. In other words, while simultaneous performance at low frequency and high frequency is theoretically obtainable, practical limits in the electronics limit that achievable performance.

This works shows that the simplest sensor mechanical designs impose impossibly stringent requirements for the electronics. More complex physics package designs, reduce the complexity of the electronics, and could yield reasonable systems. We have learned a great deal in this project as to the achievable performance levels of many possible designs, and the tradeoffs that are possible.

Concluding Summary

We are very pleased with the results from this work, and excited about the potential for these devices. In this project we explored many methods of cell interrogation at high temperature regimes, where the bandwidth of the devices is greatly increased. We also considered the electronics implications for the various methods of interrogating the cell. All of this work was done with an eye towards commercially-viable methods of implementation and production.

Measurements of the linewidth of the Larmor resonance have confirmed that in Cs, a magnetometer bandwidth of 10 kHz can be achieved at a cell temperature of 135 °C. This was achieved in a cell containing Cs and ~350 Torr N₂. Measurements as a function of cell temperature confirm that at a cell temperature of 135 °C, the linewidth is dominated by spin-exchange collisions. This implies that the magnetometer is indeed operating in the appropriate high-density regime. We have also measured the magnetometer signal size as a function of the cell temperature. We find that at temperatures above ~ 100 °C, the signal does not continue to increase proportionally with the alkali density, but begins to saturate. This saturation is consistent with the effects of optical thickness in the cell. This result shows that improvements may be made upon absorption monitoring of the atomic polarization at high alkali densities.

In order to circumvent the difficulty due to the optical thickness, we have used a dual-laser configuration, in which one laser is used to pump the atoms, while a second probe laser, linearly polarized and tuned off resonance, measures the atomic polarization via magneto-optic (optical) polarization rotation. Since the polarization rotation can be generated by pure phase shifts of the optical field, the probe can be strongly detuned from resonance, leading to reduced absorption and a corresponding reduction of the loss of sensitivity due to the cell optical thickness. This technique has proven successful, as we have measured 10 pT / $\sqrt{\text{Hz}}$ at a bandwidth of 15 kHz.

In addition to the progress in evaluating the fundamental limits to the performance of the devices at high cell temperatures, we have completed a design for a device. Without requiring the more complicated structure of perpendicular pump and probe beams, we designed a complete physics package. While failure of key circuit elements prevented final testing of this prototype, we feel we still gained a good understanding of the design issues in our bench-top tests, and further gained excellent understanding of several methods to build the small components required for such devices.

In addition, we have demonstrated magnetometry in the spin-exchange relaxation free (SERF) regime in a millimeter-scale alkali vapor cell. This measurement resulted in a sensitivity of 70 fT/ $\sqrt{\text{Hz}}$ with a bandwidth of 290 Hz using a very simple excitation/detection scheme based on the optical absorption of a single laser beam. In this experiment the cell temperature was 152 °C, with further increase in the cell temperature limited by the absorption due to the increase in optical thickness. If the polarization-rotation solution can be applied in this situation, the bandwidth of the sensor could be increased significantly by operating at even higher cell temperatures with little loss in sensitivity.

Finally, we developed a set of electronics boards capable of implementing the techniques discussed above. All the functions of locking the pump and probe lasers to the required wavelengths, controlling the cell and VCSEL temperatures, and performing the signal extraction by locking to the RF resonance have been completed. Detailed design requirements and analysis were completed for both single and dual-beam interrogation methods, and we gained a good understanding of the requirements.

This work has laid a solid foundation for future designs of both narrow and wide-band sensors. We began in the laboratory, exploring several methods of cell interrogation and achieved simultaneous high sensitivity and wide-band operation. The simple optical designs that were prototyped in this project place overly stringent requirements on the electronics design, we learned. This has further pointed us towards new possibilities of interrogation structures that reduce the complexities of the electronics design. We are highly confident that this work will lead to many new generations of sensors.

Appendices

Appendix A: List of Technical Publications

P. D. D. Schwindt, B. Lindseth, J. Kitching, and L.-A. Liew, "A chip-scale atomic magnetometer with improved sensitivity using the Mx technique," *Applied Physics Letters*, **90**, 081102 (2007).

P. D. D. Schwindt, L. Hollberg, and J. Kitching, "Self-oscillating Rb magnetometer using non-linear magneto-optic rotation," *Review of Scientific Instruments*, vol. **76**, pp. 126103, 2005.

V. Shah, S. Knappe, P. Schwindt, J. Kitching, "Subpicotesla atomic magnetometry with a microfabricated vapour cell", *Nature Photonics*, Nov 1, 2007, Vol **1**, p. 649.

Prouty, Mark, "A Miniature Total field Magnetometer," SERDP-ESTCP Partners Symposium, Washington, DC, 2007.

M. A. Perez, et al., "Rubidium Vapor Cell with Integrated Nonmetallic Multilayer Reflectors," Submitted to 2008 IEEE International Conference on Microelectromechanical systems, 2008.

Brad Lindseth, Peter Schwindt, John Kitching, D. Fischer, V. Shusterman, Non-contact measurement of cardiac electromagnetic field in mice by use of a microfabricated atomic magnetometer, *Computers in Cardiology*, 2007

Elizabeth Hodby, Elizabeth Donley, John Kitching, Differential Atomic Magnetometry Based on a Diverging Laser Beam, *Applied Physics Letters*, vol **91**, pp011109, 2007

L.-A. Liew, J. Moreland, and V. Gerginov, Wafer-level fabrication and filling of cesium-vapor cells for chip-scale atomic devices, *Eurosensors*, Sweden, 2007

References

¹ D. Budker, et al., "Sensitive magnetometry based on nonlinear magneto-optical rotation," *Phys. Rev. A* **6204**, 043403, (2000)

² I. K. Kominis, et al., "A subfemtotesla multichannel atomic magnetometer," *Nature* **422**, 596, (2003)

³ J. C. Allred, et al., "High-sensitivity atomic magnetometer unaffected by spin-exchange relaxation," *Phys. Rev. Lett.* **89**, (2002)

⁴ P. D. D. Schwindt, et al., "Chip-scale atomic magnetometer," *Appl. Phys. Lett.* **85**, 6409, (2004).

⁵ W. Happer and H. Tang, "Spin-exchange shift and narrowing of magnetic resonance lines in optically pumped alkali vapors," *Phys. Rev. Lett.* **31**, 273, (1973)

⁶ P. D. D. Schwindt, et al., "Chip-scale atomic magnetometer," *Appl. Phys. Lett.* **85**, 6409 (2004).

⁷ S. J. Smullin, I. M. Savukov, G. Vasilakis, R. K. Ghosh, and M. V. Romalis, "Low-noise high-density alkali-metal scalar magnetometer," *Phys. Rev. A* **80**, 033420, (2009)

⁸ R. Jiménez-Martínez et al., "Conversion of laser frequency noise to optical rotation noise in a Cs vapor cell," *Optics Letters*, **34**, 2519-2521, (2009)

⁹ M. A. Perez, et al., "Rubidium Vapor Cell with Integrated Nonmetallic Multilayer Reflectors," Submitted to 2008 IEEE International Conference on Microelectromechanical systems, (2008)

¹⁰ G. Kovacs, N. Maluf, and K. Petersen, "Bulk micromachining of silicon," Proc. IEEE, vol. **86**, no. 8, pp. 1536, (1998)

¹¹ L. Martinu and D. Poitras, "Plasma deposition of optical films and coatings: A review," Journal of Vacuum Science & Technology A: Vacuum, Surfaces, and Films, vol. **18**, no. 6, pp. 2619, (2000)

¹² M. Schmidt, "Wafer-to-wafer bonding for microstructure formation," Proc. IEEE, vol. **86**, no. 8, pp. 1575, (1998)

¹³ V. Shah, and M. Romalis, "Spin-Exchange-Relaxation-Free Magnetometry Using Elliptically-Polarized Light," Phys. Rev. A **80**, 013416 (2009)

¹⁴ W. Happer and A. Tam, "Effect of rapid spin exchange on the magnetic-resonance spectrum of alkali vapors," Phys. Rev. A **16**, 1877 - 1891 (1977)